LBNL-41069

# ERNEST ORLANDO LAWRENCE BERKELEY NATIONAL LABORATORY

**BERKELEY LAB**

## Theoretical and Experimental Investigations of Ferrofluids for Guiding and Detecting Liquids in the Subsurface

### FY 1997 Annual Report

G.J. Moridis, S.E. Borglin,
C.M. Oldenburg, and A. Becker

**Earth Sciences Division**

March 1998

# DISCLAIMER

**Portions of this document may be illegible in electronic image products. Images are produced from the best available original document.**

LBNL-41069

FY 1997 ANNUAL REPORT

# THEORETICAL AND EXPERIMENTAL INVESTIGATIONS OF FERROFLUIDS FOR GUIDING AND DETECTING LIQUIDS IN THE SUBSURFACE

**G.J. Moridis, S.E. Borglin,
C.M. Oldenburg and A. Becker**

*Earth Sciences Division
Lawrence Berkeley National Laboratory
Berkeley, CA 94720*

**March 1998**

# Abstract

Ferrofluids are stable colloidal suspensions of magnetic particles in various carrier liquids with high saturation magnetizations, which can be manipulated in virtually any fashion, defying gravitational or viscous forces in response to external magnetic fields.

In this report we review the results of our investigation of the potential of ferrofluids (1) to accurately and effectively guide (i) reactants (for *in-situ* treatment) or (ii) barrier liquids (low-viscosity permeation grouts) to contaminated target zones in the subsurface using electromagnetic forces, and (2) to trace the movement and position of liquids injected in the subsurface using geophysical methods.

We investigate the use of ferrofluids to enhance the efficiency of *in-situ* treatment and waste containment through (a) accurate guidance and delivery of reagent liquids to the desired subsurface contamination targets and/or (b) effective sweeping of the contaminated zone as ferrofluids move from the application point to an attracting magnet/collection point. We also investigate exploiting the strong magnetic signature of ferrofluids to develop a method for monitoring of liquid movement and position during injection using electromagnetic methods.

Starting from first principles, the partial differential equation of ferrofluid flow in porous media was derived. This equation is analogous to the conventional Darcy equation, from which it differs by the inclusion of magnetic and magnetostrictive forces. Analytical 1-D solutions were developed for a the 1-D saturated flow of ferrofluids through porous media in response to a magnetic field. Using the TOUGH2 general simulator of flow and transport through porous media, the new module EOS7M describing the behavior and flow of ferrofluids in the presence of a magnetic field, was developed and verified. The EOS7M module accounts for the effects of the magnetic field on the ferrofluid, as well as the coupled effects of water-miscibility on the ferrofluid properties and its flow and transport characteristics.

We studied the movement of an aqueous ferrofluids in response to magnetic fields from permanent magnets and electromagnets. We demonstrated the ability to induce ferrofluid movement in response to a magnetic field, and measured the corresponding magnetopressure. 2-D Hele-Shaw and sand tray experiments demonstrated the ability to guide ferrofluids in response to external magnetic fields, and showed that despite differently-shaped

initial ferrofluid distributions, varying initial distance from the magnets, heterogeneous permeability fields and ferrofluid flow along preferential pathways, the final ferrofluid distribution is invariably predictable, symmetric and is controlled by the magnetic field. In other words, the final ferrofluid distribution is unaffected by heterogeneities in the properties of the porous media and flow patterns. The implication of this realization is that ferrofluids with appropriate reagent-laden carrier liquids can be accurately guided to and positioned in contaminated target zones in the subsurface.

We demonstrated the feasibility of using conventional magnetometry for detecting subsurface zones of various shapes containing ferrofluids for tracing liquids injected for remediation or barrier formation. Experiments involving spherical, cylindrical and horizontal slabs showed a very good agreement between predictions and measurements.

# TABLE OF CONTENTS

# LIST OF FIGURES

# LIST OF TABLES

# 1. INTRODUCTION

This reports summarizes work on the use of ferrofluids in subsurface environmental applications conducted in Fiscal Year 1997 at the Lawrence Berkeley National Laboratory (LBNL). We investigate the potential of ferrofluids to (a) accurately and effectively guide liquids (reactants, for *in-situ* treatment, or barrier liquids, i.e. low-viscosity permeation grouts) to contaminated target zones in the subsurface using electromagnetic forces, and, (b) to trace the movement and position of liquids injected in the subsurface using geophysical methods.

Ferrofluids represent a new development, and thus the existing body of information on their use in environmental and geophysical applications involving problems of flow and transport through porous media is very limited. To our knowledge, the only known study of the subject is currently in progress by this LBNL team. The present report draws heavily from information developed in the course of this study [*Moridis and Oldenburg, 1998;Oldenburg et al., 1998; Borglin and Moridis, 1998; Borglin et al., 1998*].

## 1.1. Background

Ferrofluids are stable colloidal suspensions of magnetic particles in various carrier liquids [*Raj and Moskowitz*, 1990; *Ferrofluidics*, 1992]. The solid, magnetic, single-domain particles are small (with an average diameter of 3-15 nm) and are covered with a molecular layer of a dispersant. Thermal agitation due to Brownian motion keeps the particles

suspended, while the dispersant coating prevents the particles from agglomeration. The stability of ferrofluids means that an external magnetic field does not lead to local changes in the concentration of the magnetic particles in the carrier liquid, i.e. the concentration of the particles in the ferrofluid remains spatially and temporally constant regardless of the presence or strength of the external field. Consequently, ferrofluids behave like a homogeneous single-phase fluid when flowing under the influence of a magnetic field. Therefore, ferrofluids can be made to flow in a desired direction and move precisely without any physical contact [*Chorney and Mraz*, 1992]. This attribute is responsible for the unique property of ferrofluids that they can be manipulated in virtually any fashion, defying gravitational or viscous forces in response to external magnetic fields.

Ferrofluids were first developed by NASA to handle liquid propellants in the absence of gravity in outer space. Due to their ability to be held in place by magnetic fields, they are currently used (a) in hermetic seal pumps, which eliminate leakage along rotating shafts and joints [*Bailey*, 1983], (b) as barriers against volatile organic compounds in chemical processing, (c) in rotating vacuum seals used in semiconductor processing and environmentally controlled chambers [*Moskowitz*, 1975], (d) in sealed microwave, laser, and nuclear applications [*Rosensweig*, 1979], as well as in computer disk drives. They are also used in niche areas such as high-fidelity audio speakers and precision bearings [*Chorney and Mraz*, 1992], and have a number of biomedical applications. Therapeutic agents have been incorporated into or onto the magnetic particles, which are then guided and concentrated by magnetic fields at specific body sites [*Senyei and Widder*, 1981; *Morimoto*, 1983). Ferrofluids have also been used as tracers of blood flow in non-invasive circulatory measurements [*Newbower*, 1972].

# 1.2. Objectives

The objectives of this project are to investigate the potential of ferrofluids
(1) to accurately and effectively guide (i) reactants (for *in-situ* treatment) or (ii) barrier liquids (low-viscosity permeation grouts) to contaminated target zones in the subsurface using electromagnetic forces, and,
(2) to trace the movement and position of liquids injected in the subsurface using geophysical methods.

# 1.3. Significance and Applications

The ferrofluid-based environmental engineering approaches and applications investigated in this project are applicable to all sites in the DOE complex that involve the injection and monitoring of environmental liquids into the subsurface as a part of a remediation effort, and cover all the problem areas covered by the Focus Groups, i.e. High Level Waste Tanks, Mixed Waste, Subsurface Contamination, and Cross-Cutting Technologies. In particular, sites with pressing remediation needs and challenging conditions, such as Hanford, Savannah River, Oakridge, INEL and Fernald, could potentially benefit from the application of ferrofluids-based technologies.

Ferrofluids have several unique properties. They move as a homogeneous single-phase fluid under the influence of a magnetic field, with no separate consideration for the magnetic particles and the carrier liquid. They can be manipulated in virtually any fashion, defying gravitational or viscous forces in response to external magnetic fields [*Chorney and Mraz*, 1992]. Additionally, the magnetic particles cast a strong magnetic signature, which can be exploited for imaging and tracking injected liquids using geophysical methods.

The controlled emplacement of liquid reactants in order to treat or contain contaminants in the subsurface is a critical problem in all aspects of *in-situ* remediation or containment, and its failure invariably leads to failure of the remediation method, regardless of its other merits or elegance. Current emplacement practices for subsurface treatment consist entirely of injection, and the mechanism for fluid guidance is pressure (potential) differentials. This is a 'brute-force' approach, often inefficient and unpredictable, because it-is diffusive and subject to short-circuiting by highly-permeable zones. The ferrofluid-based approach proposed here can alleviate the adverse effects of heterogeneity and can lead to more accurate and effective technologies for targeting and delivery of reactants or other liquids to contaminated zones in the subsurface.

An ability to track and monitor the movement and position of injected liquids is essential in assessing the effectiveness of the delivery system and the success of the process. A number of geophysical methods (such as ground-penetrating radar, electrical resistance tomography, tiltmeters, etc.) can be used to accomplish this task. Ferrofluid tracers can also provide a powerful means for tracking the movement and location of liquids in the subsurface, as well as providing a means for testing the integrity of subsurface barriers (i.e. detection of holes). Ferrofluids used in conjunction with gelling barrier liquids may be useful as tracers to identify preferential and/or high-permeability pathways (along which the likelihood of contaminant migration is maximum) in the fractured rocks of the Yucca Mountain site.

# 1. Introduction

# 2. TECHNOLOGY DESCRIPTION

## 2.1. Ferrofluids for Guiding Liquids in the Subsurface

A Ferrofluid for Guiding liquids will be hereafter referred to as a FG. The ability of ferrofluids to be guided precisely to specific areas in response to an external field could be significant for subsurface environmental restoration. We propose to use FGs to enhance the efficiency of *in situ* treatment and waste containment through (a) accurate guidance and delivery of reagent liquids to the desired subsurface contamination targets and/or (b) effective sweeping of the contaminated zone as FGs move from the application point to an attracting magnet/collection point. The ferrofluids to be used in such applications will have the appropriate carrier liquids, containing reactants (e.g. oxidants) for *in-situ* treatment and barrier liquids (such as colloidal silica) for containment [*Moridis et al.*, 1995].

Current emplacement practices consist entirely of injection, and suffer from the adverse effects of heterogeneity which may cause the subsurface treatment to be short-circuited by preferential flow through the highly-permeable zones. Magnetic fields are easier to manipulate than pressure fields and are unaffected by the significant heterogeneity of the soil hydraulic properties. Magnetic fields may be affected by heterogeneities in the soil magnetic properties, but these are far less pronounced in magnitude and are far less important to FG flow than the subsurface hydraulic conductivity. Emplacement of liquids (for *in-situ* treatment or containment) in response to a magnetic field is expected to be more accurate and effective than emplacement in response to a pressure differential. This approach will allow fluids to be focused and guided to the desired locations in the subsurface, and more

effectively sweep the targeted treatment zone. Of particular interest is the application of FG technologies to the treatment or containment of leaking underground tanks. If the tanks can be induced to behave magnetically, a very effective treatment is possible as the injected FGs would accumulate against them in response to the tank magnetic field.

## 2.2. Ferrofluids for Monitoring, Verification and Tracing

A Ferrofluid for Tracing and detecting liquids in the subsurface will be hereafter referred to as a FT. The magnetic particles cast a strong electromagnetic signature. Because of this property, ferrofluids are used commercially for magnetic pattern recognition in magnetic tapes, hard and floppy disks, crystalline and amorphous alloys, steels, and rocks [*Ferrofluidics*, 1992]. Due to the high saturation magnetization $M_{sat}$ of the ferrofluids, this signature is sufficiently strong for magnetic detection methods at low loading volumes, i.e. 1-5% by volume, which may be insufficient to allow liquid movement in response to external fields. We propose to exploit this fact to develop a real-time monitoring of fluid movement and position during injection using ElectroMagnetic (EM) methods. Ferrofluids can also provide a significant detection and verification tool in containment technologies, where they can be injected with the barrier liquids to provide a strong signature allowing determination of the barrier geometry, extent, continuity and integrity. Finally, ferrofluids may have unique properties as tracers for detecting preferential flow features (such as fractures) in the subsurface, and thus allow the design of more effective remediation systems.

## 2.3. Ferrofluid Properties

Ferrofluids have low viscosities (as low as 2 cp), thus allowing easy injection into the subsurface. Their small particle size (3-15 nm) minimizes potential filtration problems. Typical ferrofluids contain $10^{23}$ particles/m$^3$ and are opaque to visible light. They also possess a very high saturation magnetization. In magnetite-based ferrofluids, the saturation magnetization $M_{sat}$ varies between 80-80, 000 A/m (corresponding to flux densities of 1-1000 Gauss). Neodymium-Iron-Boron and Samarium-Cobalt ferrofluids exhibit saturation magnetization about four times larger than similar magnetite systems. The size of the magnetic particles is limited by the stability requirements necessary to counter the magnetic field gradient, the gravitational field, and magnetic agglomeration. At a temperature of 25 $^{o}C$ it can be shown that the maximum size for stability is about 10 nm [*Rosensweig*, 1985]. Use of appropriate surfactants makes possible the stability of ferrofluids with larger particle sizes.

The algebraic sum of the van der Waals attractive energy, magnetic attractive energy, and steric repulsion energy (due to the presence of polar molecules adsorbed on the particle surface) determines the stable monodispersity of the particle suspensions in ferrofluids. The dispersant molecules can be polar surfactants with a polar head group attached to a long chain or long polymer molecules containing polar groups along the length of the chain and exhibiting multisite adsorption on the magnetic particle. Ferrofluids with several polar adsorbing groups (e.g. carboxyl, phosphate, sulfosuccinate, etc.) are available.

There is no long-range order between the particles of a colloidal ferrofluid. In the absence of a magnetic field, the particles are randomly oriented, and the fluid has no net magnetization. Ferrofluids are extremely *soft* magnetic materials, and as such do not exhibit hysteresis. The study of ferrofluids involves traditional ferromagnetic concepts. The relationship between the induction field $\vec{B}$, the external magnetic field $\vec{H}$ and the intensity of magnetization $\vec{M}$ of a ferrofluid is given by

$$\vec{B} = \mu_m(\vec{H} + \vec{M}), \qquad (2.1)$$

where $\mu_m$ is the magnetic permeability of the medium. The effect of the ferrofluid presence is included in the magnetization $\vec{M}$. In *soft* magnets such as ferrofluids $\vec{M}$ and $\vec{H}$ are aligned. The magnetization curve (i.e. the $M$ *vs.* $H$ curve) for a typical ferrofluid used in the experiments discussed in Section 4 (EMG 805$^{TM}$, Ferrofluidics Corporation) is shown in **Figure 2.1**. A more detailed analysis of the $M$-$H$ relationship in ferrofluid systems is discussed in Section 5.

Ferrofluids are superparamagnetic materials. Under sinusoidal excitation (AC magnetization) the imaginary component of the susceptibility determines the phase shift between the field $H$ and the magnetic induction $B$. For superparamegnetic materials, under step excitation the magnetization does not fall to zero instantaneously with the removal of the magnetizing field but decays logarithmically with time.

The quantitative aspects of complex susceptibility are discussed fully by *Becker and Collett* [1978]. In summary, for sinusoidal excitation, the magnetizing field may be defined by

$$h = H \, exp(j\omega t), \qquad (2.2)$$

where $\omega$ is the frequency and $j = \sqrt{-1}$. A complex magnetic susceptibility is defined as

$$\mu_m^* = \mu_R - j\mu_I, \qquad (2.3)$$
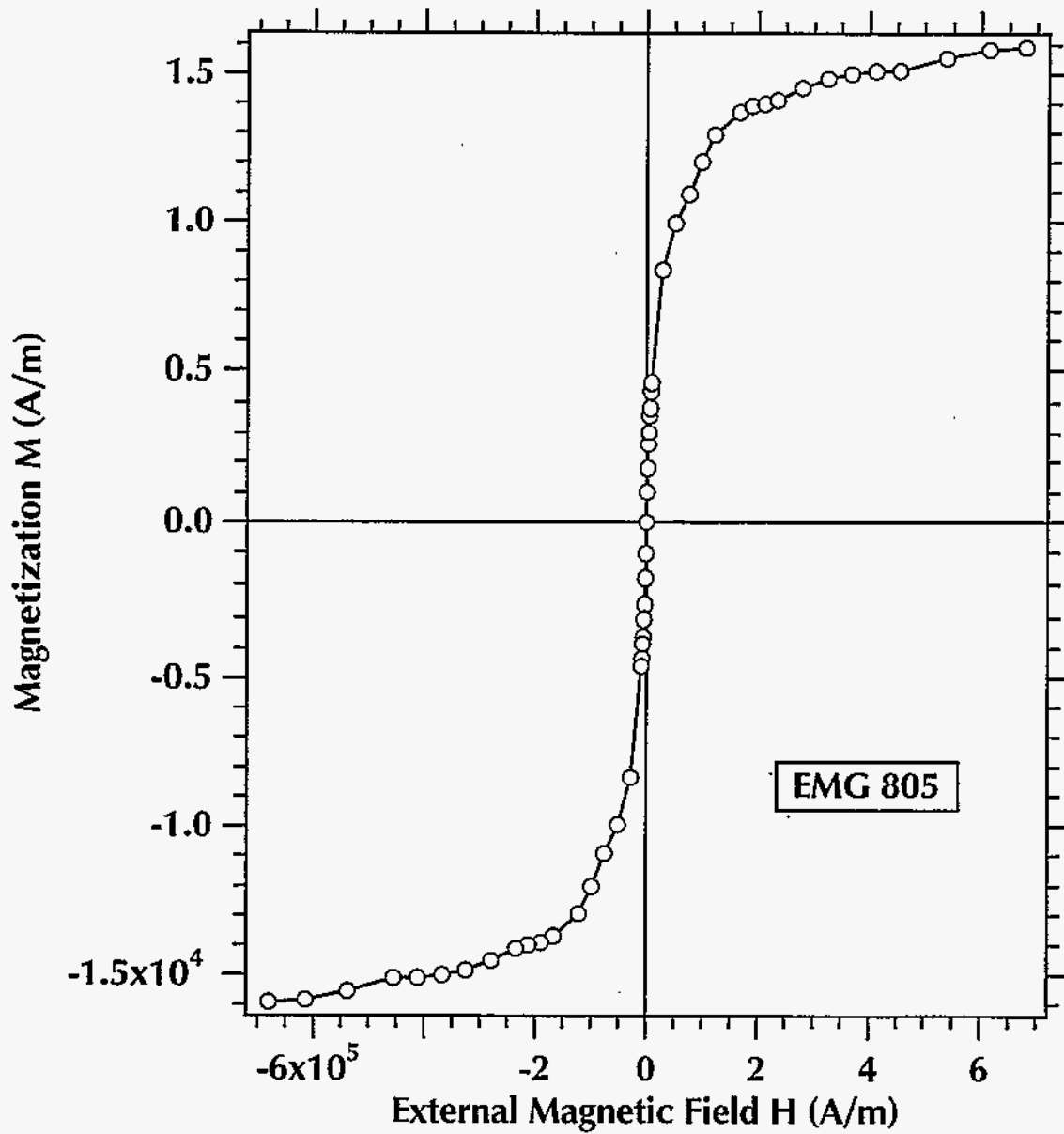
**Figure 2.1.** Typical magnetization (*M-H*) curve [*Nunes and Yu*, 1989] for an aqueous ferrofluid (EMG 805™, Ferrofluidics Corporation, Nashua, NH).

where the subscripts $R$ and $I$ denote the real and imaginary components. The power absorbed per unit volume of material is then given by

$$P = \frac{1}{2}\omega\mu_I H^2. \tag{2.4}$$

These relationships constitute the basis of a potentially powerful detection method for ferrofluid tracking of liquids in the subsurface. This issue is currently being investigated.

## 2. Technology Description

# 3. THEORETICAL STUDIES OF FG FLOW

## 3.1. Ferrohydrodynamics in Subsurface Flow

FerroHydroDynamics (FHD) is the discipline dealing with the study of the dynamics of ferrofluid motion under the influence of a strong magnetic field. There are significant differences between FHD and the better-known discipline of Magnetohydrodynamics (MHD). FHD does not necessarily require an electric current flowing through the ferrofluid, and usually there is none. The body force in FHD is due to a polarization force, which in turn requires material magnetization in the presence of magnetic field gradients [*Rosensweig*, 1985]. On the other hand, the body force acting on fluids in MHD is the Lorentz force which develops when an electric current flows at an angle to the direction of the impressed magnetic field. The force interaction in MHD is often due to free electric charge acted upon by an electric force field. Free electric charge is normally absent in FHD, as the magnetic analog of the electric charge (i.e. the monopole) has not been found in nature. An in-depth study of FHD can be found in *Rosensweig* [1985].

## 3.2. Equation of FG Flow

This section closely follows the development of the general equation of FG flow through porous rocks found in *Oldenburg et al.* [1998] and *Moridis and Oldenburg* [1998].

### 3.2.1. Force Balance

Balancing forces on the fluid in an elementary volume $dV = dA\,ds$ in **Figure 3.1** yields:

$$p\phi dA - \left(p + \frac{\partial p}{\partial s}ds\right)\phi dA - (\rho g\phi dV)\cos\theta - F_R + F_M = 0, \qquad (3.1)$$

where $\cos\theta = \partial z/\partial s$, $p$ is the fluid pressure, $\phi$ is the porosity, $dA$ is the elementary area, $ds$ is the elementary length along a streamline $s$, $F_R$ is the resistive force and $F_M$ is the magnetic force acting on $dV$. Expanding, substituting and simplifying (3.1) yields

$$-\frac{\partial p}{\partial s} - \rho g\frac{\partial z}{\partial s} - \frac{F_R}{\phi dV} + \frac{F_M}{\phi dV} = 0. \qquad (3.2)$$

### 3.2.2. Resistance to Flow

Using *DeWiest*'s [1969] approach for the development of the general Darcy equation of flow, the resistance to flow $f_p$ in an idealized porous medium composed of spheres is given by Stokes's Law:

$$f_p = \lambda\mu du_s, \qquad (3.3)$$

where $u_s$ is the fluid velocity, $\lambda = 3\pi$ for a single sphere, $\mu$ is the liquid viscosity, and $d$ is the particle diameter. The total resistance force for $N$ spheres is

$$F_R = Nf_p, \qquad (3.4)$$

where

$$N = \frac{(1-\phi)dV}{V_p}, \qquad (3.5)$$

and $V_p = \beta\,d^3$ is the volume of a single particle, $d$ is the particle diameter, and $\beta$ is a shape factor). Combining and rearranging equations, we have

$$\frac{F_R}{\phi dV} = \frac{Nf_p}{\phi dV} = \frac{(1-\phi)\lambda}{\phi^2\beta}\frac{\mu}{d^2}\phi u_s. \qquad (3.6)$$
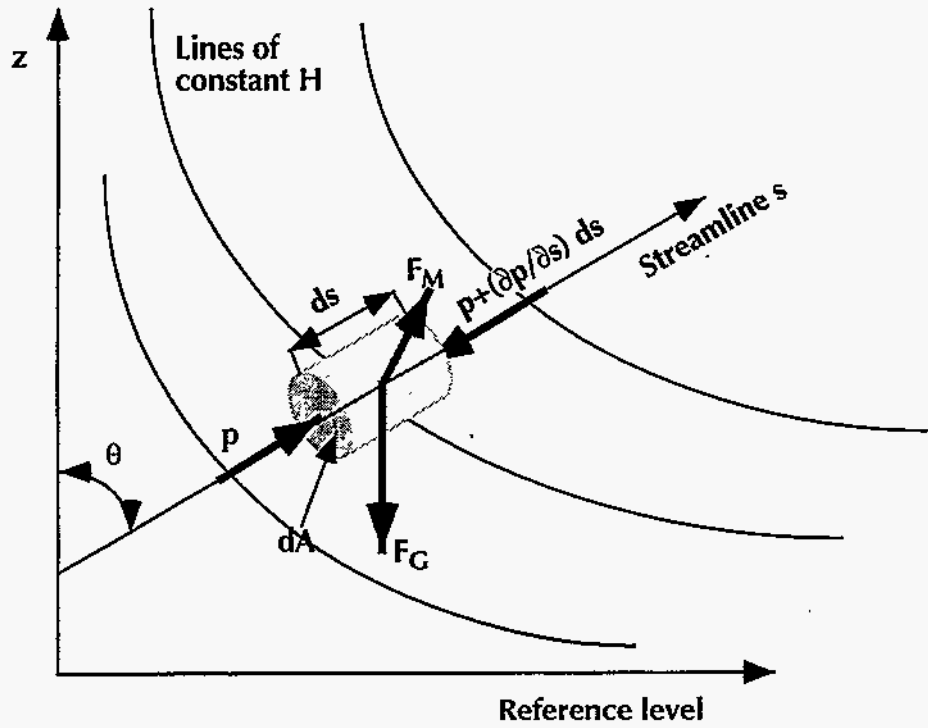
**Figure 3.1.** Force balance on the elementary volume $dV = dA\ ds$.

Defining

$$E_m = \frac{(1-\phi)\lambda}{\phi^2 \beta}, \quad k = \frac{d^2}{E_m}, \quad \text{and} \quad q_s = \phi u_s, \tag{3.7}$$

we obtain

$$\frac{\dot{F}_R}{\phi dV} = \frac{\mu}{k} q_s. \tag{3.8}$$

### 3.2.3. Magnetic Force

Based on the analysis of *Rosensweig* [1985], the magnetic force acting on the ferrofluid in the elementary volume $dV$ along the streamline $s$ is given by

$$F_M = \left( \mu_{m0} M \frac{\partial H}{\partial s} - \frac{\partial p_s}{\partial s} \right) \phi\, dV, \tag{3.9}$$

where $p_s$ is the magnetostrictive pressure defined by

$$p_s = \mu_{m0} \int_0^H \left[ \frac{\partial(MV)}{\partial V} \right]_{H,T} dH, \tag{3.10}$$

$\partial H / \partial s$ is the gradient of the total magnetic field $H$ in the $s$-direction, $M$ is the magnetization and $T$ is the temperature. $M$ is a non-linear function of $H$ that reflects the increasing magnetization of the ferrofluid. $M$ increases with $H$ up to the point of *saturation*, beyond which $M$ remains constant even as $H$ increases (**Figure 2.1**)

### *3.2.4. Final Form*

Combining equations (3.2), (3.8), and (3.9) we obtain

$$q = -\frac{k}{\mu} \left[ \frac{\partial p}{\partial s} + \frac{\partial p_s}{\partial s} - \mu_{m0} M \frac{\partial H}{\partial s} + \rho g \frac{\partial z}{\partial s} \right]. \tag{3.11}$$

The general form of the equation then becomes

$$\vec{q} = -\frac{k}{\mu} \left[ \nabla p + \nabla p_s - \rho g_m \nabla H + \rho g \nabla z \right], \tag{3.12}$$

where

$$\vec{g_m} = \frac{\mu_{m0}}{\rho} \vec{M}. \tag{3.13}$$

This formulation emphasizes that the magnetic effects of an external field on the ferrofluid are analogous to gravitational effects. In contrast, however, to $\vec{g}$ which is invariant (at least locally) in terms of magnitude and direction, the magnitude and direction of $\vec{g_m}$ varies significantly. The general equation (3.12) was developed from first principles [*Moridis and Oldenburg*, 1998], and is very similar in form and content to the well-known Darcy flow equation

$$\vec{q} = -\frac{k}{\mu} \left[ \nabla p + \rho \vec{g} \right]. \tag{3.14}$$

describing the flow of fluids in the subsurface in response to a hydraulic gradient, from which it differs in the incorporation of the second and third terms in (3.12). These terms describe the relationship between the magnetic field $H$ and the fluid, and are significant only

in the presence of both. In the absence of ferrofluids and/or magnetic fields $H$, equation (3.12) reverts to (3.14).

Even in the absence of a magnetic field ($\vec{H} = \vec{0}$), the ferrofluid rheology has to be accounted for in (3.12). Due to energy dissipation caused by the movement of the suspended particles during viscous flow, the ferrofluid mixture viscosity $\mu$ is related to the carrier fluid viscosity $\mu_0$ through the relationship [*Rosensweig*, 1985]

$$\frac{\Delta\mu}{\Phi\mu} = 2.5\left(1+\frac{\delta}{r}\right)^3 - \left(\frac{2.5\Phi_c - 1}{\Phi_c^2}\right)\left(1+\frac{\delta}{r}\right)^6\Phi, \qquad (3.15)$$

where $\Delta\mu = \mu - \mu_0$, $\Phi$ is the solids fraction in the ferrofluid (disregarding the surfactant coatings), $\Phi_c$ is the solids fraction at which the suspension becomes effectively rigid (usually $\Phi_c = 0.72$), $r$ is the particle radius and $\delta$ is the length of the absorbed polar molecule (surfactant). The viscosity quantities $\mu_0$ and $\mu$ should not be confused with the magnetic permeability of the free space $\mu_{m0}$. Equation (3.15) defines a straight line when plotting $(\mu - \mu_0)/(\Phi\mu)$ *vs.* $\Phi$. An alternative method to account for viscosity changes of the ferrofluid system is discussed in Section 5.

In the presence of an external magnetic field, the magnetic particles in the fluid tend to remain rigidly aligned with the direction of the orienting field, resulting in an increased viscous dissipation. The effect on viscosity was quantified by *Shliomis* [1972] as

$$\xi^3 - 2\xi^2 + \xi\left[1 + \frac{(\Theta+1)}{(\Omega\tau)^2}\right] - \frac{\Theta}{(\Omega\tau)^2} = 0, \qquad (3.16)$$

where

$$\xi = \Delta\mu/\zeta, \quad \Theta = \frac{\mu_{m0}M_0 H\tau}{4\zeta}, \quad \zeta = 1.5\mu\Phi, \quad \tau = \frac{3V_p\mu}{k_B T}, \qquad (3.17)$$

$M_0$ is the unperturbed magnetization, $V_p$ is the volume of a single particle, $\Omega$ is the vorticity, and $k_B = 1.38 \times 10^{-23}$ J·K$^{-1}$ is the Boltzmann constant. The quantities $\tau$ and $\zeta$ in equation (3.17) represent the Brownian relaxation time and the vortex viscosity, respectively. Calculations for typical ferrofluids yield values of $\tau$ on the order of $10^{-6}$ s *Rosensweig* [1985], and laboratory experiments determined that $\Omega\tau < 10^{-3}$ [*Rosensweig*, 1979]. Under these conditions, equation (3.16) reduces to

$$\xi = \frac{\Theta}{1+\Theta}, \quad \text{i.e.} \quad \frac{\Delta\mu}{\zeta} = \frac{\mu_{m0}M_0 H\tau}{4\zeta + \mu_{m0}M_0 H\tau} \qquad (3.18)$$

The general equation of flow of fluid $\ell$ in the presence of hydraulic and magnetic gradients is obtained by combining (3.12) with the equation of conservation of mass, yielding

$$-\nabla \cdot (\rho k_r q) = \frac{\partial}{\partial t}(\rho \phi S) + W, \tag{3.19}$$

where $S$ is the fluid saturation, $k_r$ is the relative permeability and $W$ is a source or sink term of the fluid. If a ferrofluid is the only fluid in the pore space as a single phase $(S = 1)$, then equation (3.19) provides all the needed flow information when coupled with the solution of the Maxwell equations (Section 3.3).

In most potential applications, however, ferrofluids will be introduced into fully or partially saturated subsurface formations (porous and/or fractured). If a ferrofluid with an organic carrier liquid is used, equation (3.19) results in two (in fully saturated media) or three (in partially saturated media) equations corresponding to each of the components in the phases present (i.e. aqueous, gaseous, and organic). If, however, an aqueous carrier liquid is used, equation (3.19) is applicable to the aqueous (including the ferrofluid) and the gaseous (if present, i.e. in an unsaturated system) phases, and additional information must be provided to account for the ferrofluid dilution.

This is provided by the advection-diffusion equation, which is given by

$$\frac{\partial}{\partial x_i}\left(\mathbf{D}_{ij}\frac{\partial C}{\partial x_j}\right) - \frac{\partial}{\partial x_i}(v_i C) = \frac{\partial}{\partial t}(\phi C) + W C_q + m \tag{3.20}$$

where $\mathbf{D}_{ij}$ is the tensor of hydrodynamic dispersion, $C$ is the ferrofluid concentration, $v_i$ is the Darcy velocity of the aqueous phase, $C_q$ is the ferrofluid concentration in the source or sink of strength q, and $m$ is the rate of mass transfer of the species between the liquid (solute) and the soil matrix (adsorbate). $\mathbf{D}_{ij}$ includes both mechanical dispersion [*Scheidegger*, 1961] and colloidal diffusion (analogous to molecular diffusion [*Millington*, 1959]), and is given by *Dorgarten and Tsang* [1991] as

$$\mathbf{D}_{ij} = \delta_{ij}\alpha_t|v| + (\alpha_\ell - \alpha_t)\frac{v_i v_j}{|v|} + \delta_{ij}\phi^{4/3}D_c, \tag{3.21}$$

where $\delta_{ij}$ is the Kronecker delta, $\alpha_\ell$ and $\alpha_t$ are the longitudinal and transverse dispersivities respectively, and $D_c$ is a colloidal diffusivity. Assuming linear non-equilibrium sorption, a general expression for $m$ is [*Voss*, 1984]

$$m = (1 - \phi)(m_1 C + m_2 C_s), \tag{3.22}$$

where $m_1$ and $m_2$ are sorption parameters, and $C_s$ is the concentration of adsorbate on the grains of the porous medium. If a linear equilibrium sorption model is assumed, then

$$C_s = K_d C, \qquad \text{and} \qquad m = (1 - \phi) K_d \frac{\partial C}{\partial t}, \qquad (3.23)$$

where $K_d$ is a *distribution coefficient*. It must be noted that the high density of ferrofluids does not allow any simplifications in equations (3.12) and (3.20), which must be solved in their fully coupled form using an approach such as the one of *Oldenburg and Pruess* [1995].

# 3.3. Equations of the Magnetic Field

The coupled equations ((3.12) and (3.20) in aqueous, (3.12) and (3.19) in oil-based ferrofluids) are not sufficient to solve the problem of FG flow in response to hydraulic and magnetic gradients. The following Maxwell equations must also be solved:

$$\nabla \times \vec{H} = \vec{J}_f + \frac{\partial \vec{D}}{\partial t}, \qquad (3.24)$$

i.e. Ampere's law with the Maxwell correction, as well as Gauss's second law

$$\nabla \cdot \vec{B} = 0. \qquad (3.25)$$

In most FHD applications, including the proposed FG applications, the free current density and Maxwell's displacement current are negligible [*Rosensweig*, 1985; *Moridis and Oldenburg*, 1998]. Under these circumstances, the field equations of FHD are the magnetostatic limit of Maxwell's equation:

$$\nabla \times \vec{H} = \vec{0} \qquad \text{and} \qquad \nabla \cdot \vec{B} = 0. \qquad (3.26)$$

The component of $\vec{B}$ normal to the interface of a ferrofluid is continuous, and that tangential component of the magnetic field $\vec{H}$ is also continuous [*Rosensweig*, 1985]. This defines the boundary conditions as

$$\vec{n} \times (\vec{H}_2 - \vec{H}_1) = \vec{0} \qquad \text{and} \qquad \vec{n} \cdot (\vec{B}_1 - \vec{B}_2) = 0, \qquad (3.27)$$

where $\vec{n}$ is the vector normal to the interface, and the subscripts 1 and 2 denote the relevant parameters on either side of the interface.

The calculation of the external magnetic field is complicated for general systems where magnetic permeability varies in the domain. However, in situations where the medium is

of uniform magnetic permeability and permanent magnets or electromagnets are the source of the magnetic field, we can use some simple equations to calculate the components of $H$ directly. The equations of the magnetic field as functions of the geometry and properties of a permanent magnet are given by *McCaig and Clegg* [1987]. (The earlier version of the book [*McCaig*, 1977] presented the equations with a factor $1/2\pi$ missing). For the permanent magnet in **Figure 3.2**, with a magnetic polarization of $B_r$ and dimensions $L_m$, $2a$, and $2b$ in the $x$, $y$ and $z$ directions respectively, the components of the magnetic field $H_x$, $H_y$ and $H_z$ at any point in space are given by

$$H_d = G_d(x, y, z) - G_d(x + L_m, y, z), \qquad d \equiv x, y, z, \qquad (3.28)$$

where

$$
\begin{aligned}
G_x(x, y, z) = \frac{B_r}{4\pi\mu_0} \Bigg\{ & \tan^{-1}\left[\frac{(y+a)(z+b)}{x\left[(y+a)^2 + (z+b)^2 + x^2\right]^{1/2}}\right] \\
& + \tan^{-1}\left[\frac{(y-a)(z-b)}{x\left[(y-a)^2 + (z-b)^2 + x^2\right]^{1/2}}\right] \\
& - \tan^{-1}\left[\frac{(y+a)(z-b)}{x\left[(y+a)^2 + (z-b)^2 + x^2\right]^{1/2}}\right] \\
& - \tan^{-1}\left[\frac{(y-a)(z+b)}{x\left[(y-a)^2 + (z+b)^2 + x^2\right]^{1/2}}\right] \Bigg\},
\end{aligned}
\qquad (3.29)
$$

$$
\begin{aligned}
G_y(x, y, z) = \frac{B_r}{4\pi\mu_0} \ln\Bigg\{ & \frac{(z+b) + \left[(z+b)^2 + (y-a)^2 + x^2\right]^{1/2}}{(z-b) + \left[(z-b)^2 + (y-a)^2 + x^2\right]^{1/2}} \\
& \times \frac{(z-b) + \left[(z-b)^2 + (y+a)^2 + x^2\right]^{1/2}}{(z+b) + \left[(z+b)^2 + (y+a)^2 + x^2\right]^{1/2}} \Bigg\},
\end{aligned}
\qquad (3.30)
$$

$$
\begin{aligned}
G_z(x, y, z) = \frac{B_r}{4\pi\mu_0} \ln\Bigg\{ & \frac{(y+a) + \left[(z-b)^2 + (y+a)^2 + x^2\right]^{1/2}}{(y-a) + \left[(z-b)^2 + (y-a)^2 + x^2\right]^{1/2}} \\
& \times \frac{(y-a) + \left[(z+b)^2 + (y-a)^2 + x^2\right]^{1/2}}{(y+a) + \left[(z+b)^2 + (y+a)^2 + x^2\right]^{1/2}} \Bigg\}.
\end{aligned}
\qquad (3.31)
$$

To solve the problem of ferrofluid movement in response to hydraulic and magnetic gradients, the coupled equations of fluid flow and of the magnetic field must be solved. In a porous medium fully-saturated with a FG these equations can be simplified, and analytical solution can be obtained for a known $H$ field [*Moridis and Oldenburg*, 1998]. In FG flow under most realistic (multi-phase) conditions, however, it does not appear possible to obtain analytical solutions even for the simplest one-dimensional problems [*Moridis and Oldenburg*, 1998]. Numerical solutions appear to be the only option.
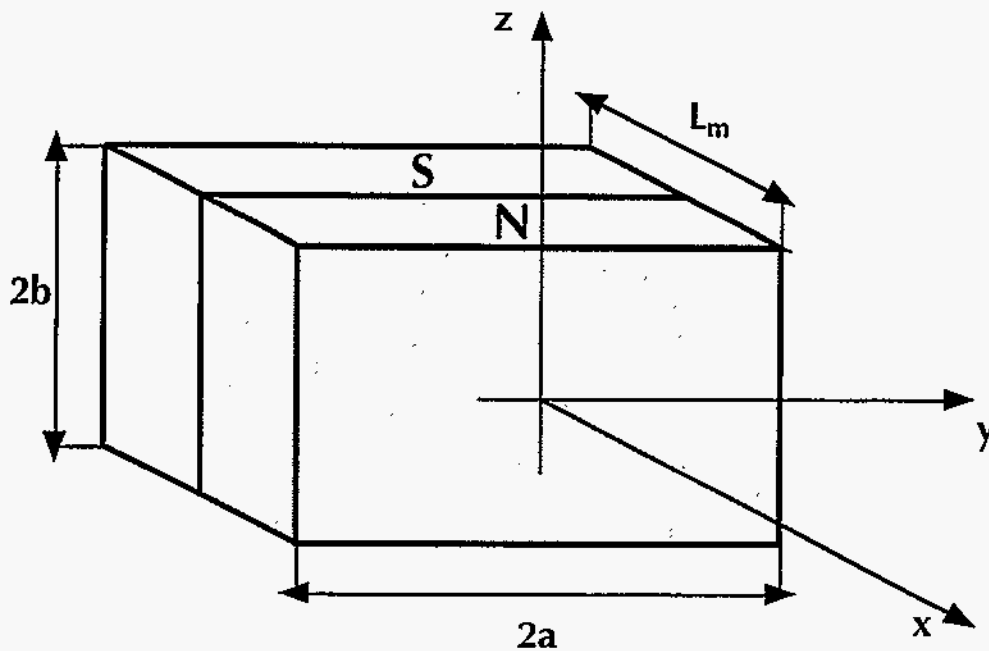
**Figure 3.2.** Local coordinate system for the magnetic field produced by a permanent magnet. The magnetic poles are a distance $L_m$ apart.

# 3.4. Analytical Solutions

An analytical solution to the problem of FG flow is only possible in one-dimensional domains and in porous media fully-saturated with the FG. Under these conditions, equations (3.12) and (3.19) are combined and then simplified, yielding

$$\frac{\partial}{\partial s}\left\{\frac{k\rho}{\mu}\left[\frac{\partial p}{\partial s}+\frac{\partial p_s}{\partial s}+\rho\left(-g_m\frac{\partial H}{\partial s}+g\frac{\partial z}{\partial s}\right)\right]\right\}=\frac{\partial}{\partial t}(\rho\phi)+W, \qquad (3.32)$$

where

$$g_m = g_m(s) = \frac{\mu_{mo}}{\rho}M, \qquad (3.33)$$

and the parameter $s$ can be either $x$ or $z$. For simplicity, equation (3.32) does not contain any subscripts, and all fluid properties are those of the FG. The following assumptions are made:

1. The fluid properties are invariant.
2. The magnetostrictive pressure is small and can be neglected. The reasons for the validity of this assumption are discussed in detail by *Rosensweig* [1985.]

We introduce the transformation

$$p = p_0(1 + p_r), \tag{3.34}$$

in which $p_0$ is the initial pressure and $p_r$ is the relative deviation from $p_0$. Equation (3.32) then becomes:

$$K p_0 \frac{\partial^2 p_r}{\partial s^2} + K \rho \frac{\partial}{\partial s} \left( -g_m \frac{\partial H}{\partial s} + g \frac{\partial z}{\partial s} \right) = S \frac{\partial p_r}{\partial t} + Q, \tag{3.35}$$

where

$$K = \frac{k}{\mu}, \quad S = \phi (\beta_\phi + \beta_\rho) p_0, \quad Q = \frac{W}{\rho}, \quad \beta_\phi = \frac{1}{\phi} \frac{\partial \phi}{\partial p} \quad \text{and} \quad \beta_\rho = \frac{1}{\rho} \frac{\partial \rho}{\partial p}. \tag{3.36}$$

The terms $\beta_\phi$ and $\beta_\rho$ are the pore and FG compressibilities, respectively.

For 1-D FG flow, when the $s$-axis of the magnet ($s \equiv x, z$) is aligned with the direction of flow, the component of the magnetic field in the $s$ direction is given by equation (3.28), i.e. $H_s = G_s(s) - G_s(s + L)$, and $G_s(s)$ is obtained from equation (3.29) as

$$G_s(s) = \frac{B_r}{\pi \mu_0} \left\{ \tan^{-1} \left[ \frac{ab}{s \left( a^2 + b^2 + s^2 \right)^{1/2}} \right] \right\}. \tag{3.37}$$

The $M$ $vs.$ $H$ relationship can be obtained from the ferrofluid magnetization curve (**Figure 2.1**). In our experience, an excellent fit can be provided by using a double-exponential function. For 1-D FG flow aligned with the $x$-axis of a magnet, the *magnetic gravity* $g_m$ of equation (3.33) can be accurately approximated by an exponential function of the distance $s$ from the pole of the magnet. **Figure 3.3** shows the accuracy of the approximation

$$g_m(x) \frac{\partial H(x)}{\partial s} = \frac{\mu_{m0}}{\rho} M(x) \frac{\partial H(x)}{\partial x} \simeq u_1 \exp(-u_2 x) \tag{3.38}$$

for the EMG 805$^{\text{TM}}$ and EMG-C$^{\text{TM}}$ ferrofluids (**Table 3.1**) and the PM1 and PM2 magnets (**Table 3.2**) used in the experimental work. (A more detailed discussion of the ferrofluids and of the magnets, as well as an explanation of the terms in **Table 3.2** can be found in Section 4). The values of $u_1$ and $u_2$ for a combination of ferrofluids and magnets appear in **Table 3.3**.

| Table 3.1. Properties of the EMG 805™ and EMG-C™ Ferrofluids | | |
|---|---|---|
| **Property** | **EMG 805™** | **EMG-C™** |
| Viscosity at 27 $^{0}$C | 2.5 cp | 8 cp |
| Magnetite concentration (vol/vol) | 3.7% | 5.2% |
| Surfactant concentration (vol/vol) | 8% | 10% |
| Water concentration (vol/vol) | 88.3% | 84.8% |
| Initial magnetic susceptibility | 0.49 | 0.49 |
| pH | 7 | 7 |
| Density | 1190 kg/m$^3$ | 2000 kg/m$^3$ |
| Saturation magnetization | $1.65 \times 10^4$ A/m | $3.07 \times 10^4$ A/m |

| Table 3.2. Magnets Used in the Experiments | | | |
|---|---|---|---|
| **Magnet Type** | **Description** | **Field** | **Dimensions** |
| Electromagnet | 2 parallel copper coils, $N_t \simeq 2000$ turns | $B = \dfrac{\mu_{m0} N_t I}{2 \pi \overline{R}}$ | $R_i = 0.011$ m<br>$R_o = 0.035$ m<br>$L = 0.025$ |
| Nd-Fe-B (PM1) | Permanent magnet<br>Rectangular shape<br>5 units, often stacked | $B_r = 1.2$ T<br>$H_c = 1.0$ T | $L_m = 0.0254$ m<br>$H = 0.05$ m<br>$W = 0.05$ m |
| Nd-Fe-B (PM2) | Permanent magnet<br>Rectangular shape | $B_r = 1.0$ T<br>$H_c = 1.0$ T | $L_m = 0.0254$ m<br>$H = 0.032$ m<br>$W = 0.032$ m |
| Nd-Fe-B (PM3) | Permanent magnet<br>Rectangular shape | $B_r = 1.1$ T<br>$H_c = 0.93$ T | $L_m = 0.0127$ m<br>$H = 0.0254$ m<br>$W = 0.0254$ m |
| Nd-Fe-B (PM4) | Permanent magnet<br>Magnetic rings, pole axis perpendicular to disk | $B_r = 1.1$ T<br>$H_c = 0.93$ T | $R_i = 0.005$ m<br>$R_o = 0.02$ m<br>$Z = 0.01$ m |
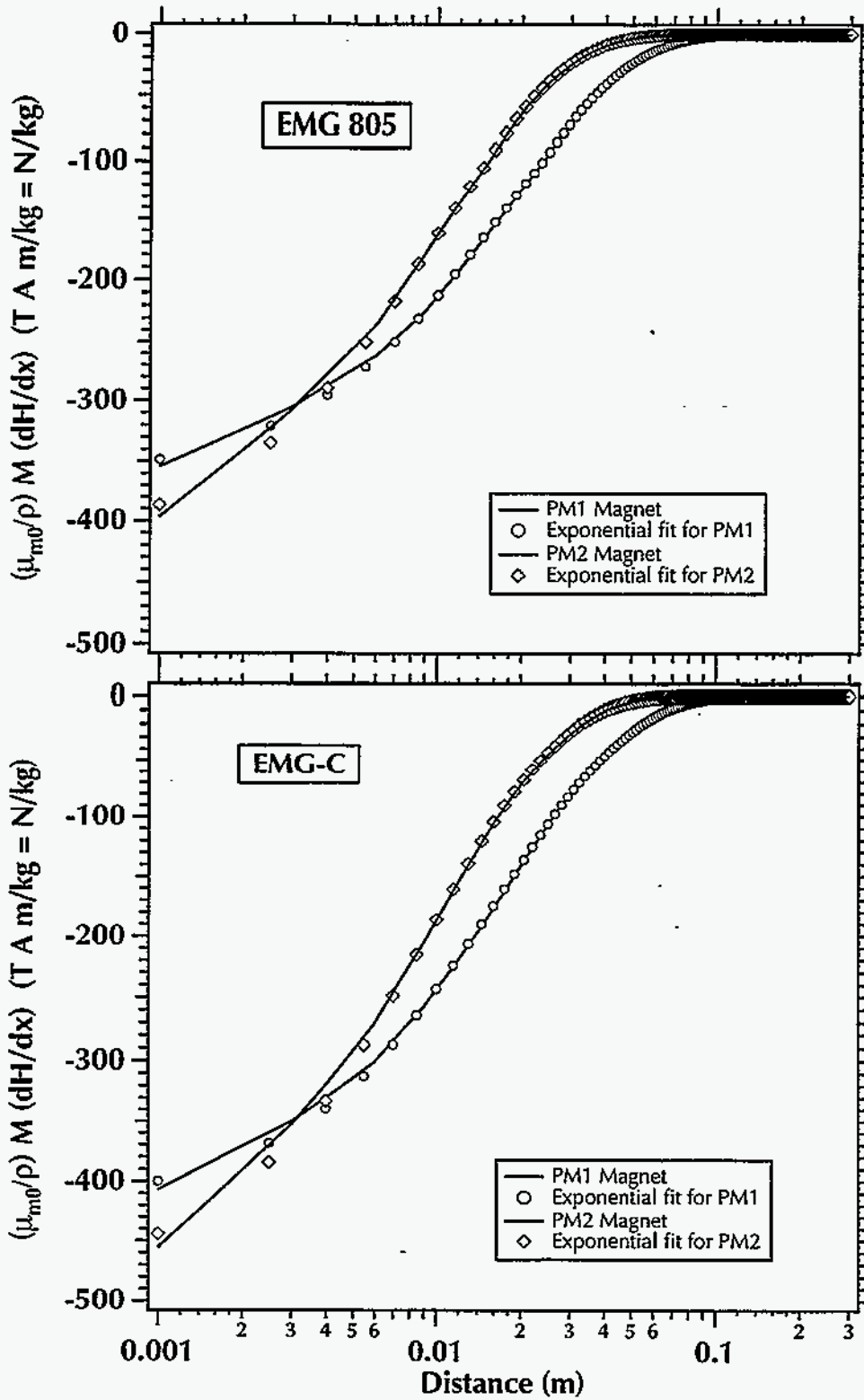
**Figure 3.3.** Comparison of analytical and fitted predictions of $g_m \frac{\partial H}{\partial s}$ (EMG 805$^{TM}$ ferrofluid and PM3 magnet).

| Table 3.3. $u_1$ and $u_2$ Values in Equation (3.38) | | |
|---|---|---|
| **Magnet+Ferrofluid** | $u_1$ (N/kg) | $u_2$ |
| PM1 + EMG 805$^{TM}$ | $-368.25$ | 55.124 |
| PM1 + EMG-C$^{TM}$ | $-422.87$ | 55.124 |
| PM2 + EMG 805$^{TM}$ | $-426.16$ | 96.477 |
| PM2 + EMG-C$^{TM}$ | $-489.38$ | 96.478 |

### 3.4.1. Pressure Distribution in a Horizontal FG Column

The equation of flux $q_x$ is obtained by combining equations (3.12), (3.36) and (3.38), yielding

$$q_x = -K \left\{ \frac{dp}{dx} - \rho u_1 \exp\left[-u_2(x + L_0)\right] \right\}, \qquad (3.39)$$

where $L_0$ is the distance between the magnetic pole and the porous medium. Under the static conditions (i.e. no flow in a closed horizontal domain subjected to a magnetic field $H$) shown in **Figure 3.4**, the pressure distribution along the $x$ axis can be obtained by setting $q_x = 0$ at all times. Then

$$\frac{dp}{dx} = \rho u_1 \exp\left[-u_2(x + L_0)\right] \quad \text{and} \quad p = C_p - \rho \frac{u_1}{u_2} \exp\left[-u_2(x + L_0)\right], \quad (3.40)$$

where $C_p$ a constant. For $x \to \infty$, $p \to C_p$, from which it is obvious that $C_p = p_0$, i.e. the initial pressure before the application of the magnetic field and before any flow events. In terms of $p_r$, equation (3.40) becomes

$$p_r = -\frac{\rho}{p_0} \frac{u_1}{u_2} \exp\left[-u_2(x + L_0)\right]. \qquad (3.41)$$

The distribution of $p_G = p_r \, p_0$, termed the *magnetopressure* for the EMG 805$^{TM}$ ferrofluid and the stacked PM1 magnet values is shown in **Figure 3.5**, and represents gauge pressures because $p_0$ is the atmospheric pressure. It is possible to use (3.41) to predict the pressure exerted by the EMG 805$^{TM}$ on the bottom of a closed horizontal column, provided the conditions of one-dimensional configuration discussed above are met.
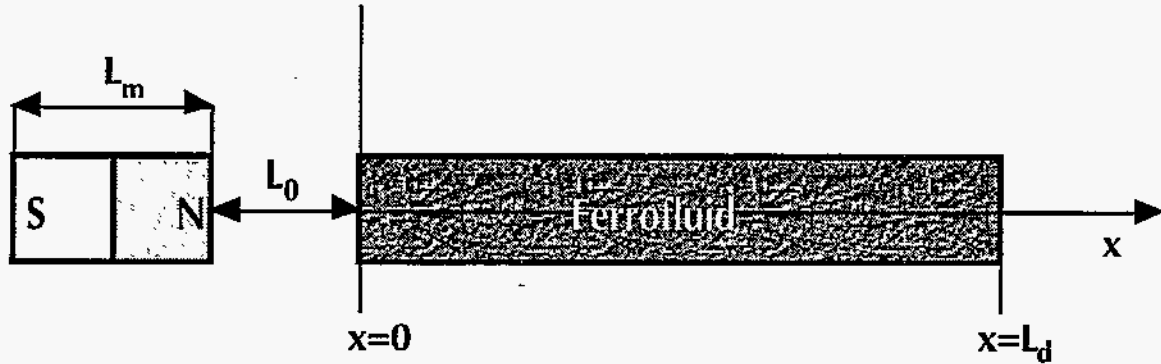
**Figure 3.4.** Configuration of the 1-D horizontal FG system.

## 3.4.2. Pressure Distribution in a Vertical FG Column

For the configuration shown in case (a) in **Figure 3.6**, the equation of flux $q_z$ is obtained in a manner similar to that of (3.39), yielding

$$q_z = -K \left\{ \frac{dp}{dz} + \rho\, u_1 \exp\left[-u_2(z + L_0)\right] - \rho\, g \right\}, \tag{3.42}$$

where $L_0$ is the distance between the magnetic pole and the porous medium. Setting $q_z = 0$ and integrating results in

$$p = C_v + \rho\, g\, z + \rho\, \frac{u_1}{u_2} \exp\left[-u_2(z + L_0)\right]. \tag{3.43}$$

It is easy to show that $C_v = p_0$. In terms of $p_r$, equation (3.43) becomes

$$p_r = \frac{\rho g}{p_0} z + \frac{\rho}{p_0} \frac{u_1}{u_2} \exp\left[-u_2(z + L_0)\right]. \tag{3.44}$$

The $p_r$ for case (b) is obtained in an entirely analogous manner, resulting in

$$p_r = \frac{\rho g}{p_0} z - \frac{\rho}{p_0} \frac{u_1}{u_2} \exp\left[-u_2(L_0 + L_d - z)\right], \tag{3.45}$$

where $L_d$ is the column length. For the EMG 805[TM] ferrofluid and the PM1 magnet, the $p_G$ distributions in the vertical columns of **Figure 3.6** are shown in **Figures 3.7** and **3.8** for cases (a) and (b), respectively. The calculations for case (b) are based on an $L_d = 0.3$ m. The length of the portion of the FG column suspended against gravity by the magnetic field is determined from **Figure 3.7** as the $z$ at which $p_G = p_r\, p_0 = 0$.
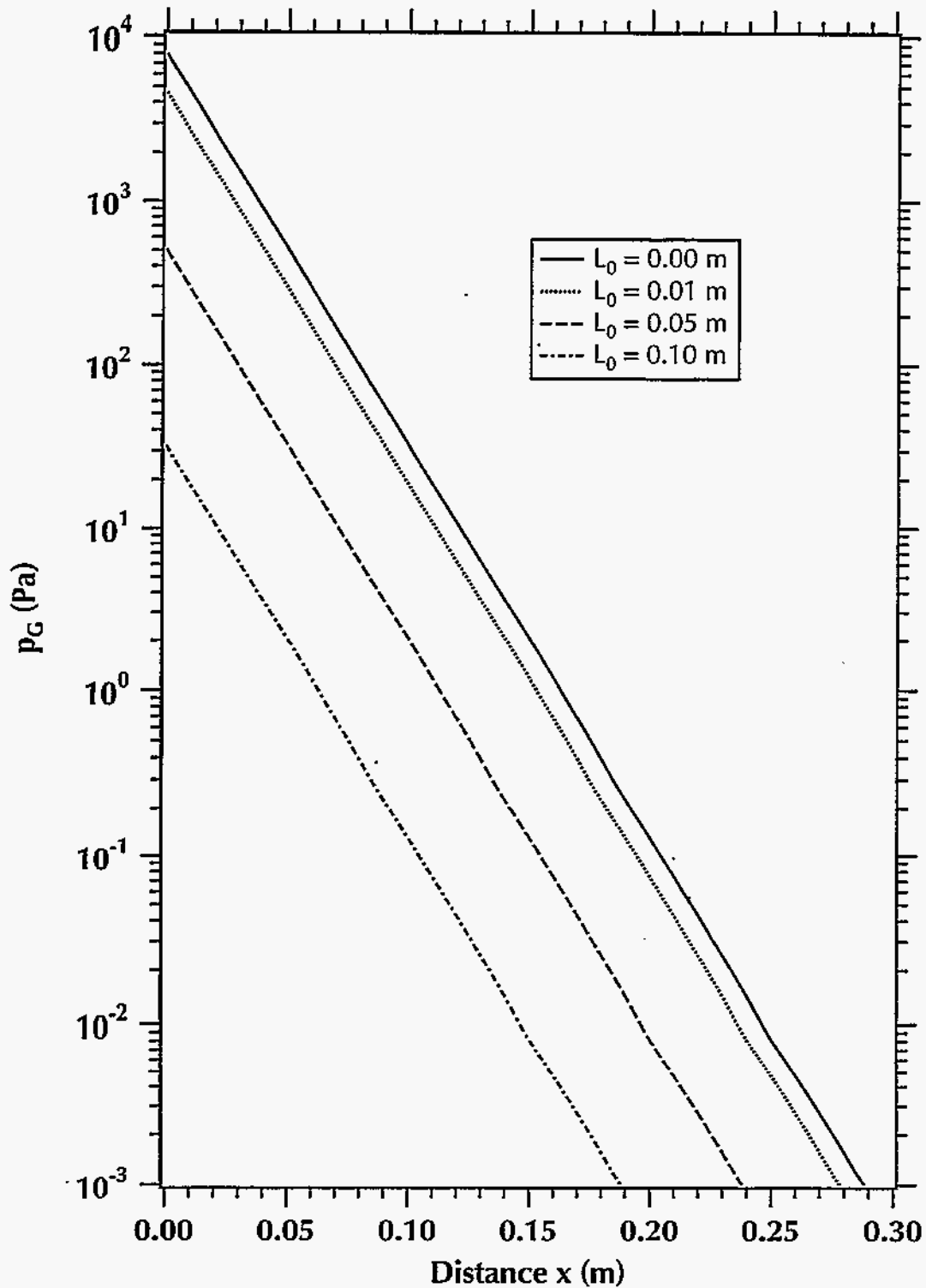
**Figure 3.5.** Distribution of $p_G = p - p_0$ (i.e., the gauge pressure) in the horizontal column in **Figure 3.4** for various $L_0$. The ferrofluid is EMG 805[TM] and the magnet is PM1.

**Case (a)**

**Case (b)**

$z=0$

S

$L_m$

N

$L_0$

$z=0$

Ferrofluid

$z=L_d$

z

Ferrofluid

$z=L_d$

$L_0$

N

$L_m$

S

z
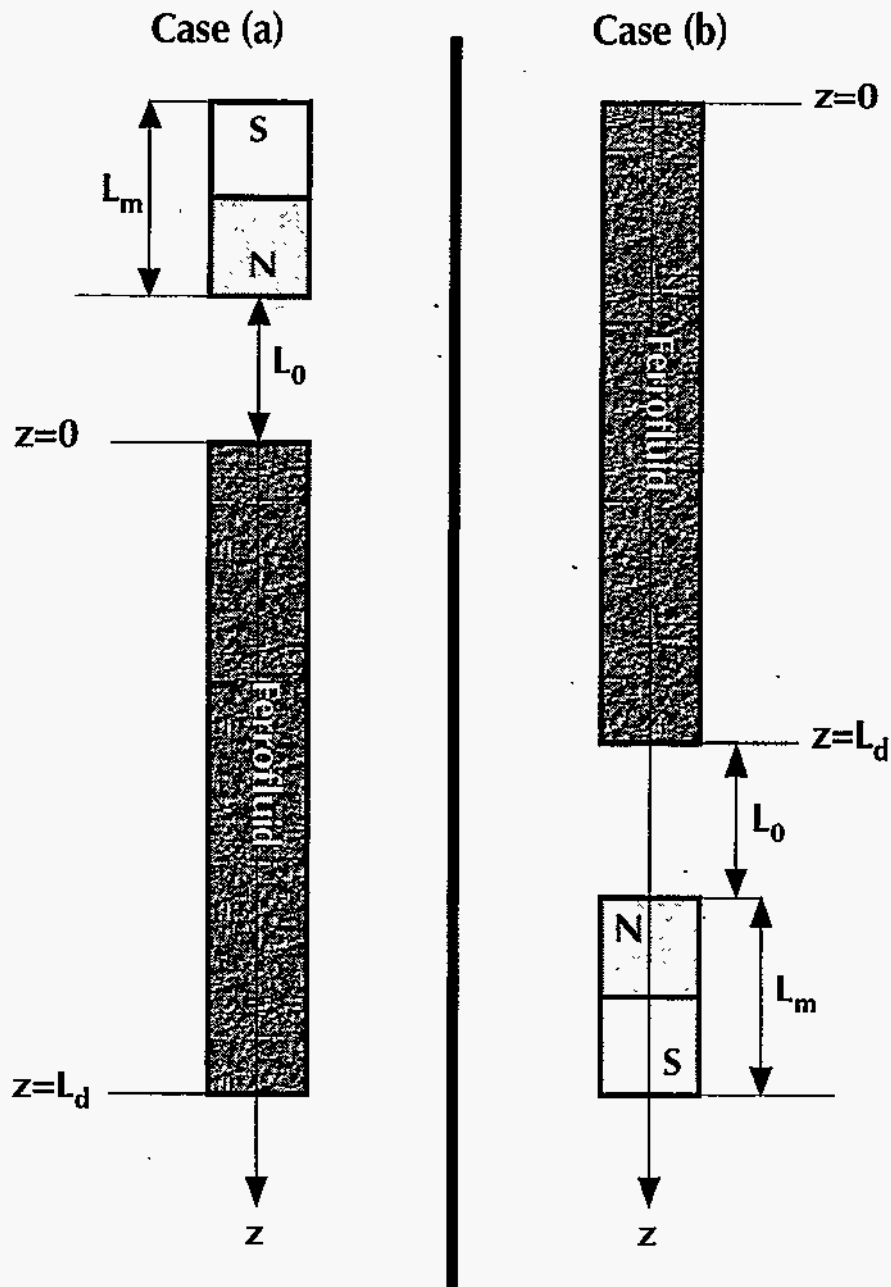
**Figure 3.6.** Possible configurations of the 1-D vertical FG system.
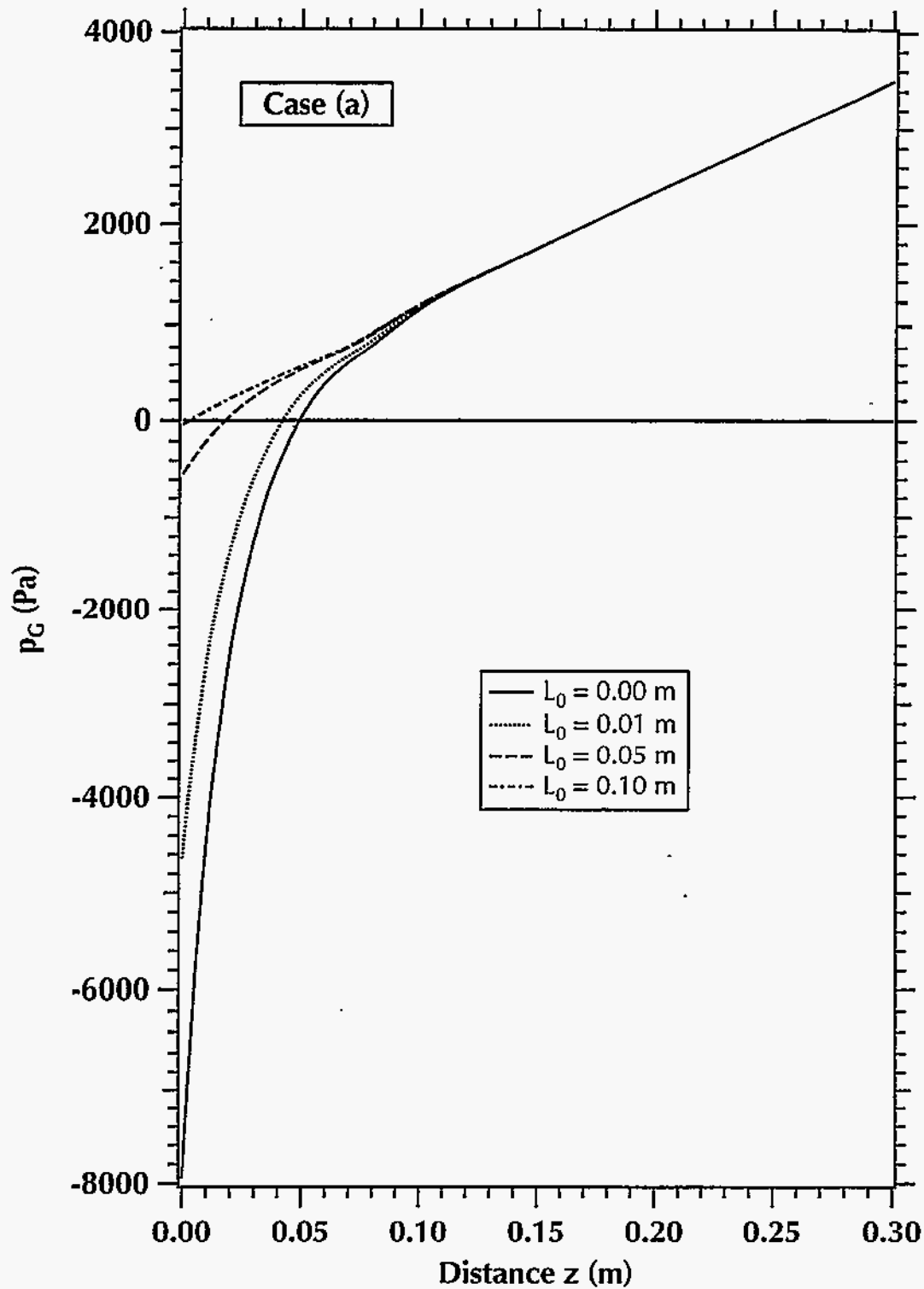
**Figure 3.7.** $p_G$ (gauge) distribution in case (a) of the vertical FG column of **Figure 3.6** (EMG 805™ ferrofluid and PM1 magnet).
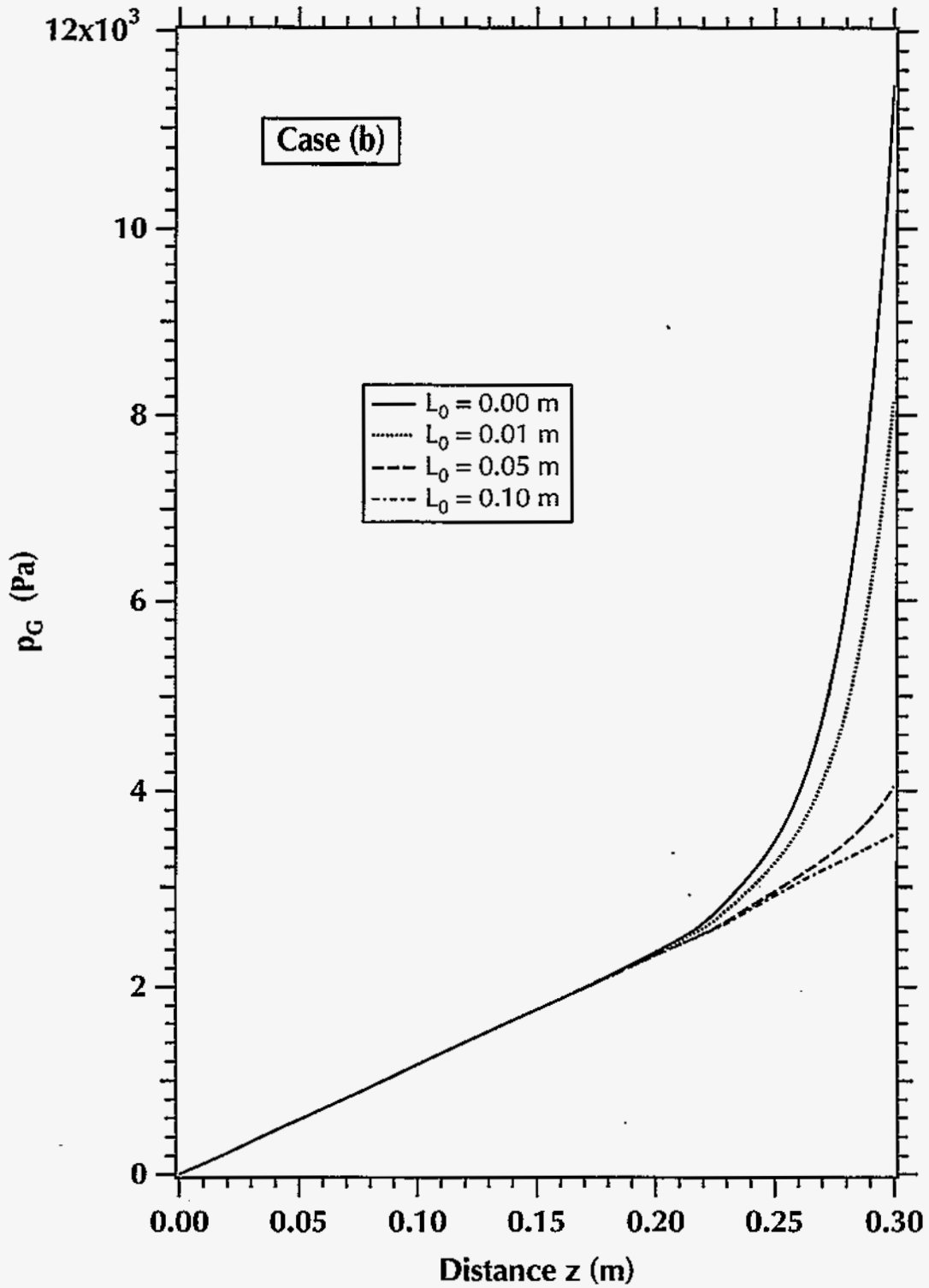
**Figure 3.8.** $p_G$ (gauge) distribution in case (b) of the vertical FG column of **Figure 3.6** with $L_d = 0.3$ m (EMG 805$^{TM}$ ferrofluid and PM1 magnet).

### 3.4.3. 1-D Flow in a Semi-Infinite Horizontal FG System With Known Flux at the x=0 Boundary

We consider one-dimensional horizontal FG flow in the configuration shown in **Figure 3.4.** The column is semi-infinite, i.e. $L_d \to \infty$. For $t > 0$, ferrofluid is produced at a constant rate $W$ at $x = 0$. Setting $s \equiv x$, the equation of flow is obtaining by combining (3.35) and (3.38), resulting in

$$K\, p_0 \frac{\partial^2 p_r}{\partial x^2} + T_0 \exp[-u_2(x + L_0)] = S \frac{\partial p_r}{\partial t}, \qquad (3.46)$$

where $T_0 = K \rho\, u_1\, u_2$.

Taking the Laplace transform of both sides of equation (3.46) and rearranging the terms of the equation yields

$$K\, p_0 \frac{d^2 \Psi}{dx^2} - S \lambda \Psi = -\frac{T_0}{\lambda} \exp[-u_2(x + L_0)] - S\, p_r(t = 0), \qquad (3.47)$$

where

$$\Psi = \mathcal{L}\{p_r\} \qquad (3.48)$$

and $\lambda$ is the Laplace space parameter. The term $p_r(t = 0)$ corresponds to the initial pressure distribution, i.e. when the magnetic field is active but before the initiation of flow. This is supplied by equation (3.41), resulting in

$$K\, p_0 \frac{d^2 \Psi}{dx^2} - S \lambda \Psi = T \exp[-u_2(x + L_0)], \qquad (3.49)$$

where

$$T = S \frac{\rho}{p_0} \frac{u_1}{u_2} - \frac{T_0}{\lambda}. \qquad (3.50)$$

Equation (3.49) is a linear, 2nd order ordinary differential equation, with the following general solution:

$$\Psi = A_1 \exp[(\omega\sqrt{\lambda})\, x)] + A_2 \exp[(-\omega\sqrt{\lambda})\, x] + A_3 \exp[-u_2(x + L_0)], \qquad (3.51)$$

where

$$\omega = \sqrt{\frac{S}{Kp_0}}.$$
(3.52)

From the boundary condition at $x \to \infty$ we have:

$$p_r(x \to \infty) = 0, \quad \text{i.e.} \quad \Psi(x \to \infty) = 0 \quad \text{and thus} \quad A_1 = 0.$$
(3.53)

At the $x = 0$ boundary

$$Q = -Kp_0 \left[ \frac{\partial p_r}{\partial x} - \frac{\rho\, u_1}{p_0} \exp(-u_2\, L_0) \right],$$
(3.54)

from which

$$\frac{d\Psi}{dx}(x=0) = \frac{1}{\lambda}\left[ -\frac{Q}{Kp_0} + \frac{\rho\, u_1}{p_0} \exp(-u_2\, L_0) \right].$$
(3.55)

Differentiating (3.51) and equating to (3.55) at $x = 0$ yields

$$-A_2\, \omega\sqrt{\lambda} - A_3\, u_2 \exp(-u_2\, L_0) = \frac{1}{\lambda}\overbrace{\left[ -\frac{Q}{Kp_0} + \frac{\rho\, u_1}{p_0} \exp(-u_2\, L_0) \right]}^{\gamma_1} = \frac{\gamma_1}{\lambda}.$$
(3.56)

Substituting $\Psi$ from (3.51) in (3.49) and carrying out the differentiations yields

$$A_2\, \lambda\, (K p_0\, \omega^2 - S) \exp(-\omega\sqrt{\lambda}\, x)$$
$$+ A_3 \left(K p_0\, u_2^2 - S\, \lambda\right) \exp[-u_2(x + L_0)] = T \exp[-u_2(x + L_0)].$$
(3.57)

The quantity $Kp_0\omega^2 - S = 0$, $A_3$ is determined as

$$A_3 = \frac{T}{Kp_0\, u_2^2 - S\, \lambda} = \frac{\overbrace{\dfrac{\rho}{p_0}\dfrac{u_1}{u_2}}^{\gamma_2} - \dfrac{T_0}{S}\dfrac{1}{\lambda}}{\underbrace{\dfrac{Kp_0\, u_2^2}{S}}_{\gamma_3} - \lambda} = \frac{T_0}{S}\frac{1}{\lambda(\lambda - \gamma_3)} - \frac{\gamma_2}{\lambda - \gamma_3}.$$
(3.58)

The term

$$\frac{1}{\lambda\,(\lambda - \gamma_3)} = -\frac{1}{\gamma_3}\left( \frac{1}{\lambda} - \frac{1}{\lambda - \gamma_3} \right).$$
(3.59)

Substituting in equation (3.58) and using the equality $\gamma_2 = T_0/(S\gamma_3)$ leads to

$$A_3 = -\frac{\gamma_2}{\lambda} \qquad (3.60)$$

· Then $A_2$ is then determined from (3.56) as

$$A_2 = \gamma_4 \frac{1}{\lambda^{3/2}}, \qquad (3.61)$$

where

$$\gamma_4 = \frac{1}{\omega}\left[-\gamma_1 + \gamma_2 u_2 \exp(-u_2 L_0)\right] = \frac{1}{\omega}\frac{Q}{K\,p_0} \qquad (3.62)$$

The Laplace-space equation of FG flow is obtained by substituting for $A_2$ and $A_3$ in equation (3.51):

$$\Psi(x, \lambda) = \gamma_4 \frac{\exp[(-\omega\sqrt{\lambda})\,x]}{\lambda^{3/2}} - \gamma_2 \exp[-u_2(x + L_0)]\frac{1}{\lambda}. \qquad (3.63)$$

The equation of $p_r = p_r(x, t)$ is obtained by inverting the Laplace space solution of equation (3.61), i.e.

$$p_r(x, t) = \mathcal{L}^{-1}\{\Psi(x, \lambda)\}, \qquad (3.64)$$

and after the appropriate substitutions yields

$$p_r = \gamma_4\left[2\sqrt{\frac{t}{\pi}}\exp\left(-\frac{\omega^2 x^2}{4t}\right) - (\omega\,x)\,\mathrm{erfc}\left(\frac{\omega\,x}{2\sqrt{t}}\right)\right] - \gamma_2\exp[-u_2(x+L_0)]. \qquad (3.65)$$

The first part of equation (3.65) does not include any magnetic terms. It represents the analytical solution of flow in a horizontal system under the initial and boundary conditions discussed above and in the absence of a magnetic field. All the magnetic effects are accounted for in the second part of equation (3.65).

We now consider an example of flow in a configuration such as the one in **Figure 3.4.** The porous medium in the column has $\phi = 0.46$ and $k = 10^{-13}$ m$^2$. The ferrofluid is EMG 805$^{\mathrm{TM}}$ with $\rho = 1200$ kg/m$^3$ and $\mu = 2 \times 10^{-3}$ Pa·s. The porous medium and

FG compressibilities are $\beta_\phi = 0$ Pa$^{-1}$ and $\beta_\rho = 5 \times 10^{-10}$ Pa$^{-1}$ respectively. The PM1 magnet is located at a distance of $L_0 = 0$ m and $L_0 = 0.01$ m from the column. For this combination of magnet and ferrofluid, we have shown the accuracy of exponential relationship of equation (3.38) with $u_1 = -368.25$ and $u_2 = 55.124$. The horizontal column is initially at a pressure $p_0 = 1.2 \times 10^5$ Pa, and $p(x \to \infty) = p_0$. At $t = 0$, FG is produced at the $x = 0$ boundary at a rate $Q = 10^{-6}$ m/s.

**Figures 3.9** and **3.10** show the pressure distributions for $L_0 = 0$ m and $L_0 = 0.01$ m, respectively. As expected, for very early times ($t = 10^{-5}$ s) the pressure distribution is practically identical to that predicted by equation (3.41). It is very interesting to note that contrary to traditional flow through porous media, in **Figure 3.9** we observe flow from a low pressure to a high pressure due to the presence of the magnetic field.

### 3.4.4. 1-D Flow in a Semi-Infinite Horizontal FG System With Known Pressure at the x=0 Boundary

If $p_B$ is the pressure at the $x = 0$ boundary, then $p_r(x = 0) = p_{rb} = (p_B/p_0) - 1$ ($p_{rb} < 0$). Applying equation (3.51) at $x = 0$, we have

$$\Psi(x = 0) = A_2 + A_3 \exp(-u_2 L_0) = \frac{p_{rb}}{\lambda} \qquad (3.66)$$

The $A_3$ coefficient is determined from equation (3.60). The $A_3$ coefficient is obtained from (3.66) and (3.60) as

$$A_2 = \gamma_5 \frac{1}{\lambda} \qquad (3.67)$$

where

$$\gamma_5 = p_{rb} + \gamma_2 \exp(-u_2 L_0). \qquad (3.68)$$

The Laplace-space equation of FG flow is obtained by substituting for $A_2$ and $A_3$ in equation (3.51):

$$\Psi(x, \lambda) = \gamma_5 \frac{\exp[(-\omega\sqrt{\lambda})x]}{\lambda} - \gamma_2 \exp[-u_2(x + L_0)]\frac{1}{\lambda}. \qquad (3.69)$$

Inversion of equation (3.69) returns

$$p_r(x, t) = \gamma_5 \operatorname{erfc}\left(\frac{\omega x}{2\sqrt{t}}\right) - \gamma_2 \exp[-u_2(x + L_0)]. \qquad (3.70)$$

**Figure 3.9.** $p_r$ distribution for $L_0 = 0$ m in the horizontal FG column of **Figure 3.4** when the flow rate at the $x = 0$ boundary is defined (EMG 805[TM] ferrofluid and PM1 magnet).

**Figure 3.10.** $p_r$ distribution for $L_0 = 1$ m in the horizontal FG column of **Figure 3.4** when the flow rate at the $x = 0$ boundary is defined (EMG 805[TM] ferrofluid and PM1 magnet).

At the $x = 0$ boundary

$$\mathcal{L}\{Q\} = -K\,p_0 \left[ \frac{\partial \Psi}{\partial x}(x = 0) - \frac{\rho\,u_1}{p_0} \exp(-u_2\,L_0)\,\frac{1}{\lambda} \right].$$ (3.71)

From equation (3.69),

$$\frac{\partial \Psi}{\partial x}(x = 0) = -\gamma_5\,\omega\,\frac{1}{\lambda^{1/2}} + \gamma_2\,u_2 \exp(-u_2\,L_0)\frac{1}{\lambda}.$$

Substitution in (3.71) results in

$$\mathcal{L}\{Q\} = K\,p_0\,\gamma_5\,\omega\,\frac{1}{\lambda^{1/2}},$$ (3.72)

from which the variable flux $Q$ at $x = 0$ is obtained as

$$Q = Q(t) = \mathcal{L}^{-1}\{Q\} = K\,p_0\,\gamma_5\,\omega\,\frac{1}{\sqrt{\pi\,t}}.$$ (3.73)

In the horizontal system of the example discussed in the previous section, the boundary condition at $x = 0$ is changed from constant $Q$ to a constant $p_B = 10^5$ Pa. **Figures 3.11** and **3.12** show the pressure distributions for $L_0 = 0$ m and $L_0 = 0.01$ m, respectively. As expected, for very early times ($t = 10^{-5}$ s) the pressure distribution is practically identical to that predicted by equation (3.41). We note the flow from a low pressure to a high pressure due to the presence of the magnetic field. This effect appears to be more pronounced than in the case of constant $Q$ at the $x = 0$ boundary.

For the same example, the time-variable flow $Q$ at the $x = 0$ boundary is shown in **Figure 3.13**. The effect of the magnetic field is demonstrated by the upward shift of the $Q$ curve, which appears as a line in the log-log graph. As expected, increasing $L_0$ reduces $Q$, and the corresponding $Q$ curve shifts downward toward the $Q$ curve corresponding to no (or negligible) magnetic effects.
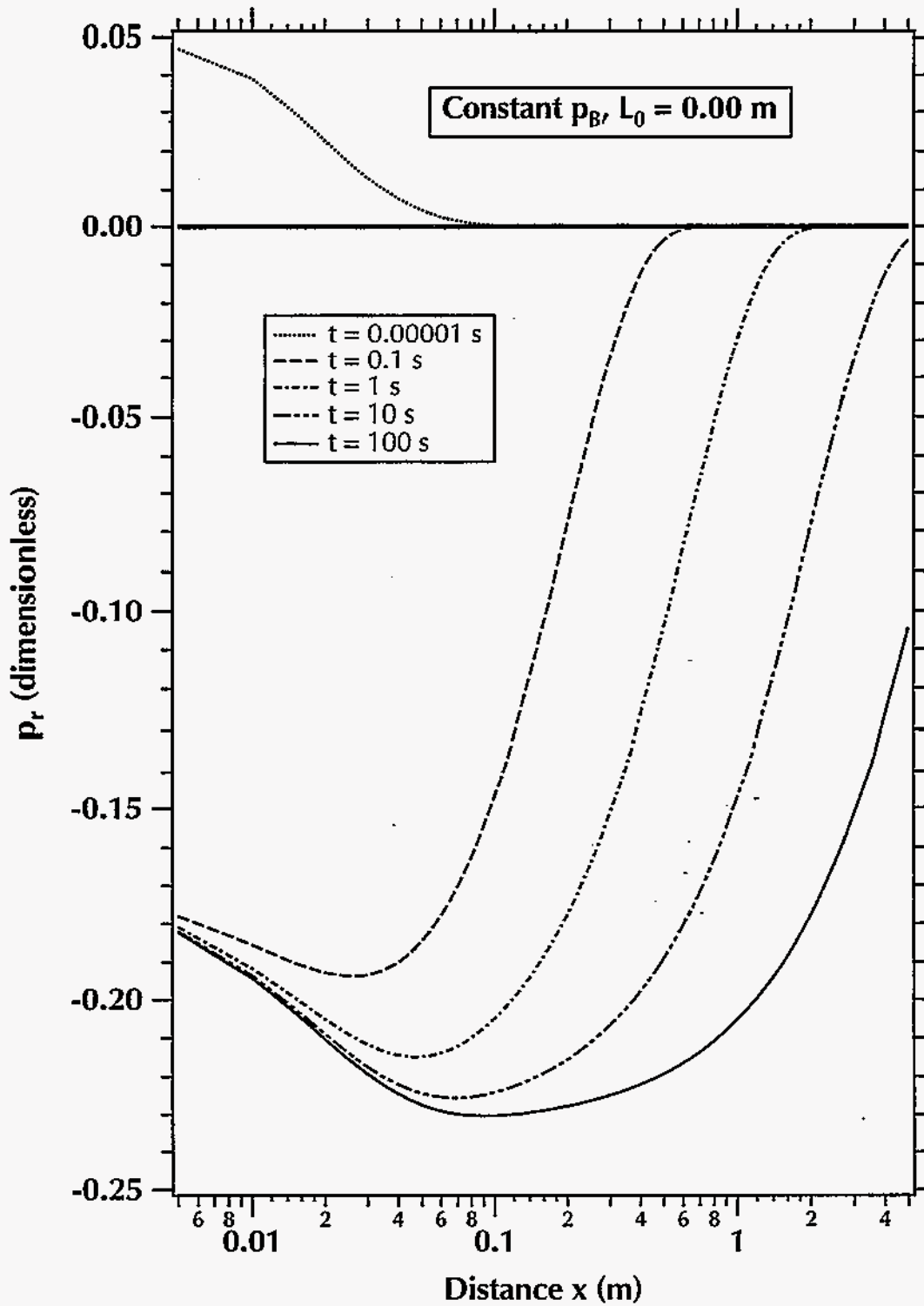
**Figure 3.11.** $p_r$ distribution for $L_0 = 0$ m in the horizontal FG column of **Figure 3.4** when the pressure at the $x = 0$ boundary is defined (EMG 805™ ferrofluid and PM1 magnet).
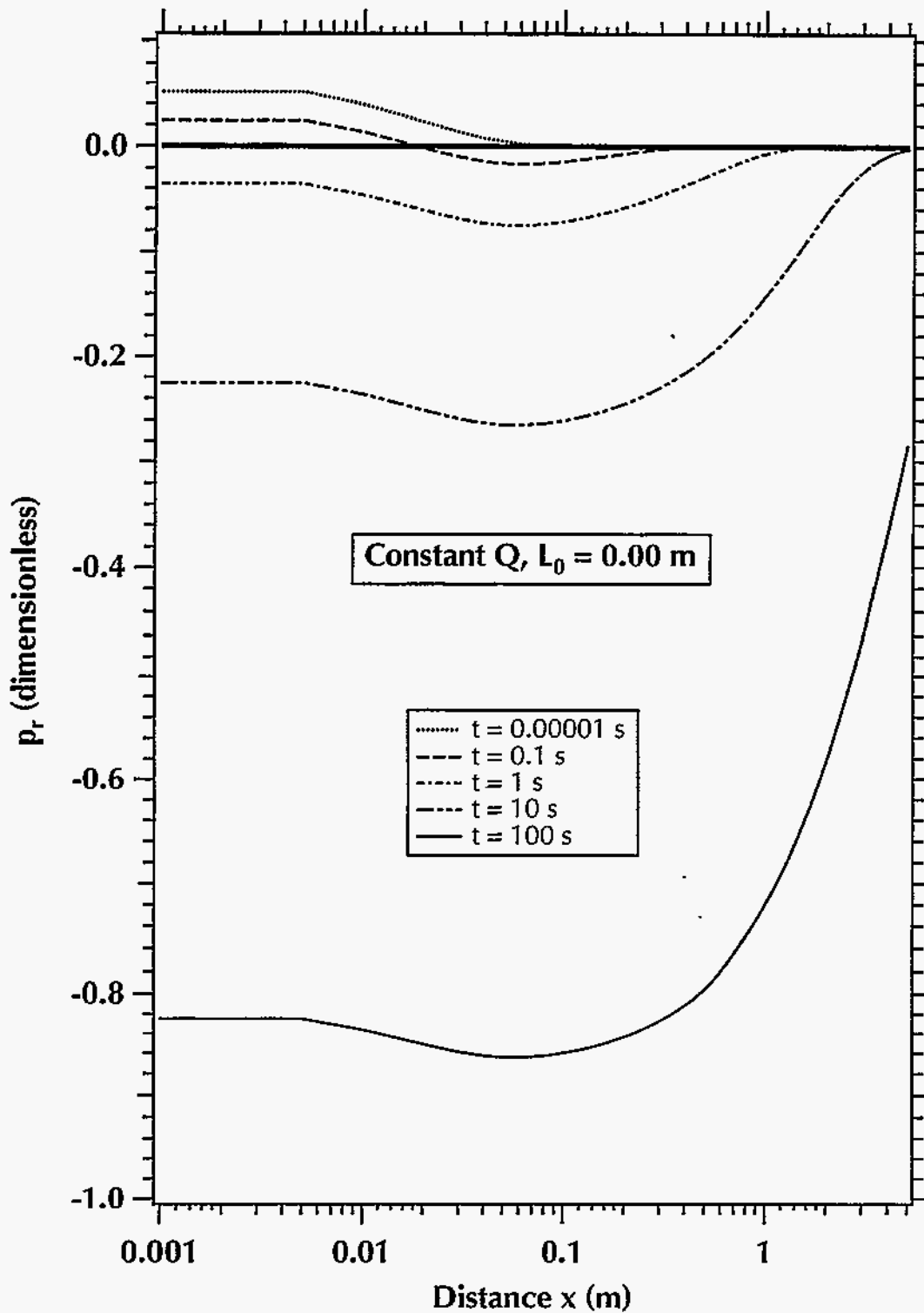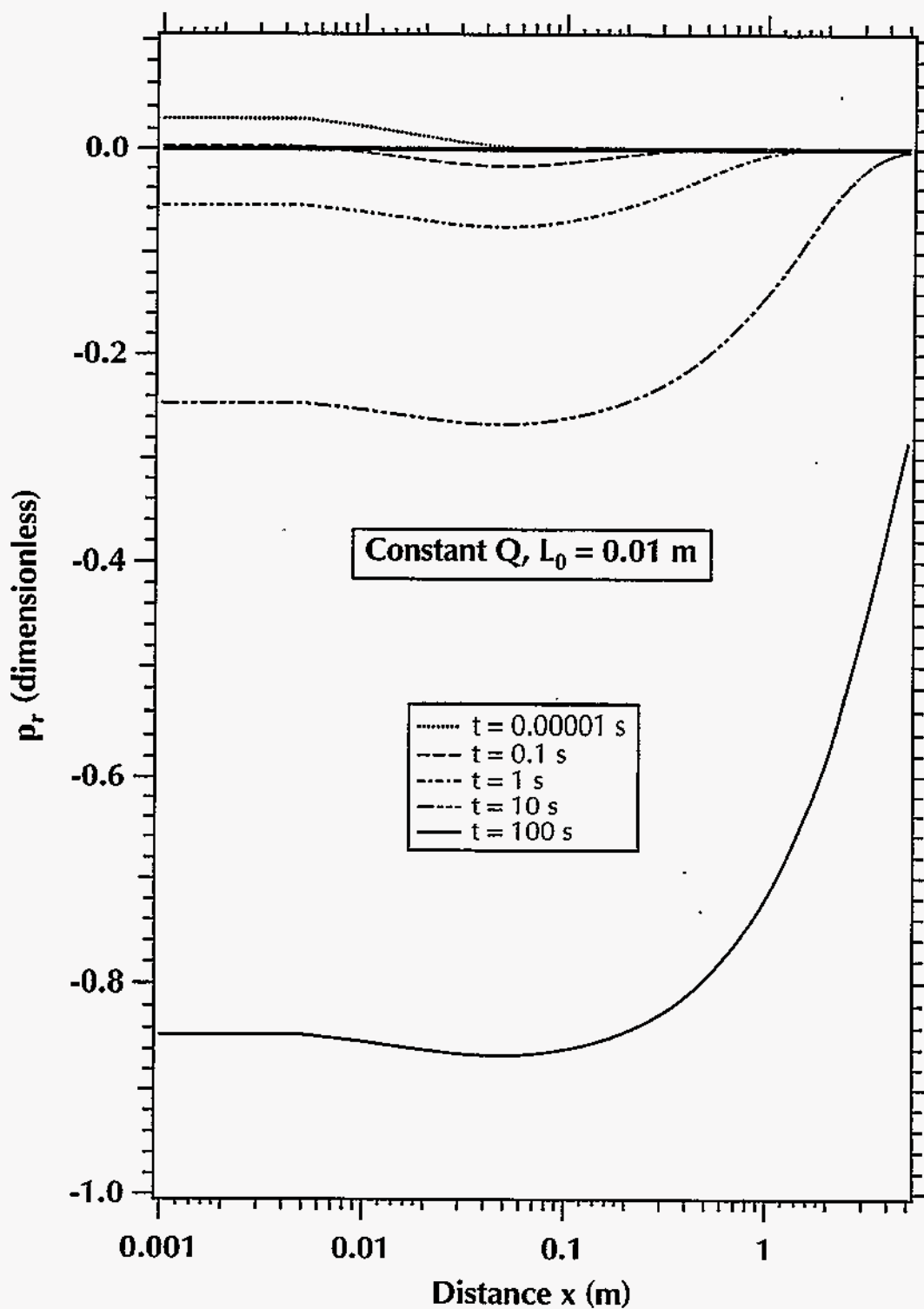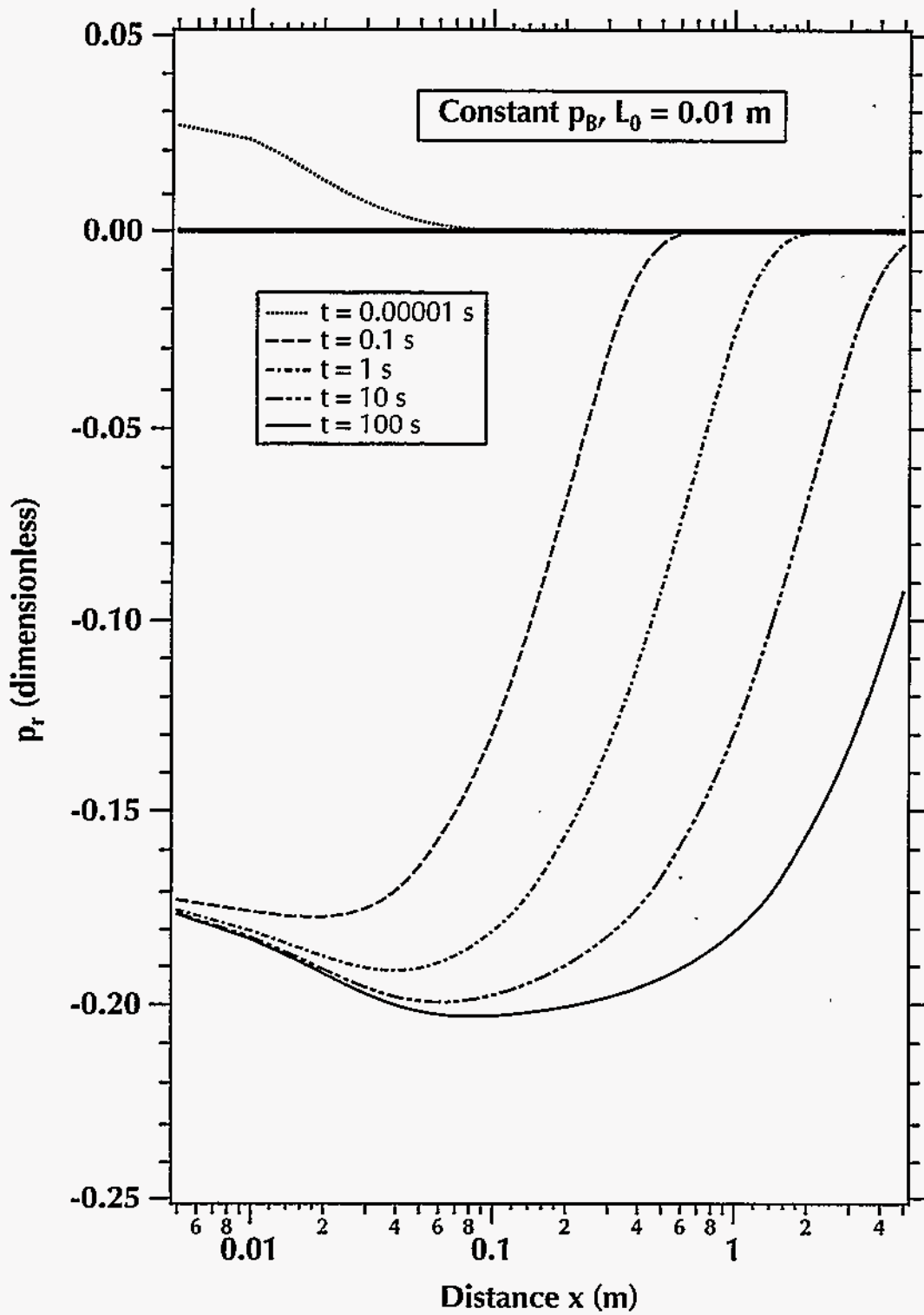
**Figure 3.12.** $p_r$ distribution for $L_0 = 1$ m in the horizontal FG column of **Figure 3.4** when the pressure at the $x = 0$ boundary is defined (EMG 805™ ferrofluid and PM1 magnet).
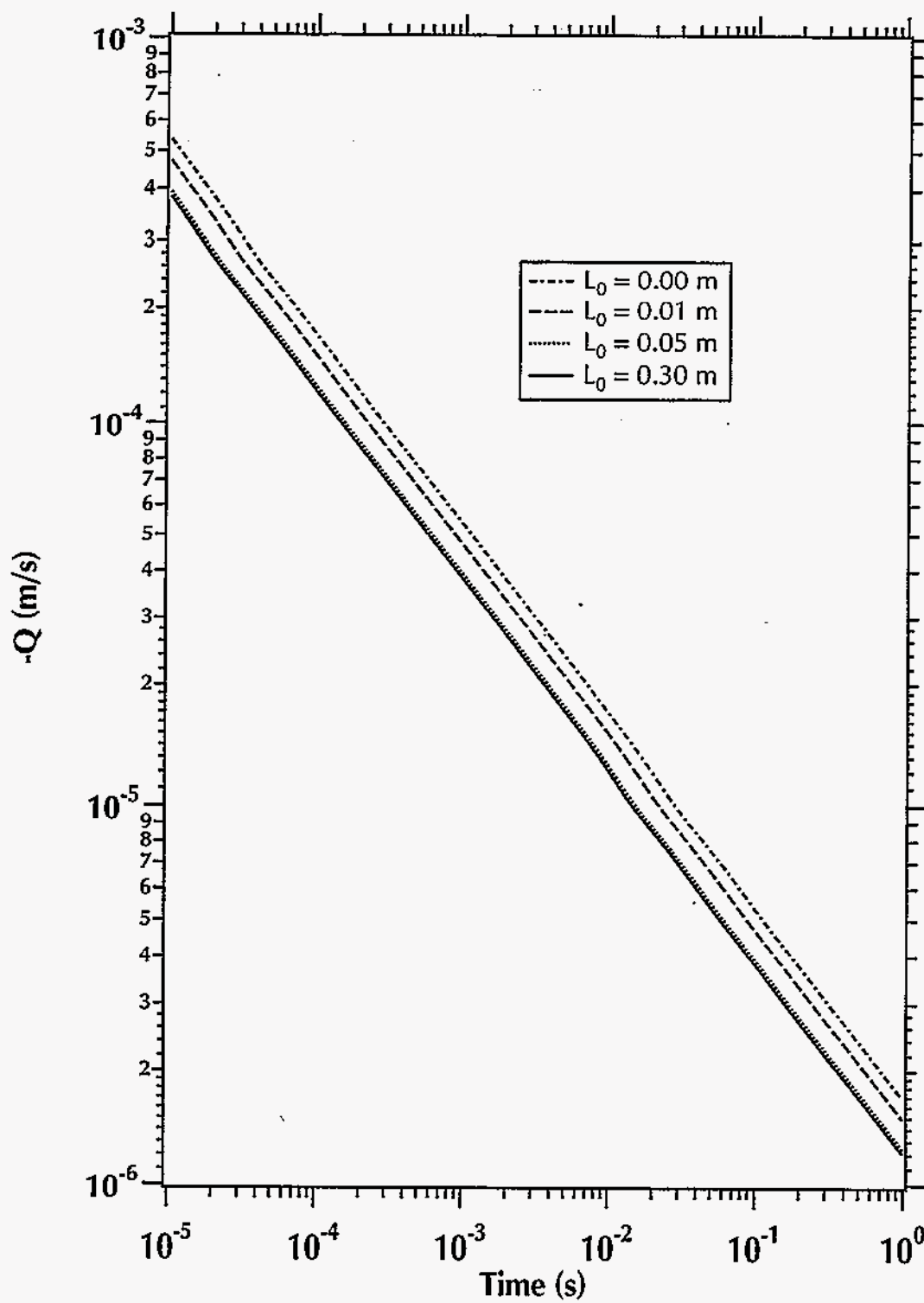
**Figure 3.13.** $Q = Q(t)$ for variable $L_0$ when the pressure at the $x = 0$ boundary is defined (EMG 805$^{TM}$ ferrofluid and PM1 magnet).

# 4. EXPERIMENTAL STUDIES OF FG FLOW

In this section we discuss experimental investigations of FG flow under a variety of conditions. These laboratory experiments address the issue of feasibility of inducing flow of ferrofluids with permanent magnets or electromagnets, and involve the movement of ferrofluids (i) against gravity in a tube, (ii) in a Hele-Shaw cell, and (iii) through porous media. Results are presented in terms of *magnetopressure*, i.e. a concept we introduce to describe the pressure induced by the ferrofluid in the presence of a magnetic field.

## 4.1. Materials

The two FGs used in this study, i.e. EMG 805$^{TM}$ and EMG-C$^{TM}$, were obtained from Ferrofluidics Corporation (Nashua, NH). **Table 3.1** summarizes the physical properties of the two aqueous ferrofluids. Both these ferrofluids are water based, i.e. the carrier liquid is water. The stabilization of the magnetic particles is achieved by means of a water-soluble dispersant (detergent). To avoid potentially detrimental effects of the negatively-charged soil particles on the ferrofluid stability, anionic dispersants and a near-neutral pH were used. All the concentrations in **Table 3.1** are by volume.

An electromagnet and a set of Neodymium-Iron-Boron (Nd-Fe-B) permanent magnets were used to create the magnetic fields which induced FG flow in the experiments (**Table 3.2**). For ease of differentiation, we refer to the permanent magnets as PM1, PM2, PM3 and PM4. The terms $I$ and $\overline{R}$ in the electromagnet of **Table 3.2** correspond to the electric

current and the average radius, i.e., $\overline{R} = (R_i + R_o)/2$. $R_i$ and $R_o$ are the inner and outer radius of the coil (in the case of the electromagnet) or of the magnetic ring (in the case of PM4). The terms $H$ and $W$ are the height and width of the rectangular permanent magnets, while $Z$ is the thickness of the magnetic disk in PM4. The five units of PM1 magnets were often used in a stacked arrangement, which was equivalent to a single long magnet with $L_0$ = 0.127 m.

The term $B_r$ is the residual induction of the permanent magnets, which is the induction at the point at which the hysteresis loop crosses the $B$ axis at zero magnetizing force, and represents the maximum flux output from the given magnet (i.e. at zero air gap). $H_c$ is the coercive force, and gives the measure of the demagnetizing force necessary to reduce an observed induction $B$ to zero after the permanent magnet has previously been brought to saturation.

# 4.2. Experiment 1: FG Movement in Response to Magnetic Fields

## 4.2.1. Vertical FG Movement

To observe the ferrofluid moving against gravity under the influence of a magnetic field, the EMG 805™ ferrofluid was placed in a 0.4 m long Teflon tube (6.35 mm (0.25 in) OD, 3.18 mm (0.125 in) ID) bent in a U-shape. The fluid filled the tube to a height of 0.1 m from each end of the U-shaped tube. The magnetic field used in these experiments was provided by an electromagnet or a permanent magnetic ring (**Table 3.2**). These magnets were positioned in the vicinity of the air-ferrofluid interface on the vertical portion of one side of the tube, and the effects of the magnetic field were determined by measuring the movement of the interface.

The electromagnet caused a 2.5 mm rise of the ferrofluid in the tube when the current through the coil was $I = 0.4$ A. This current produced a field strength of approximately 5.5 A/m. This rise was accompanied by a corresponding decrease of 2.5 mm in the fluid height of the other end of the tube. When the current was interrupted, the ferrofluid returned to the initial equilibrium position in the tube. When the direction of the current was reversed, the fluid moved in the same direction with the same magnitude, i.e. the interface moved upward by 2.5 mm. This observation illustrates the fact that an external magnetic field applied to a ferrofluid always causes attractive forces. Reversing the polarity will reverse the polarity of the ferrofluid particles, but the forces will still be attractive and the ferrofluid will move in the same direction.

The balance of forces acting on a ferrofluid is given by the ferrohydrodynamic Bernoulli equation [*Rosenweig*, 1985]. The rise $\Delta h$ of the FG level in response to a magnetic field normal to the FG-air interface is thus computed as

$$\Delta h = \frac{1}{\rho g} \left( \mu_{0m} \overline{M} H + \frac{1}{2} \mu_{0m} M^2 \right), \qquad (4.1)$$

where $\overline{M}$ is the average magnetization and the other terms are as previously defined (Sections 2 and 3). For the EMG 805™ ferrofluid and the electromagnetic coil described in **Table 3.2**, this equation predicts a $\Delta h = 2.1$ mm. The small discrepancy between prediction and measurement can be attributed to difficulties in the accurate measurement by visual methods of such small displacements, as well as to an uncertainty over the exact number of turns ($N_t$) in the coil.

The same experiment was repeated by using 4 stacked PM4 permanent magnetic rings (**Table 3.2**). Since the ring magnets have a permanent field, it was not possible to observe the same response as the FG movement induced by the electromagnet. The stacked PM4 magnets had a significantly larger magnetic field strength than the electromagnet. Slow and steady movement of the ring magnets alongside the tube induced substantial FG movement. The ferrofluid rose cohesively as a continuous column to a height of 0.06 m above the original FG-air interface in the half of the U-shaped tube along which the magnet moved upward. Further rise was limited by the tube dimensions. This rise was accompanied by a corresponding equal decrease in height on the opposite side of the tube. The FG movement continued until the gravity force exceeded the magnetic attraction, beyond which point the FG column broke apart and the bulk of the fluid fell back to an equilibrium position with FG levels at the same height in the two halves of the tube. A portion of the FG column remained trapped within the magnetic field and followed indefinitely the movement of the magnets in any direction.

To further investigate vertical ferrofluid movement, a droplet of ferrofluid with a volume $V_d = 0.2$ mL was placed on a horizontal glass plate, and was exposed to the magnetic fields of the PM3 and PM2 magnets. Discernible vertical deformation was observed when the air gap, $L_0$, was 0.05 and 0.08 m, respectively. The magnetic field created by the PM2 at $L_0$ was measured at $3 \times 10^{-3}$ T, which compares favorably to the predicted value of $5 \times 10^{-3}$ T from equation (3.29) when considering the sensitivity of the magnetic field to distance.

### 4.2.2. Horizontal FG Movement

Horizontal deformation of the FG was expected to occur at a greater distance because the ferrofluid would not have to overcome the gravitational field. Two experiments were conducted to determine the largest distance (air gap) from which horizontal FG movement

(initially manifested as deformation of a small FG quantity) could be induced by the permanent magnets. In the first experiment, a thin stream of ferrofluid falling through a small hole in the horizontal bottom of a small container was approached from the side by the permanent magnets. Visible deformation was observed at distances of 0.07 m and 0.115 m with the PM3 and PM2 magnets, respectively.

In the second experiment, drops of ferrofluid were placed on a carefully leveled, horizontal acrylic plate so that the drops formed a circular pool on the plate surface. Each FG drop had a $V_d = 1.3$ ml and a diameter of 0.015 m. The maximum air gap over which horizontal movement could be effected was observed. For the PM3 and PM2 magnets, the maximum air gaps were 0.08 and 0.12 m, respectively. The initially circular ferrofluid droplets were first deformed to an oblong shape, then slowly elongated until contacting the magnet (**Figure 4.1**). Following contact with the magnet, the ferrofluid continued to flow along the formed channel and collect on the magnet surface.

In all cases, the PM2 magnet effected FG deformation or movement from a greater distance than the PM3 magnet. This was expected because, although the two magnets have nearly identical $B_r$ and $H_c$ values, the dimensions of the PM2 magnet, i.e. the $L_m$, $a$ and $b$ of equations (3.28) through (3.31), are larger than those of the PM3 magnet. From these equations, it is obvious that a larger magnet (i.e. longer and/or with a larger pole surface area) will produce a stronger field $H$. Such an increase in $H$ can be effected by stacking the magnets.

The PM3 and PM2 magnets were stacked, resulting in a longer magnet but with an uneven pole surface area. With the stacked configuration, the maximum air gap was increased to 0.15 m. When 5 stacked PM1 magnets were used, the combined $L_m = 0.127$ m and the maximum airgap increased to 0.27 m.
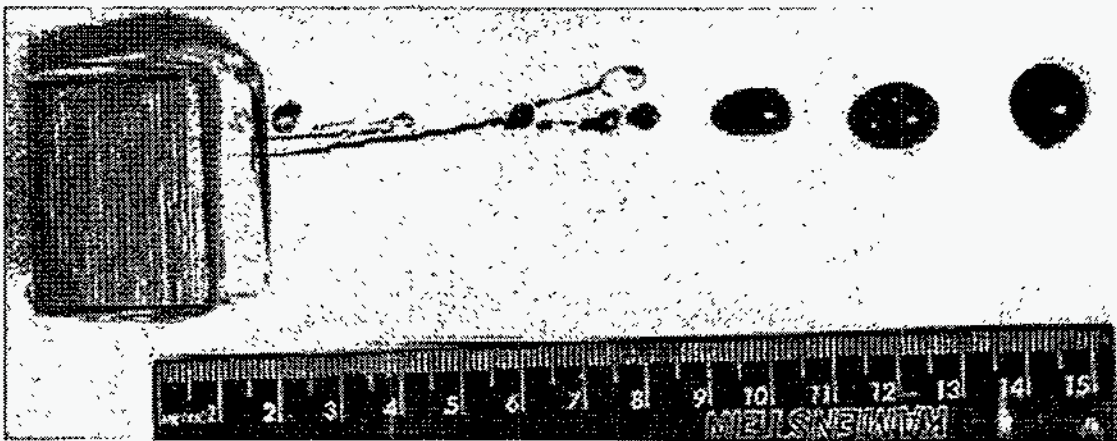


**Figure 4.1.** Movement of EMG 805$^{TM}$ ferrofluid under the influence of the PM2 magnet.

# 4.3. Experiment 2: Ferrofluid Movement in Hele-Shaw Cells

The use of Hele-Shaw cells, i.e. parallel glass plates with a narrow gap width, as experimental analogues for porous media is well documented [*Saffman and Taylor*, 1958]. The permeability $k$ of a Hele-Shaw cell is given as

$$k = \frac{1}{12}\, a^2 \qquad\qquad (4.2)$$

where $a$ is the gap width. In this experiment, ferrofluid was injected into a Hele-Shaw cell filled with water and the FG movement under the influence of a magnetic field was observed. Compared to two-dimensional (thin-plate) porous media systems, Hele-Shaw cells offer the advantage of clearer visualization of the flow.

Two Hele-Shaw cells were constructed from 0.25 m × 0.28 m smooth glass plates. A 1.6 mm shim was placed between the plates to achieve a fixed gap size. After the edges were sealed with silicone, the cells were filled with water and leveled horizontally. A small volume of EMG 805[TM] ferrofluid was injected using a thin syringe. Following the injection, the syringe was removed and an external magnetic field was applied using the 5 stacked PM1 magnets. The cell gap was aligned with the $x$ axis of the magnetic pole (**Figure 3.2**). In response to the magnetic field, the ferrofluid started moving towards the magnet.

A series of snapshots from a typical experiment is shown in **Figure 4.2**. Plate (a) shows the initial FG shape ($t = 0$) before the application of the external magnetic field. At $t = 219$ s from the application of the magnetic field, the fluid has moved slowly to form the teardrop shape shown in plate (b). As the teardrop elongates, the fluid closest to the magnet accelerates because it encounters higher magnetic field strength and higher field gradient. In plate (c) at $t = 277$ s, the fluid acceleration due to these strong forces is leading to turbulent instabilities which appear as fingers in the advancing FG front. In plate (d) at $t = 427$ s, the fluid has reached the sealed end of the Hele-Shaw cell and is accumulating symmetrically around the magnet. The fluid continues migrating until practically all accumulates against the magnet forming a symmetric, arc-shaped pool.

Note that, despite the complete water miscibility of EMG 805[TM], mixing with the water in the cell gap appears to be very limited, and is indicated by a lighter-gray halo around the FG pool. This is attributed to the strong attractive forces between the FG and the magnet. The FG particles are aligned with the magnetic field, free Brownian motion is inhibited and mixing is thus limited. Of particular interest is that the fluid, regardless of the pathway to the magnet, invariably accumulates in a symmetric, arc-shaped pool. This attribute has potentially important implications in environmental applications.
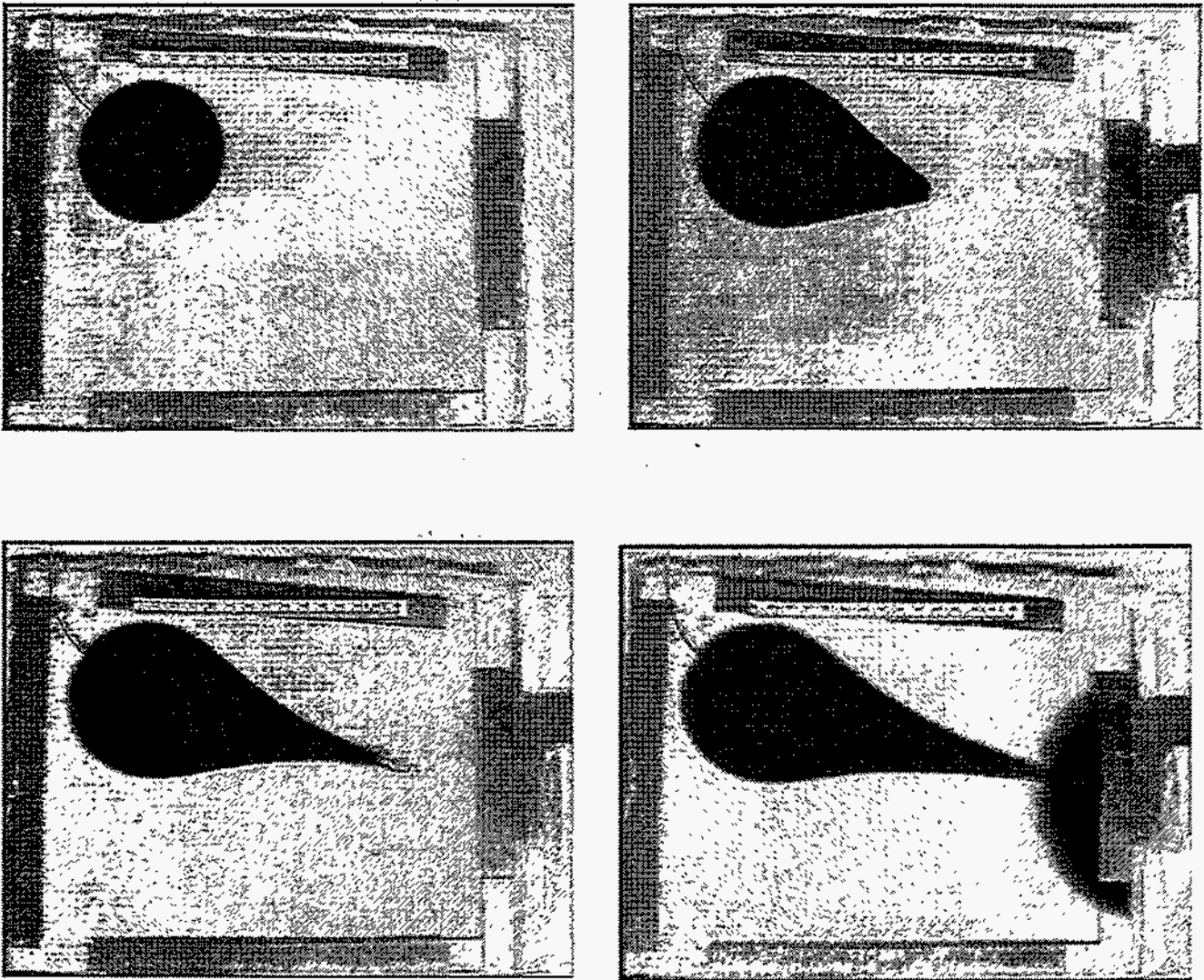
**Figure 4.2.** Movement of EMG 805$^{TM}$ ferrofluid in a water-filled horizontal Hele-Shaw cell with a gap width of 1.6 mm.

Water soluble dye was injected into the water in the cell gap to visualize the water recirculation pattern caused by the FG as it moved toward the magnet and displaced water. Close observation revealed a recirculating flow pattern defined by the advancing FG as it swept the dye away from the magnet, first along the edges of the plate along which the magnet was located, and then back toward the FG injection point.

# 4.4. Experiment 3: Ferrofluid Movement in a Porous Medium

The movement of ferrofluids through porous media was investigated in shallow beds of saturated Monterey #60 sand (hydraulic conductivity $K = 5 \times 10^{-4}$ m/s, $\phi = 0.46$) in trays with dimensions 0.1 m $\times$ 0.12 m. The thickness of the sand bed was 0.01 m. After saturating the sand-filled trays with water, the sand surface was smoothed and was left exposed to the air. EMG-C$^{TM}$ ferrofluid was injected at a distance of 0.1 m from one side of the tray. The initial FG distribution was approximately circular (**Figure 4.3**) or band-shaped (**Figure 4.4**). Aligning the centerlines of the sand tray and of the 5 PM1 magnets, an external field was then applied. The FG movement through the sand was recorded using a video camera, which was activated and time indexed at appropriate intervals.

Typical results of a sand bed experiment with an initial circular FG distribution are shown in **Figure 4.3**. The flow of fluid toward the magnet is very similar to that observed in the Hele-Shaw experiment. The ferrofluid initially follows a direct pathway toward the center of the magnet. Upon reaching the wall next to the magnet, the FG begins to accumulate and form an arc-shaped pool around the magnet.

Practically identical observations are made when using a larger sand tray (0.1 m $\times$ 0.3 m) and a larger initial distance from the magnet (**Figure 4.5**). These experiments demonstrated ferrofluid movement from distances of 0.22 m with the 5 stacked PM1 magnets. The initial FG velocity is very low. To cover the distance of 0.22 m through the saturated sand to the magnet takes about 1 week, with the process of deformation of the initial disk to a tear drop shape taking the majority of this time. As the fluid approaches the magnet, the velocity increases due to the increasing magnetic field strength and gradient.

The movement of ferrofluid from the initial band to the magnet is shown in **Figure 4.4**. In general, several fingers of fluid (in all likelihood, corresponding to the highest permeability pathways) break from the band and move toward the magnet. Once a continuous path is established, accumulation of the fluid begins and the final FG distribution is very similar to that in the experiment with the circular FG distribution. The difference in the size of the final FG pool in the two experiments is due to the larger amount of FG in the band.

t=0 min            t=10 min

t=16 min          t=38 min

t=48 min          t=93 min
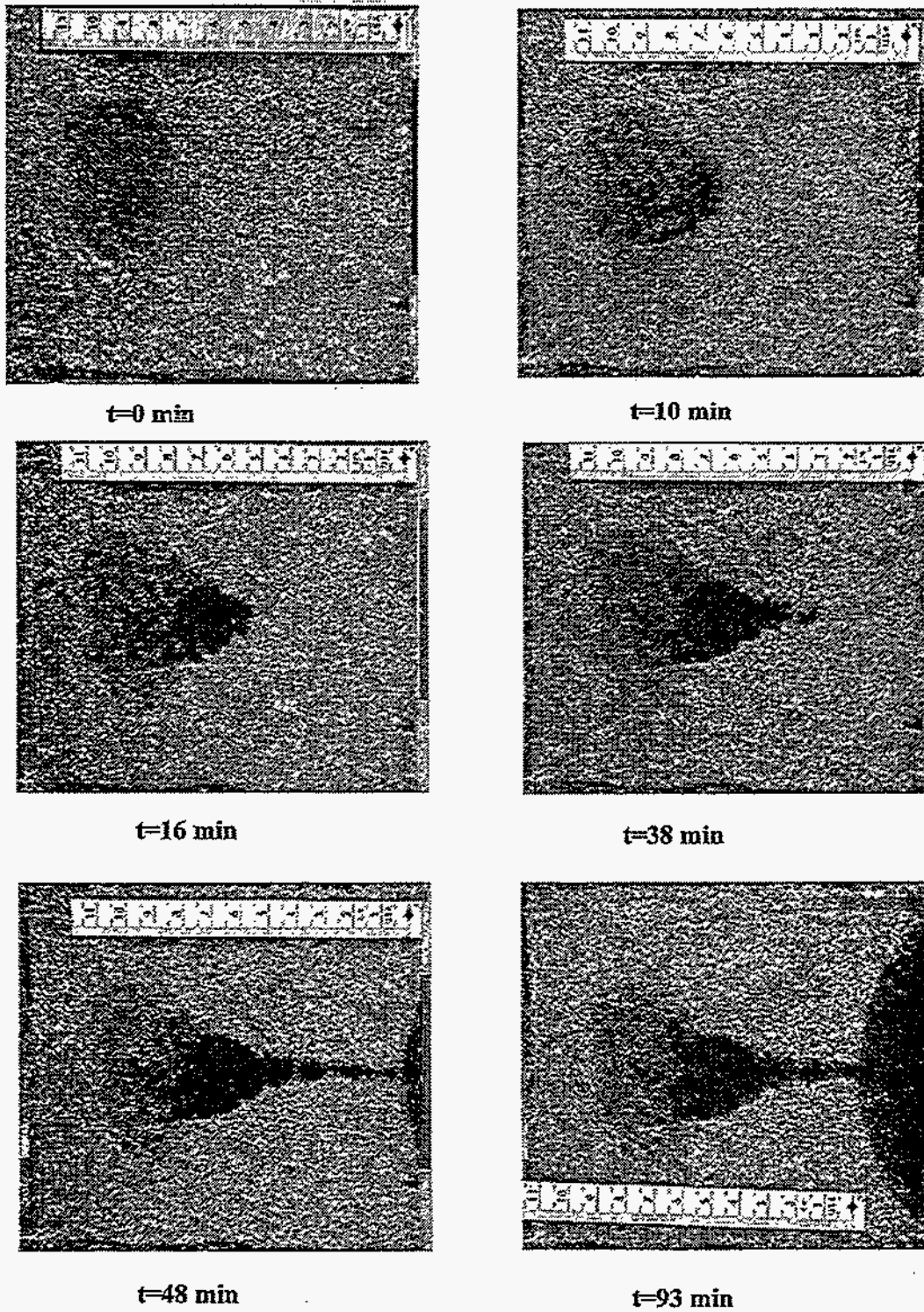
**Figure 4.3.** Movement of EMG-C$^{TM}$ through sand from an initial circular FG distribution.

t=0 min

t=11 min

t=114 min

t=166 min

t=172 min
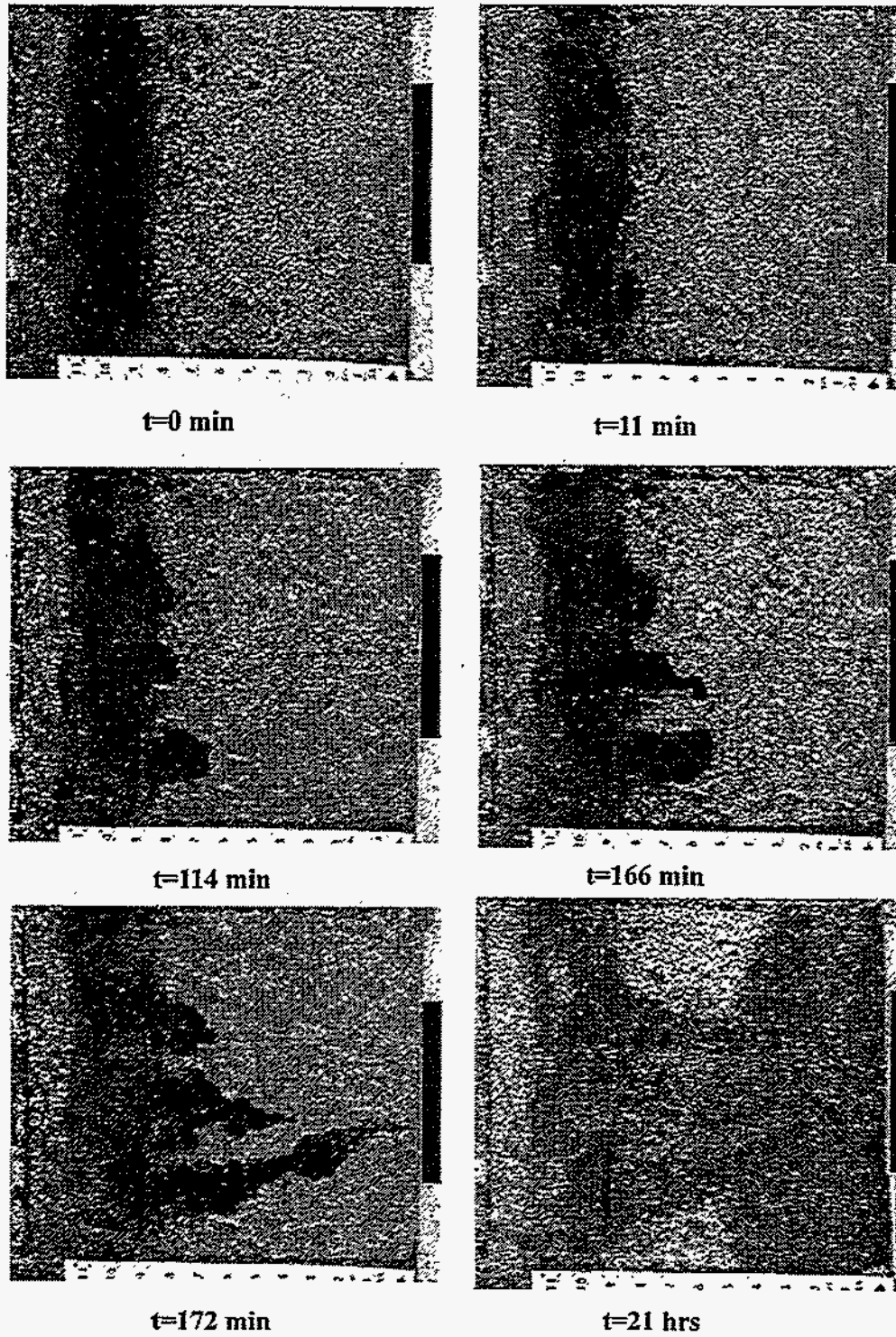
t=21 hrs

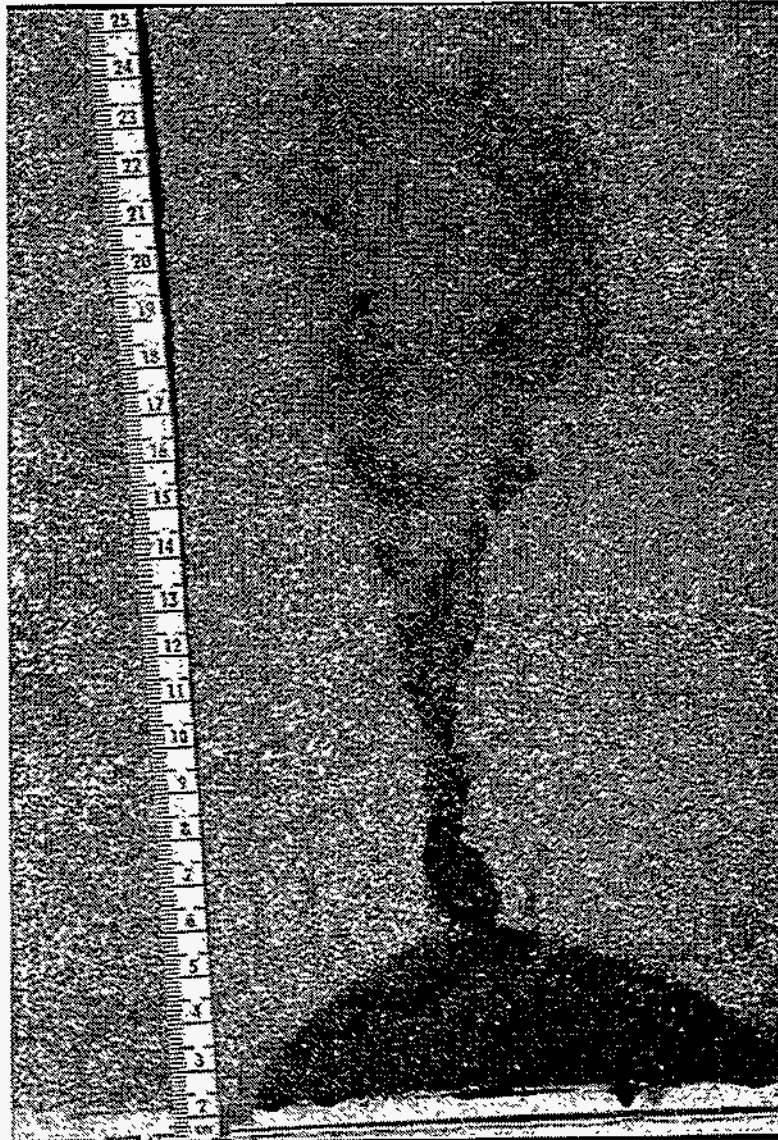**Figure 4.4.** Movement of EMG-C$^{TM}$ through sand from an initial band-shaped FG distribution.

**Figure 4.5.** Final distribution of EMG-C$^{TM}$ in a longer sand tray.

The importance of the observations in **Figures 4.3** through **4.5** lies in the realization that despite differently-shaped initial FG distributions, varying initial distance from the magnets, heterogeneous permeability fields, and FG flow along preferential pathways, the final FG distribution is invariably predictable, symmetric and is controlled by the magnetic field. In other words, the final FG distribution is unaffected by heterogeneities in the properties of the porous media and flow patterns, although the transient approach to the final distribution may be affected by medium heterogeneities. The implication of this realization is that FGs with appropriate reagent-laden carrier liquids could be accurately guided to and positioned in contaminated target zones in the subsurface.

Investigation of the vertical FG distribution in the sand tray at the conclusion of the experiments revealed a uniform coverage throughout the depth of the sand layer. In all cases, the trail of ferrofluid could be readily seen by the residual black FG coating left on the sand particles.

## 4.5. Experiment 4: Magnetopressure

Magnetopressure is defined as the pressure exerted by a ferrofluid in response to a magnetic field. The apparatus used for magnetopressure measurements consisted of a horizontal column of ferrofluid connected at one end to a differential pressure transducer (DPT) and open to the atmosphere on the other (**Figure 4.6**). To avoid magnetic effects on its metallic parts, the DPT was connected to the column by means of a tube filled with silicone oil (Dow Corning Corp., Midland, MI), which served as a pressure-transfer liquid.

The FG column in this experiment was 0.12 m long, with an OD of 6.35 mm and a 1.6 mm wall thickness. The flexible nylon connector tube (for the pressure transfer to the DPTs) was 1.3 m long, with an OD of 3.18 mm. This length was sufficient to eliminate any possible effects of the magnetic field on the DPT. To cover the range of the magnetopressures measured in this experimental series, three different transducers were used, i.e. Validyne DPT models DP 15-30, DP 15-26, and DP 15-20 (Validyne Systems, Northridge, CA). The transducers were calibrated using the known hydrostatic pressures in a vertical water column. The DPT measurements were recorded on a personal computer using a Validyne signal conditioning unit operated by a GPIB interface with a LabVIEW$^{TM}$ (Austin, TX) data acquisition program.

Pressure measurements were taken as the permanent magnets approached the end of the column connected to the pressure transducer. The PM2 and the 5 stacked PM1 magnets (**Table 3.2**) were used in this experiment, in which the centers of the FG column and of the magnetic pole face were aligned. **Figures 4.7** and **4.8** show the measured magnetopressures $p_G$ (gauge pressures over the atmospheric) in horizontal columns filled with the EMG-C and EMG 805$^{TM}$ ferrofluids, respectively.

Magnetopressure Experiments
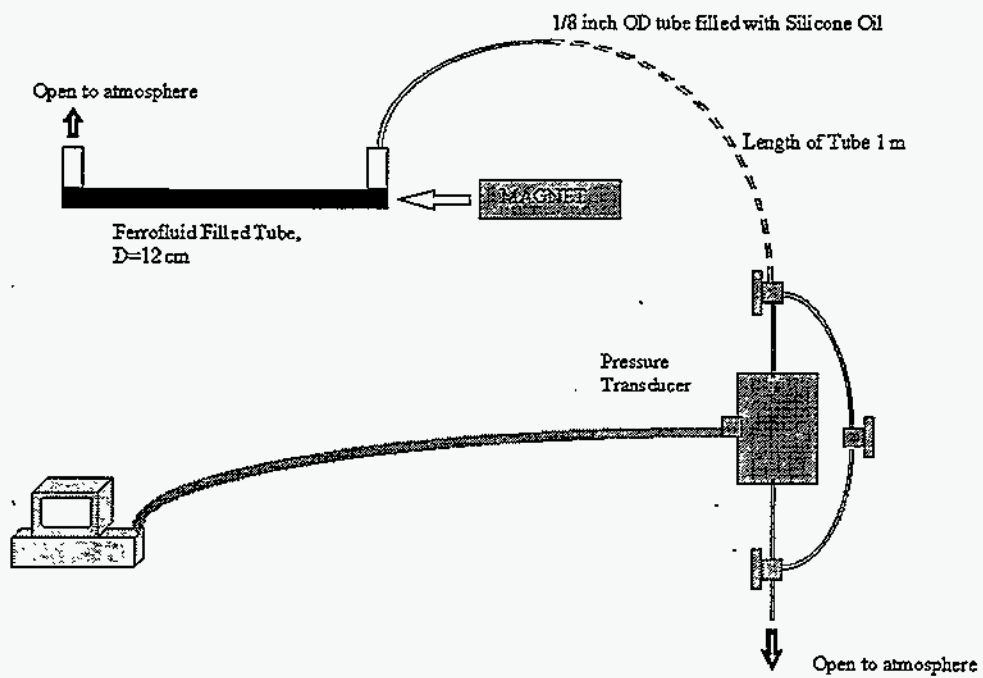


**Figure 4.6.** Schematic of the magnetopressure experiments.
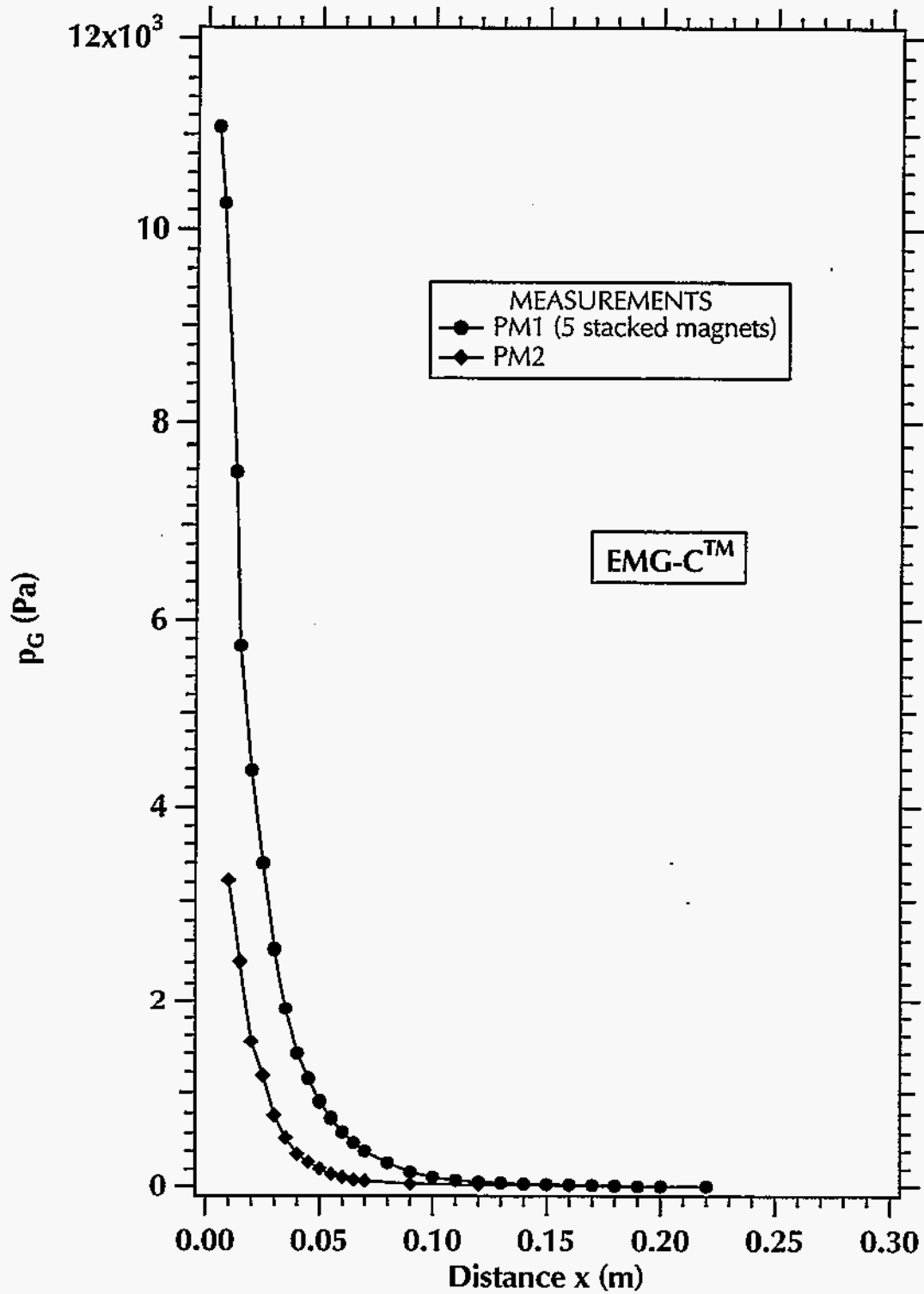
**Figure 4.7.** Magnetopressure (gauge) measurements using the EMG-C™ ferrofluid.
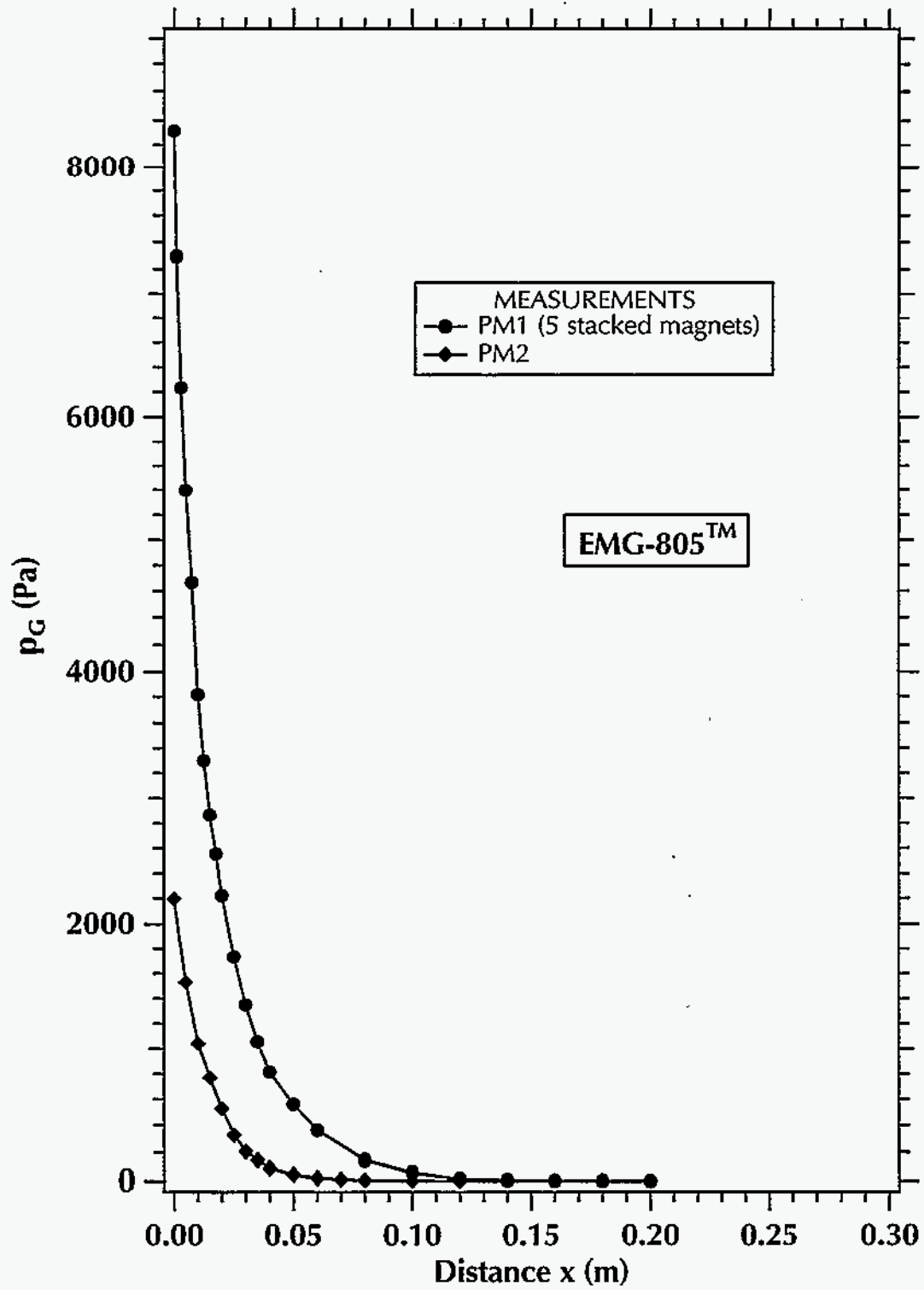
**Figure 4.8.** Magnetopressure (gauge) measurements using the EMG 805$^{TM}$ ferrofluid.

The magnitude of the magnetopressures $p_G$ and the distance over which they are measurable increase with the saturation magnetization of the ferrofluid (EMG-C *vs*. EMG 805[TM]) and the strength of the magnetic field. Note that the close-range measurements in **Figures 4.7** and **4.8** may not be very reliable because the strong attraction between the ferrofluids and the magnets at such short distances did not allow accurate magnet positioning.

# 5. NUMERICAL SIMULATION OF FG FLOW

## 5.1. General Principles

In this section we discuss the development of numerical simulation capabilities for modeling the flow of ferrofluid in porous media. These simulation capabilities are being added to the multicomponent flow and transport simulator TOUGH2 [*Pruess*, 1987; *Pruess*, 1991*a*] in the form a new equation of state (EOS) module called EOS7M. Because the framework for porous media flow and component mass conservation are already established in TOUGH2, the essence of this task lies in the calculation of the external magnetic field and the body force due to ferrofluid magnetization in the spatially varying external magnetic field.

The attractive force on a volume of ferrofluid due to magnetization $M$ by an external magnetic field $H$ is given by the expression [*Rosenzweig*, 1985]

$$\vec{F} = \mu_m M \nabla H \tag{5.1}$$

where $\mu_m$ is the magnetic permeability in Tesla·m/Ampere-turn (Tm/A), $M$ is the magnetization in A/m, and $H$ is the magnetic field strength in A/m. To calculate ferrofluid flow, it is necessary to (i) calculate the ferrofluid magnetization, (ii) calculate the external magnetic field and its gradient, and (iii) calculate of physical properties of ferrofluid-water mixtures such as density and viscosity. This additional force and the mixing model calculations are inserted into TOUGH2 to create the ferrofluid flow and transport simulation capability. A brief discussion of these steps along with summaries of preliminary validation results are

presented in this section.

## 5.2. FG Magnetization

Magnetization is the result of ferrofluid becoming polarized in the presence of an external magnetic field. As the magnetic field strength increases from an initial level of zero, the ferrofluid becomes magnetized to a degree controlled by the strength of the external field and the magnetic susceptibility of the ferrofluid. The relationship between the magnetic induction $B$, also called the magnetic flux density, $H$, and $M$ is known generally as the $B - H$ curve, where

$$\vec{B} = \mu_m(\vec{H} + \vec{M}). \tag{5.2}$$

Note that equation (5.2) is written in terms of the vectors $\vec{B}$, $\vec{H}$, and $\vec{M}$, but can also be written as a scalar equation where $B$, $H$, and $M$ are scalars representing vector magnitudes. As the magnetic field strength is increased beyond some point, the ferrofluid reaches a maximum magnetization, or saturation magnetization. Thus the magnetization is a function of $H$ whose parameters depend on the particular type of ferromagnetic material:

$$\vec{M} = f(\vec{H}). \tag{5.3}$$

Ferrofluid magnetization data along with two fitted curves are shown in **Figure 5.1** as $M$ plotted against $H$. The full $B$-$H$ curve for the ferrofluid would be obtained by multiplying $M$ by $\mu_m$ and adding the $\mu_m H$ term of equation (5.2). **Figure 5.1** is indicative of a *soft* magnetic material, that is one that attains magnetization easily and reaches saturation at relatively low magnetic field strength. The two key magnetic parameters describing magnetization are the initial susceptibility and the saturation magnetization. Given the magnetic properties of the medium and of the FG, all that is necessary to calculate the force on a ferrofluid due to an external magnetic field is the strength and direction of the external magnetic field and its gradient at all points where FG is present.

Magnetization curves can be fit using various curves. **Figure 5.1** shows the goodness-of-fit of the double exponential function

$$M = 15689.1 - 8060.1 \exp(7.5274 \times 10^{-6} H) - 7409.1 \exp(8.0736 \times 10^{-5} H),$$

and of the arctangent function

$$M = 10^4 \operatorname{atan}(3 \times 10^{-5} H).$$

The arctan approximation was used in the EOS7M module discussed in this Section.
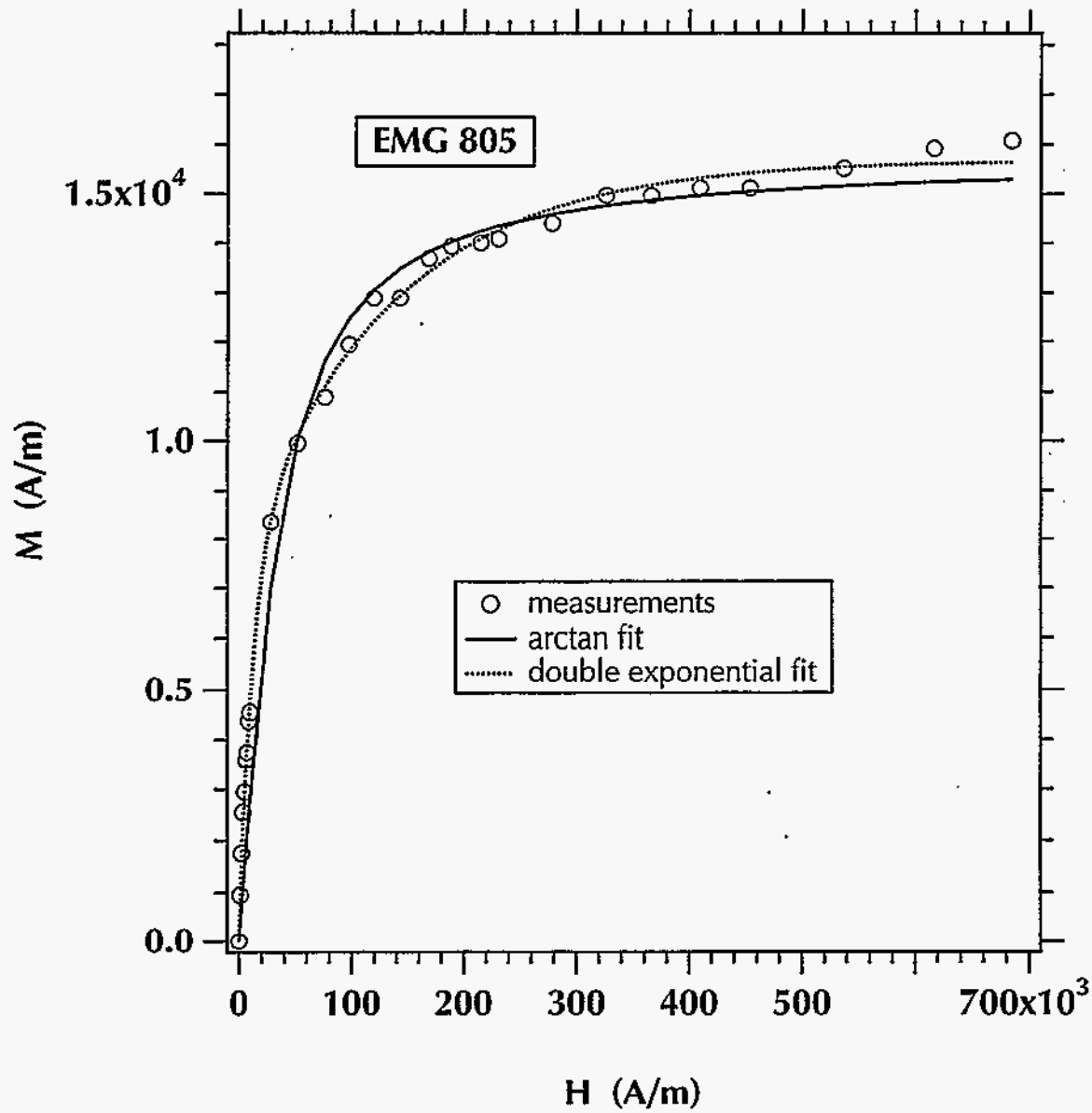
**Figure 5.1.** Ferrofluid magnetization data and fitting curves used to model the magnetization of the EMG 805™ ferrofluid.

# 5.3. External Magnetic Field

The calculation of the external magnetic field is complicated for general systems where magnetic permeability varies in the domain. However, in situations where the medium is of uniform magnetic permeability and permanent magnets or electromagnets are the source of the magnetic field, we can use some simple equations to calculate the components of $H$ directly [*McCaig and Clegg*, 1987]. The equations of the magnetic field as functions of the geometry and properties of a permanent magnet were given in Section 3. Once the magnetic field strength is known at each point, simple differencing is used to calculate the gradient of the field. Note that it is only necessary to calculate $H$ and its gradient at positions in the flow domain that contain ferrofluid.

Although $B$ is altered by the presence of ferrofluid, $H$ is independent of the presence of ferrofluid. Thus the procedure we implement in EOS7M involves calculating the magnetic field strength only once at the beginning of each simulation. The coupling between ferrofluid flow and magnetic field occurs through the $M$ and $H$ terms. Once $H$ and its gradient are calculated, we calculate magnetization using a best-fit function to the magnetization curve. Then the magnetic force at the interface between each gridblock is calculated and added to the pressure gradient and gravitational body force terms.

# 5.4. Numerical Treatment of the FG Properties

The EOS7M module under development is based on the EOS7 thermophysical properties module for water, brine, and air [*Pruess*, 1991b]. As such, there is already the facility to handle brine-water mixtures in terms of density and viscosity variations. We use these same facilities to model the density and viscosity of water-FG mixtures in water-based ferrofluids.

The mixing model for aqueous phase density assumes two pseudo-components, an end member ferrofluid with mass fraction $X_f$, and pure water with mass fraction $X_w = 1 - X_f$. The FG component is assumed to consist of $H_2O$, magnetite particles, and surfactant. Following the work of *Reeves et al.* [1986] and *Herbert et al.* [1988] on brine-water mixtures, we assume the volumes of pure water and ferrofluid are additive, and obtain for the mixture density $\rho$ the equation

$$\frac{1}{\rho} = \frac{1 - X_f}{\rho_w} + \frac{X_f}{\rho_f} \tag{5.4}$$

where the density of each component is given by $\rho_w$ and $\rho_f$. At such time when density effects become important in our applications, laboratory experiments will be carried out to test this mixing model, and alternate models will be incorporated in EOS7M as appropriate.

Viscosity effects are incorporated through the correlation of *Herbert et al.* [1988]

$$f(X_f) = 1 + \mu_1 X_f + \mu_2 X_f^2 + \mu_3 X_f^3. \tag{5.5}$$

The viscosity of the brine is calculated by multiplying $f(X_f)$ by the viscosity of pure water at the given pressure and temperature. The viscosity of pure ferrofluid (EMG-805) is 2.35 times as large as the viscosity of pure water at 20 °C, corresponding to $\mu_1 = 1.35$. We currently set $\mu_2 = \mu_3 = 0$ due to lack of data.

# 5.5. Validation and Testing

In a preliminary validation of EOS7M, **Figure 5.2** presents results of a test of direct measurement of magnetic field strength compared to calculations using EOS7M. The experiment consists simply of the measurement of magnetic induction with a digital Gaussmeter (F.W. Bell, Boca Raton, FL, Model 811A, with a HTJ4-0608 probe) at various distances from the PM1 magnet (**Table 3.2**).

The measurements are converted to $H$ units and are shown in **Figure 5.2** along with calculated values of $H$ in a direction aligned with the poles. The Gaussmeter measurements are based on magnetic flux through a very small crystal sensing device at the tip of the probe, and are very sensitive to position and probe angle when the probe is near the magnet. Thus the data point at $z=0$ is not considered as reliable as the points farther from the magnet. These results demonstrate the validity of the *McCaig and Clegg* [1987] equations in EOS7M.

An additional validation experiment was conducted to test the calculation of forces on the ferrofluid in EOS7M. This experiment, in which the PM1 magnet is moved toward a small horizontal tube containing pure EMG 805TM ferrofluid that is open to atmospheric pressure on one end and connected to a pressure transducer on the other end, is discussed in Section 4.5. The tube is aligned with the magnetic poles. The magnet is moved toward the tube along the axis of the poles while the pressure at the end of the tube is recorded. This results in a plot of pressure *vs.* distance, where the pressure $p_G$ is due to the force on the ferrofluid.

Shown in **Figure 5.3** is the comparison between calculated pressures (obtained when using the arctan fitting curve shown in **Figure 5.1**) and measured pressures. A very good agreement between the two is observed.
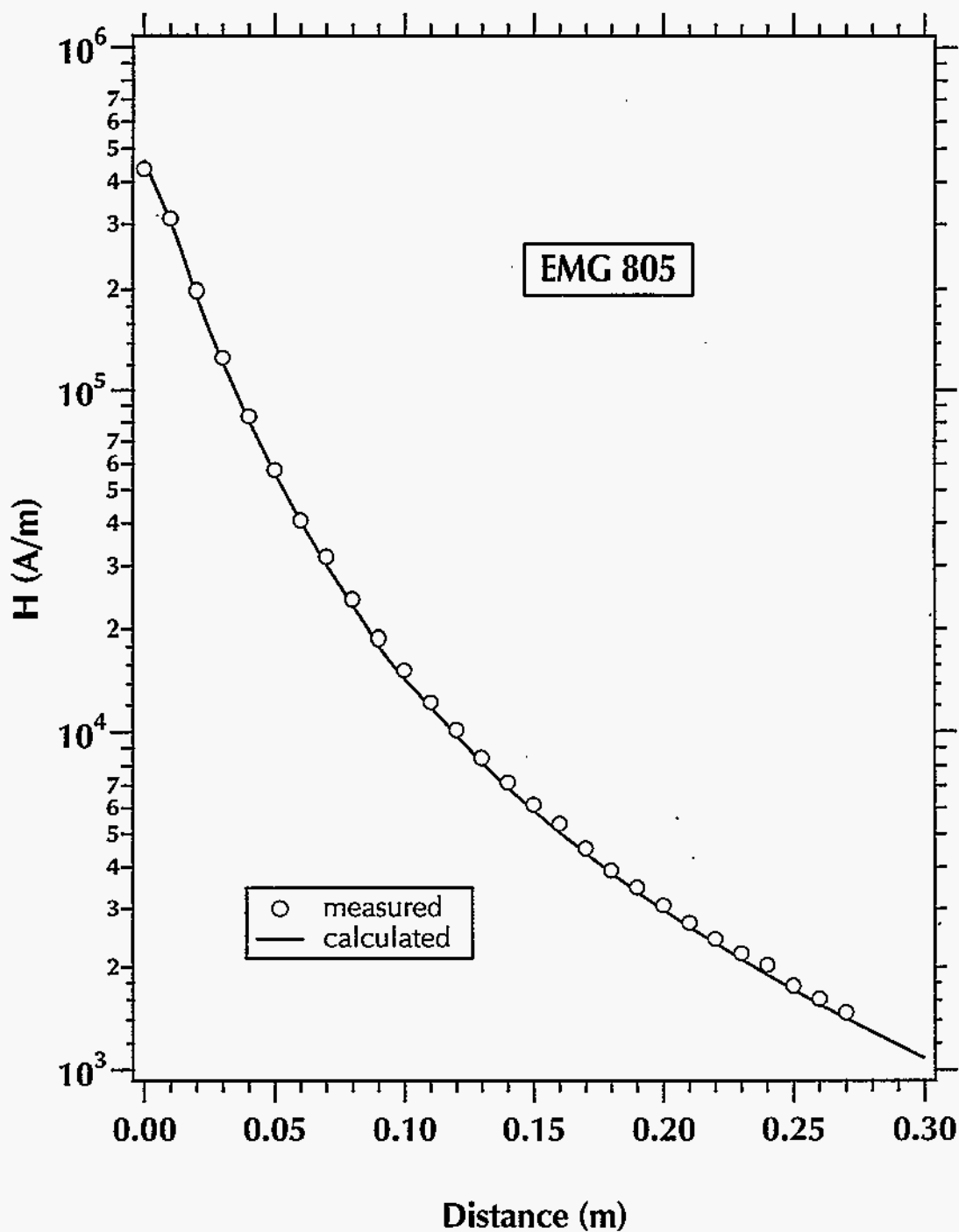
**Figure 5.2.** Calculated and measured values of magnetic field strength versus distance away from the permanent magnet PM1.
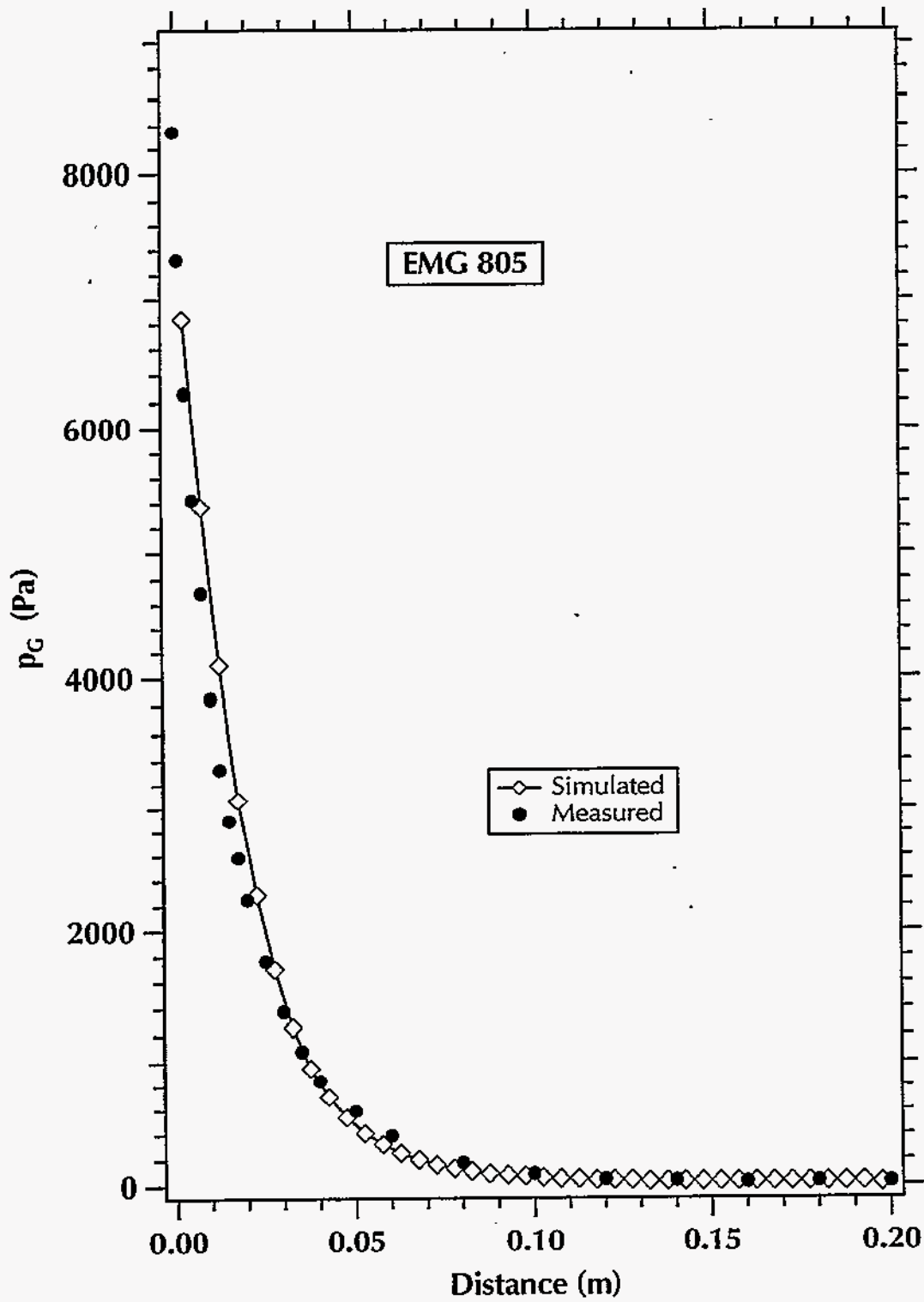
**Figure 5.3.** Measured and calculated ferrofluid pressures (gauge) *vs.* distance from the permanent magnet PM1.

# 6. GEOPHYSICAL STUDIES OF FT PERFORMANCE

## 6.1. Magnetic Detection of FTs

The investigation of the use of ferrofluids as imageable tracers (FTs) is discussed in this section. Tracers are frequently used for characterization of subsurface hydrological properties. Broadly, the method involves the injection of a specific quantity of the tracer fluid through an injection well and monitoring the rate and extent of movement of the fluid by sampling in one or more monitoring wells. One of the drawbacks of this method is that it is invasive in nature, so that the very process of monitoring may disturb the system under study. The use of tracers with magnetic properties can remove this drawback if the injected fluid can be imaged non-invasively by observing the associated magnetic field anomaly at this surface.

The detection of magnetized material in the subsurface is well established in the methodology of applied geophysics [*Telford et al.*, 1990]. One of the earliest magnetic surveys, conducted nearly 100 years ago, was aimed at confirming the outline of the Kiruna iron formation in Sweden. This practice, commonly referred to as the magnetic mapping method, is based on very precise measurements (an accuracy of 20 ppm or $\pm 1$ nT can be achieved routinely) of the earths magnetic field which, on a local scale, is relatively invariant. Thus even very small local variations of the earths field can be associated with the presence of subsurface magnetic material.

The limiting parameter in the detection of the ferrofluid in the subsurface is the susceptibility of the magnetite. The susceptibility is determined both by the magnetic material and by particle size. The susceptibility is a linear function of dilution, and detection

depths can be evaluated on a per case basis. In order to assess the feasibility of using dilute ferrofluid as a tracer, we investigate the depth to which a volume containing 1 m$^3$ of a 15% solution of EMG 805$^{TM}$ water-based ferrofluid (**Table 3.1**) injected into a medium of $\phi = 0.3$ can be located. For this study we consider 3.3 m$^3$ of magnetizable material either in the form of a sphere (with a radius $r = 0.92$ m) or in the form of a circular thin plate (with a thickness $d = 0.02$ or $d = 0.10$ m, corresponding to plate radii of $r = 7.75$ m and 3.25 m, respectively). In addition, we discuss the detection of a thin square slab (with $d = 0.02$ m and 0.10 m) and of a vertical semi-infinite cylinder of varying $r$.

# 6.2. Theoretical FT Studies

## 6.2.1. Magnetization

In computing the magnetic anomalies in this study, we assume that the induced magnetization is directly proportional to the inducing field (local ambient magnetic field) and the magnetic susceptibility of the material. We also assume that this quantity is a linear function of the ferrofluid dilution. The magnetite in the EMG 805 ferrofluid has an initial magnetic susceptibility $k_m = 6.16$ MKS units. The concentration of magnetite in the EMG 805 fluid is 3.7%, which would give the ferrofluid a susceptibility of 0.23 MKS. When injected into soil with $\phi = 0.4$, the resulting soil-liquid system has a magnetic susceptibility of 0.091 MKS units at full saturation (i.e., when undiluted). At the postulated 15 % dilution, the corresponding susceptibility $k_m = 0.014$ MKS.

In these calculations we neglect demagnetization. This effect, which is a function of model geometry, tends to weaken the observable effects but is only noticeable in highly magnetized materials. For our spherical model and at the given susceptibility, the demagnetization effect is about 1%. Under these conditions the magnetization of a given object is simply the product of its susceptibility $k_m$ and the intensity of the ambient magnetic field $F_0$.

## 6.2.2. Anomalous Magnetic Field for a Sphere

The magnetic field anomaly for a magnetized sphere can be readily computed by considering it to be a magnetic dipole whose moment $M$ is simply the product of the spherical volume $V$ and its magnetization [*Telford et al.*, 1990]. The dipole axis is oriented along the direction of the inducing field. Thus we have,

$$M = V\, k_m\, F_0. \tag{6.1}$$

For the purpose of the model calculations, we consider a simple, high latitude, situation

where the sphere is exposed to a vertical inducing field of 47, 000 nT. The field is to be located using a total field magnetometer, which measures the vertical component of the anomalous magnetic field generated by the presence of the sphere. If the origin of the coordinate system is the center of the sphere (which is located at a depth $h$ below the surface), the observable magnetic anomaly along a traverse over the sphere center is then given by

$$\Delta F = \frac{M}{4 \pi r_d^3} \frac{2 h^2 - x^2}{r_d^2}, \tag{6.2}$$

where

$$r_d^2 = h^2 + x^2. \tag{6.3}$$

Numerical results for traverse profiles over three spheres of different depths but equal magnetic moment are shown in **Figure 6.1**. From equation (6.1), we note that the magnetic anomaly zero crossings are located at $x = \pm\sqrt{2h}$.

The anomaly maximum lies directly over the center of the sphere ($x = 0$) and has an amplitude of

$$\Delta F_{max} = \frac{M}{2 \pi h^3}. \tag{6.4}$$

For the model under consideration $M = 2.2 \times 10^4$ MKS. Assuming that 1 nT is the smallest detectable $\Delta F$ anomaly, then the maximal depth to center at which the 3.3 m$^3$ sphere can be detected is $h_{max} = 7$ m (**Figure 6.2**). Note that the maximum depth of detection varies as the $M^{1/3}$ of the sphere. This indicates that doubling the sphere radius doubles the depth of detection at constant saturation and ferrofluid susceptibility. On the other hand, for a constant sphere volume, the fluid susceptibility would have to be raised by a factor of eight (i.e., injection at full strength) in order to achieve a doubling in the depth of detection.

### 6.2.3. Anomalous Magnetic Field for a Flat Circular Plate

Considering a vertical inducing field and total field measurements, the maximal magnetic anomaly a flat thin circular plate with a radius $r$ occurs over its center and is given by

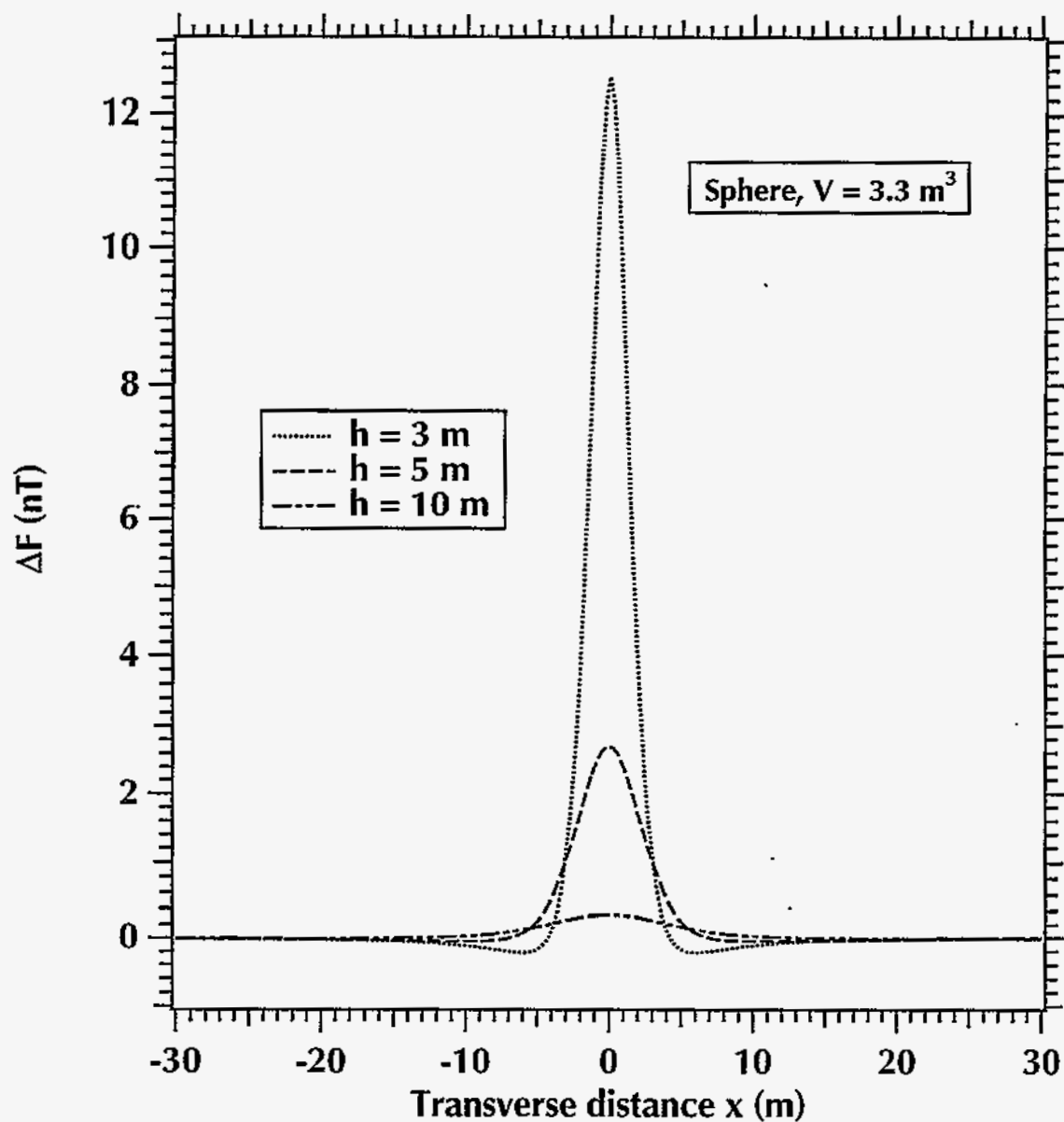$$\Delta F_{max} = \frac{M}{2 \pi (z^2 + r^2)^{3/2}}, \tag{6.5}$$

**Figure 6.1.** $\Delta F(r, x, h)$ for a $V = 3.3$ m$^3$ sphere along the $x$-axis (transverse) at depths $h = 3, 5$ and 10 m.
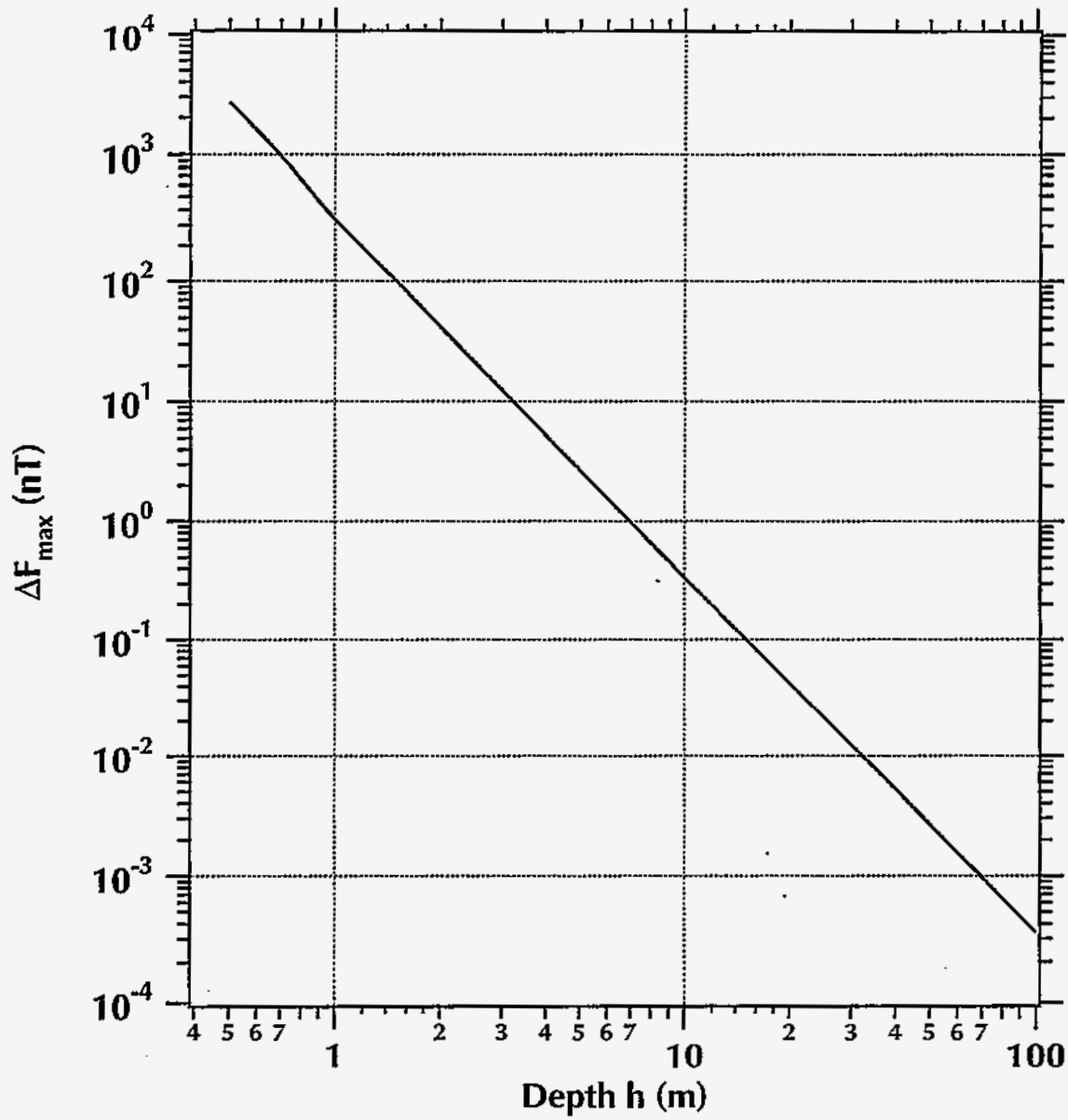
**Figure 6.2.** Dependence of $\Delta F_{max} = \Delta F(r, x = 0, h)$ on the depth $h$ to a $V = 3.3$ m$^3$ spherical anomaly.

where $z$ is the depth to the disk, and $M$ is given by equation (6.1). **Figure 6.3** shows the $\Delta F_{max}$ of a disk with a $V = 3.3$ m$^3$ and thickness $d = 0.1$ m and 0.02 m. At $z > r$, the anomaly due to the plate approaches that of a dipole.

If we take the disc and sphere volume to be equal, we can determine a relationship between $h_{max}$ (see section 6.2.1) and the maximal depth of detection for the disc, $z_{max}$. The two are related as

$$h_{max} = \sqrt{z_{max}^2 + r^2} \qquad \text{and} \qquad z_{max} = \sqrt{h_{max}^2 - r^2}, \qquad (6.6)$$

indicating that for an equal volume of material $z_{max} > h_{max}$. In the present case (in which $V = 3.3$ m$^3$), the $d = 0.02$ m plate ($r = 7.25$ m) can be detected to a depth of $z_{max} = 7$ m, i.e., at nearly the same depth as the sphere but 0.9 m lower than the sphere top. When $d = 0.1$ m, the disk $r$ decreases to 3.25 m, the magnetic anomaly over its center increases and $z_{max}$ increases to about 10 m. As before, demagnetization is neglected in these calculations. Note that when $r > z$, the magnetic field anomaly generated by the disk at its edges may exceed that observed over its center.

## 6.2.4. Anomalous Magnetic Field for a Flat Rectangular Plate

For a flat square plate at depth $h$, with width $2a$, length $2b$ and thickness $d$, the magnetic anomaly is given by the equation [Bhattacharyya, 1964]

$$\Delta F = \frac{k_m F_0 \, d}{4\pi} \left[ \frac{2\,b\,a_2}{(a_2^2 + h^2)\sqrt{a_2^2 + b^2 + h^2}} \left( 1 + \frac{h^2 + a_2^2}{h^2 + b^2} \right) \right.$$
$$\left. - \frac{2\,b\,a_1}{(a_1^2 + h^2)\sqrt{a_1^2 + b^2 + h^2}} \left( 1 + \frac{h^2 + a_1^2}{h^2 + b^2} \right) \right], \qquad (6.7)$$

where

$$a_1 = x - a \qquad \text{and} \qquad a_2 = x + a, \qquad (6.8)$$

and $x$ is the detector position on the surface with respect to the center of the plate. The transverse profiles of rectangular plate with a $V = 3.3$ m$^3$, $d = 0.02$ m and 0.10 m at $h = 0.5, 1,5,$ and 10 m are given in **Figure 6.4**. As with the thin disk, when $h \ll 2a$, the edges of the plate display a higher anomalous reading that the center. The maximum anomaly does not occur at the center of the plate (i.e., at $x = y = 0$) but near the edge of the plate.

The anomaly $\Delta F$ at the center ($x = 0$) of a square plate ($a = b$) is given by the equation
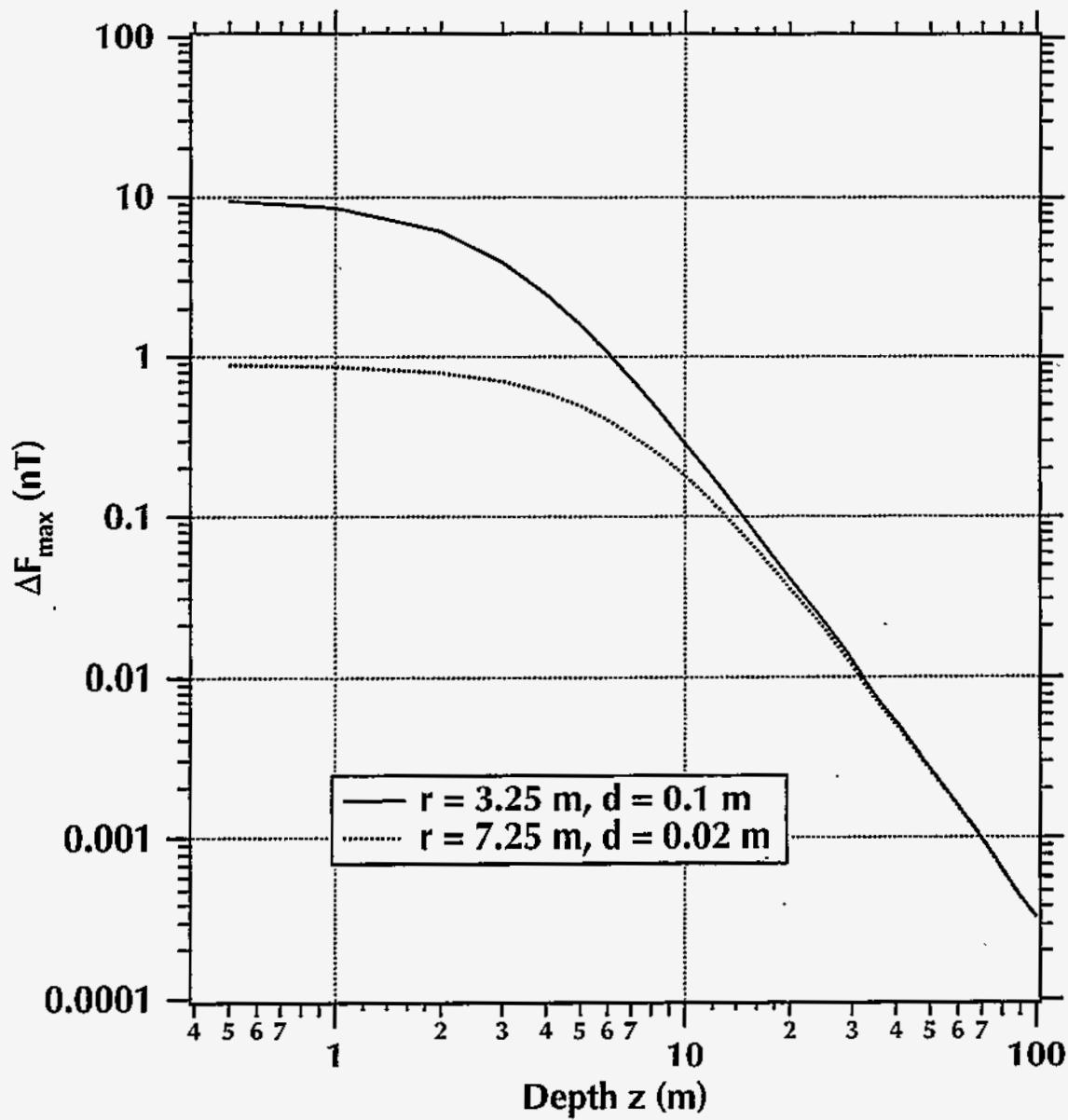
**Figure 6.3.** Dependence of $\Delta F(r, d, x = 0, h)$ on the depth $h$ to a $V = 3.3 \ m^3$ disk-shaped anomaly of thickness $d$ and radius $r$.
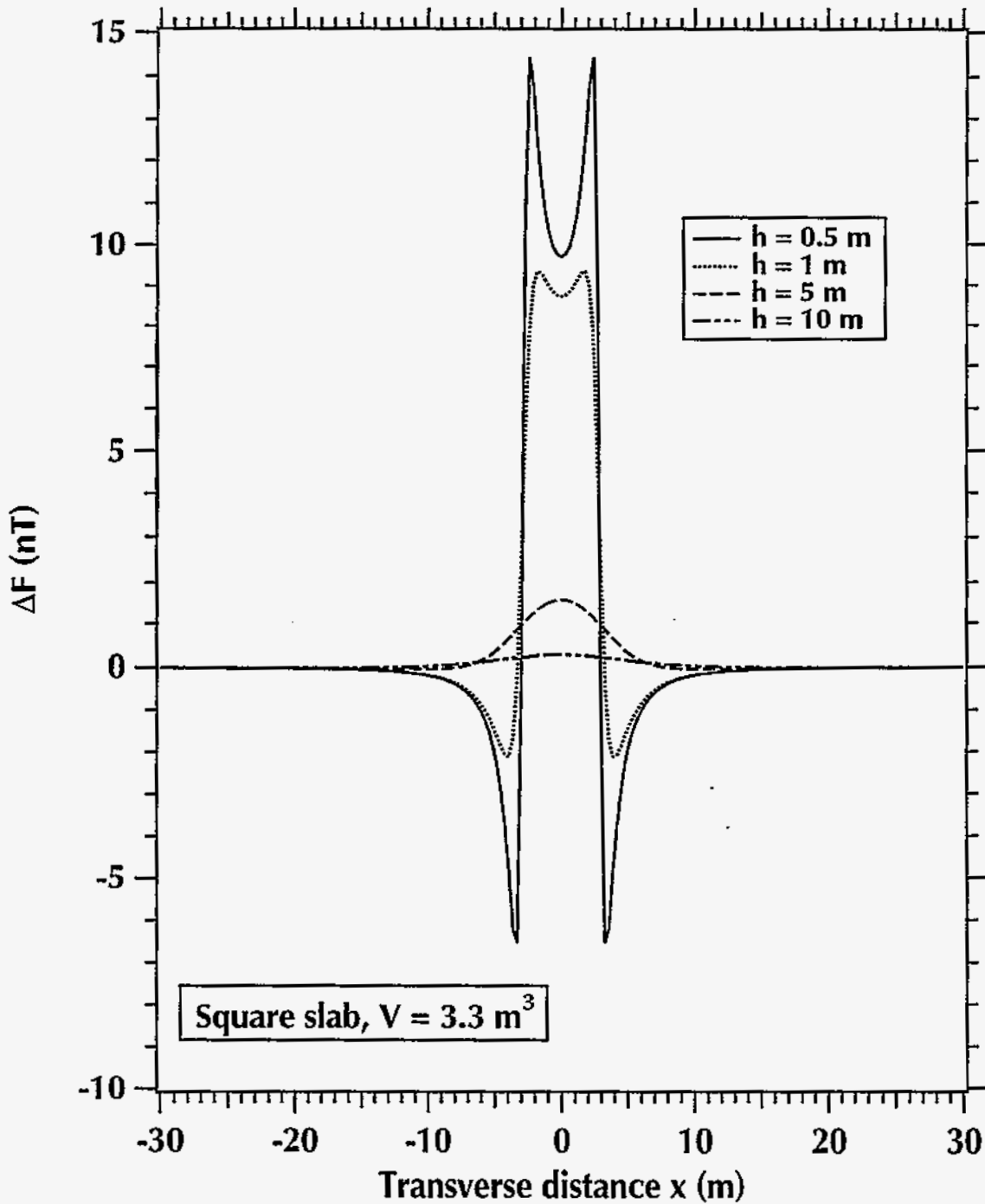
**Figure 6.4.** $\Delta F(a, d, x, h)$ for a $V = 3.3 \text{ m}^3$ square slab anomaly (of width $a$ and thickness $d$) along the $x$-axis (transverse) at various depths $h$.

$$\Delta F = \frac{k_m F_0 d}{\pi} \left[ \frac{a^2}{(a^2 + h^2)\sqrt{2a^2 + h^2}} \right]. \tag{6.9}$$

The $\Delta F(x = 0, h)$ for a square slab of thickness $d = 0.02$ and $0.10$ m are shown in **Figure 6.5**. The results are similar to those of the disk, with the anomaly approaching that of a dipole as $h$ increases.

### 6.2.5. Anomalous Magnetic Field for an Infinite Vertical Cylinder

A vertical cylinder at a depth to its top $z$ much less than its length can be approximated by a monopole, in which case the anomaly is given by [*Breiner*, 1973]

$$\Delta F = \frac{k_m F_0 r^2}{4 r_d^2}, \qquad r_d^2 = x^2 + z^2 \tag{6.10}$$

where $r$ is the cylinder radius and $x$ is the distance from the projection of the cylinder center to the surface. The transverse profiles over a vertical cylinder of $r = 0.5$ m, and $z = 3$ and 5 m are given in **Figure 6.6**. The detection depth of the cylinder is on the same order of the sphere discussed in Section 6.2.2. The anomaly over the center of the cylinders of $r = 0.3$ and $0.5$ m are shown in **Figure 6.7**. The maximum depth of detection for these cylinders are 4 and 6 meters, respectively.

# 6.3. Experimental FT Investigations

The feasibility of using of ferrofluids as tracers was investigated in laboratory magnetometer surveys of various FT shapes which involved comparisons between the measured and the theoretically predicted values. A three axis miniature fluxgate magnetometer (model APS534, Applied Physics Systems, Mountain View, CA) was used in these experiments.

To effectively calculate the expected anomaly and to interpret the measured anomaly, the magnetic baseline was first determined by measuring the ambient field. The ambient field is a vector quantity and therefore has components in the $x$, $y$, and $z$ direction. For the present experiments, the vertical component of the field was maximized and the resulting vertical anomaly was recorded. A set of typical ambient field measurements are given in **Table 6.1**.

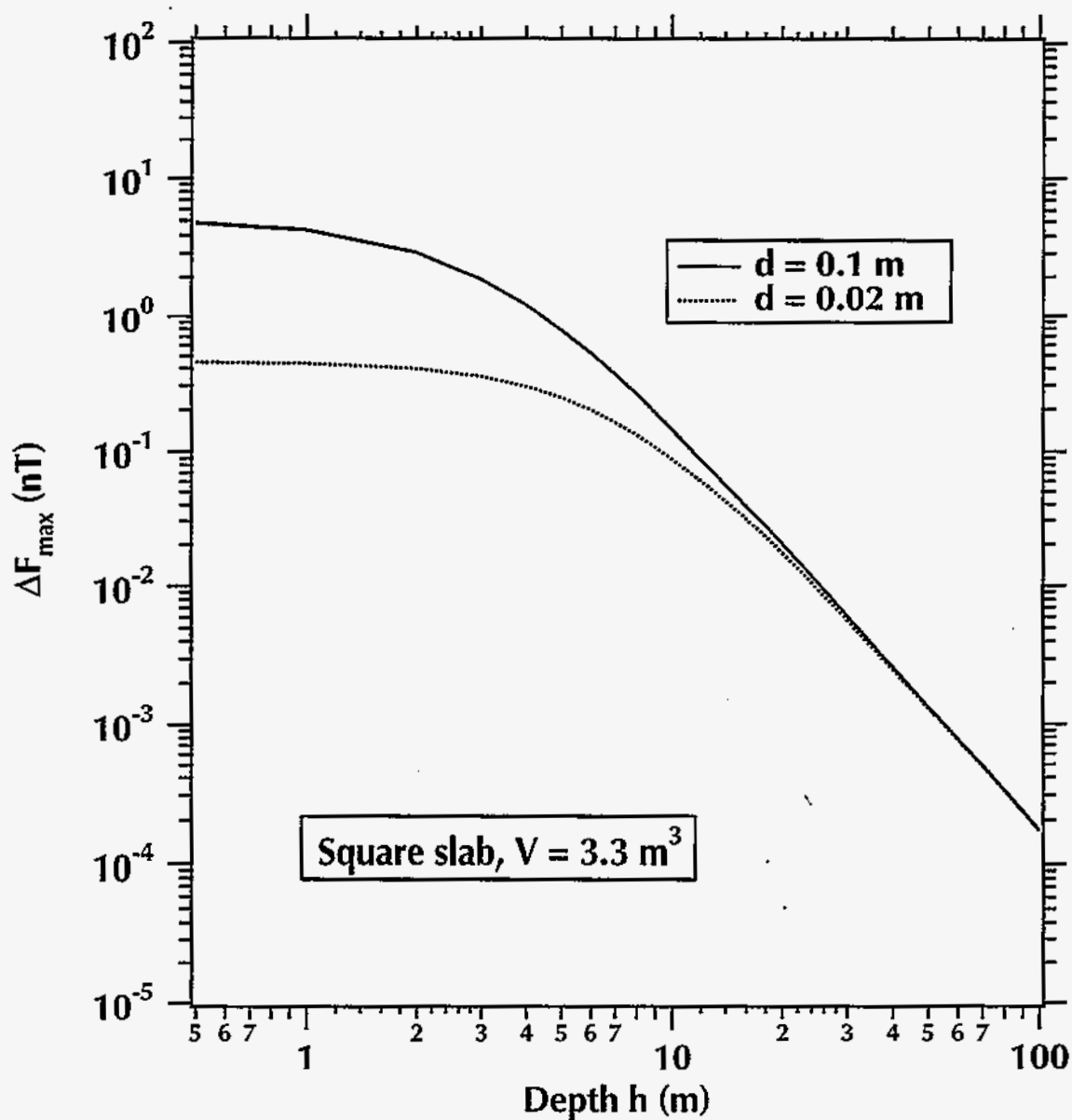**Figure 6.5.** Dependence of $\Delta F(a, d, x = 0, h)$ on the depth $h$ to a square slab anomaly of width $a$, thickness $d$ and constant volume $V \approx 3.3 \text{ m}^3$.
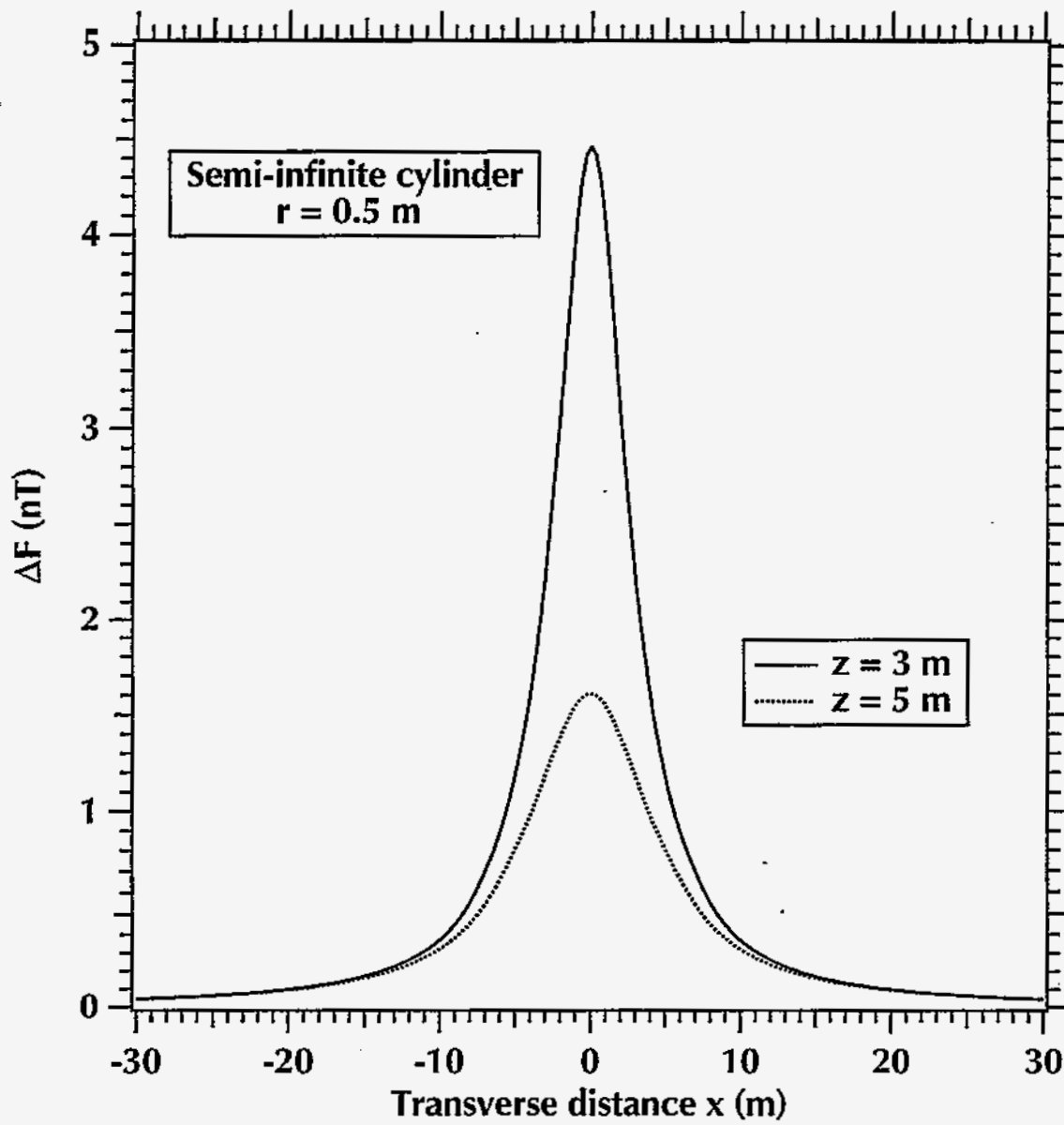
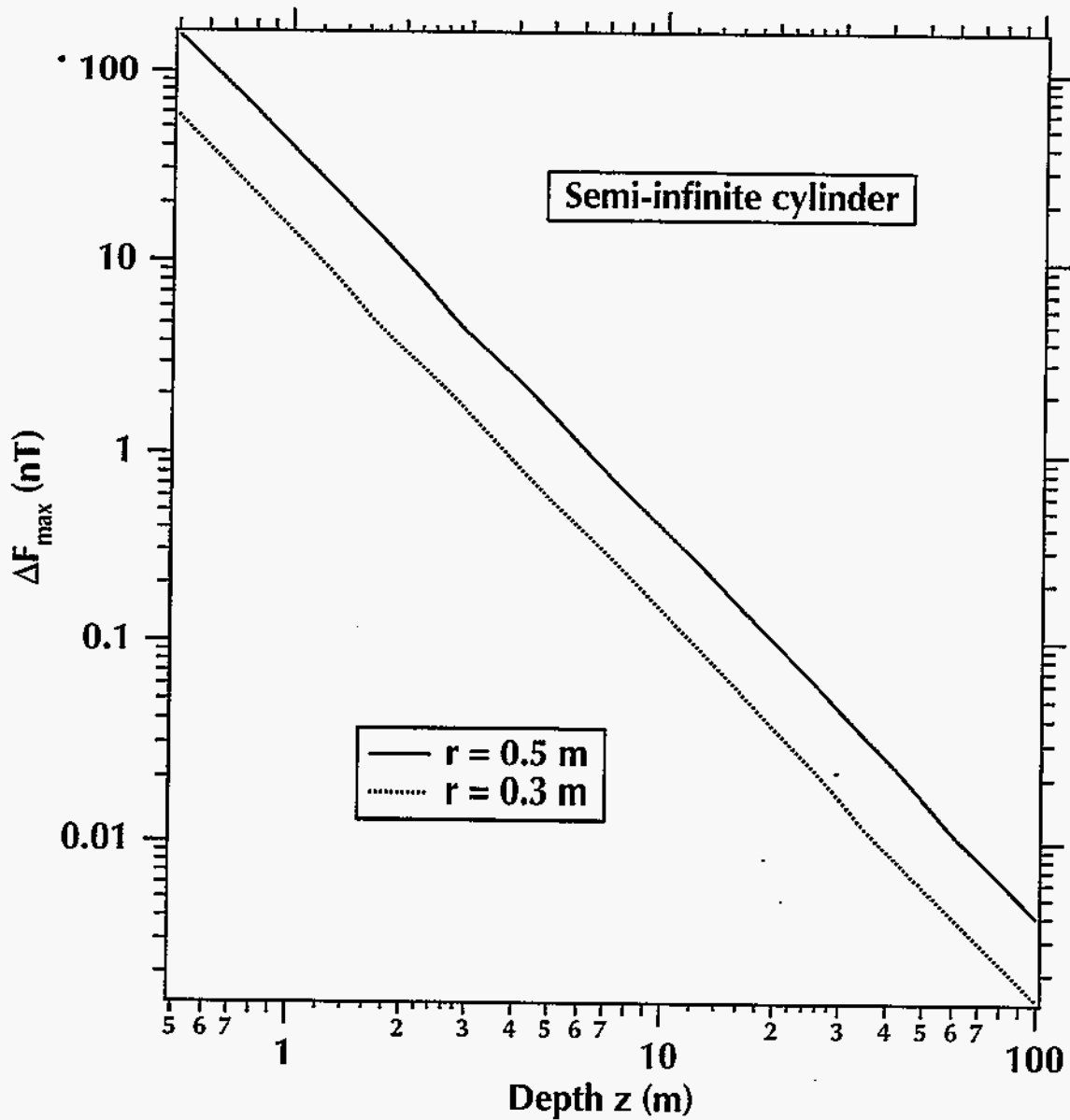**Figure 6.6.** $\Delta F(r, x, z)$ for a semi-infinite cylinder of radius $r = 0.5$ m.

**Figure 6.7.** Dependence of $\Delta F_{max} = \Delta F(r, x = 0, z)$ on the depth $z$ to a semi-infinite cylindrical anomaly of radius $r$.

The magnetometer had a excitation voltage of $\pm 10$ V and an output voltage of $\pm 5$ V. The output voltage for the $H_x$, $H_y$ and $H_z$ components of the ambient magnetic field was measured by a digital multimeter and was manually logged. After first ensuring that the inducing ambient field was consistent over the surface of the board, the magnetometer was aligned with the magnetic north. To minimize noise, the magnetometer was fixed in position and the anomaly-inducing FT volume was moved in relation to the probe over the gridded surface of the board ($0.01 \times 0.01$ m grid size). This maximized the resultant signal in the EW and vertical directions.

A major consideration in achieving reliable anomaly measurements is to minimize the noise in ambient fields. Such noise increases during the daylight hours due to solar effects and anthroprogenic activities. Periodic magnetic storms can also increase the noise level by an order of magnitude. Therefore, care has to be taken in the selection of the location and time of the magnetic measurements. All measurements were taken outdoors, away from buildings, power lines and/or other large metallic structures, with the magnetometer placed on a carefully leveled plywood board resting on a resin table.

In the following experiments, the magnetometer was placed on the level, gridded board. To measure the anomaly from the ferrofluid samples (prepared as described in the following section), the samples were moved along a line perpendicular to the axis of the magnetometer (**Figure 6.8**). With this configuration, the vertical anomaly at the magnetometer position is negative. Although field measurements routinely achieve detection limits on the order of 1 nT, in these laboratory experiments the detection limit was about 2 nT.

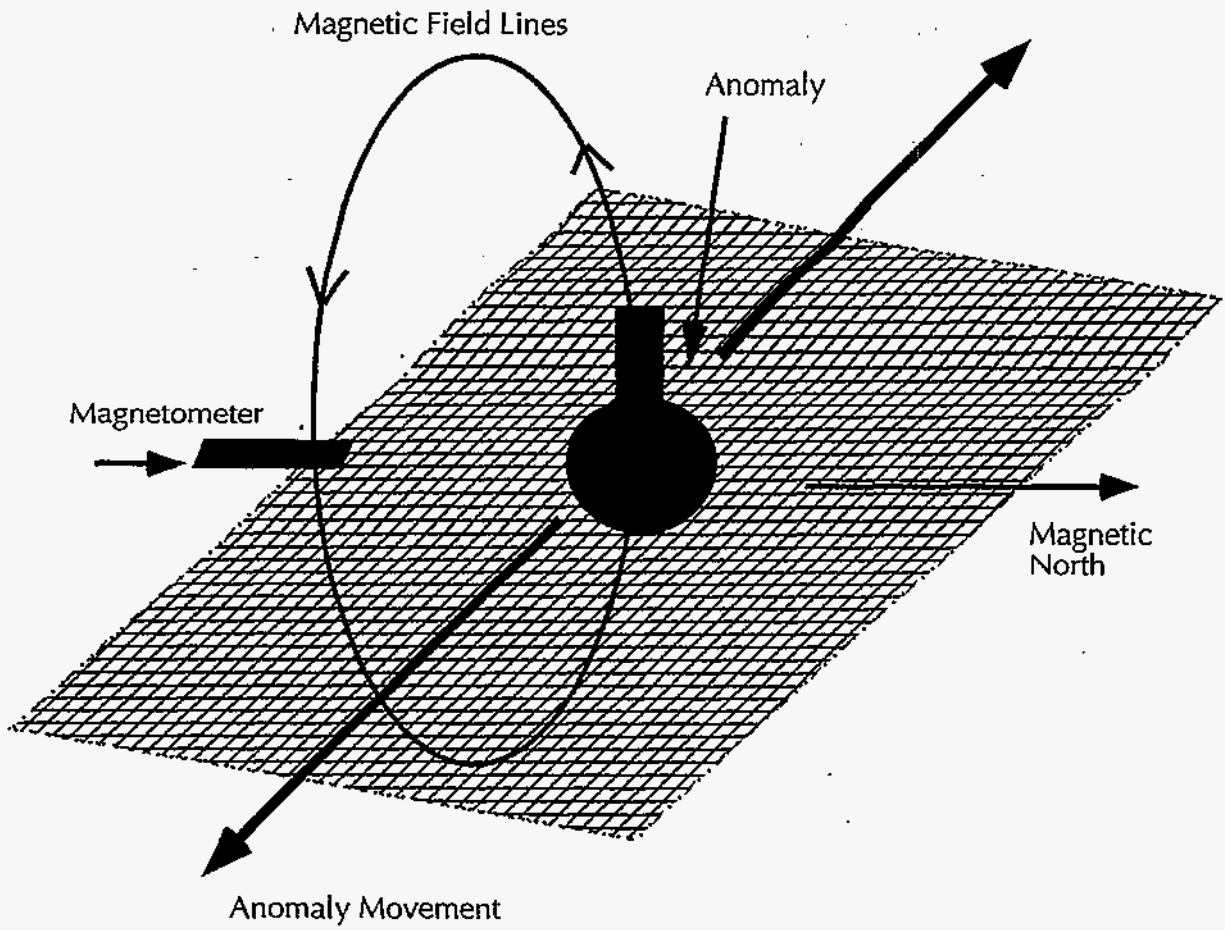| Table 6.1. Typical Ambient Magnetic Field Measurements | |
|---|---|
| **Component** | **Field (nT)** |
| $H_z$ (vertical) | 42,000 |
| $H_x$ (EW) | 22,000 |
| $H_y$ (NS) | 750 |
| Resultant (declination 18°) | 47,000 |

**Figure 6.8.** A schematic of the experimental approach in the measurement of the FT-induced anomalies.

### 6.3.1. Spherical Anomaly

To model the spherical anomaly described above, a 100 ml spherical flask was filled with 100% (i.e., undiluted) EMG 805$^{TM}$ ferrofluid. The resulting anomaly had a $V = 105$ ml. Using equation (6.4) and the $V = 3.3$ m$^3$ sphere as a reference, a general scaling relationship can be obtained to predict the anomaly. Assuming that the inducing fields are the same, we derive

$$\frac{h_1}{h_2} = \left(\frac{k_{m1} V_1}{k_{m2} V_2}\right)^{1/3}. \tag{6.11}$$

If $h_1$ is the depth to the $V_1 = 105$ ml flask and $h_2$ is the depth to the $V_2 = 3.3$ m$^3$ sphere, $k_{m1} = 0.23$ MKS is the susceptibility of the undiluted EMG 805$^{TM}$ ferrofluid in the flask and $k_{m2} = 0.014$ MKS is the susceptibility of 15% ferrofluid solution in the $V_2$ sphere, then

$$\frac{h_1}{h_2} = 0.08,$$

from which the maximum detection depth for the $V_1$ anomaly is determined as $h_{max} = 0.56$ m.

Predictions and measurements of the spherical anomaly-induced $\Delta F$ along the $x$-axis (transverse) at $h = 0.055$, 0.08, and 0.12 m are shown in **Figures 6.9** through **6.11**. As the distance from the magnetometer increases, the maximum anomaly decreases and broadens. Under the conditions of the experiments, the $\Delta F$ at $h = 0.12$ m is only four times the detection limit, and therefore considerable noise is apparent in the data. For all three traverses, however, a good match between predictions and measurements (in terms of anomaly shape, height and width) is observed.

The flask of ferrofluid was moved along the center line (i.e. along $h$ at $x = 0$) from $h = 0.035$ m to $h = 0.28$ m, and the maximum anomaly peak $\Delta F_{max}$ was recorded as it decreased with $h$. **Figure 6.12** shows a good agreement between the measured and the predicted $\Delta F_{max}$. The scattering at the larger $h$ values is due to the proximity of the measured anomaly to the limit of detection of the instrument.

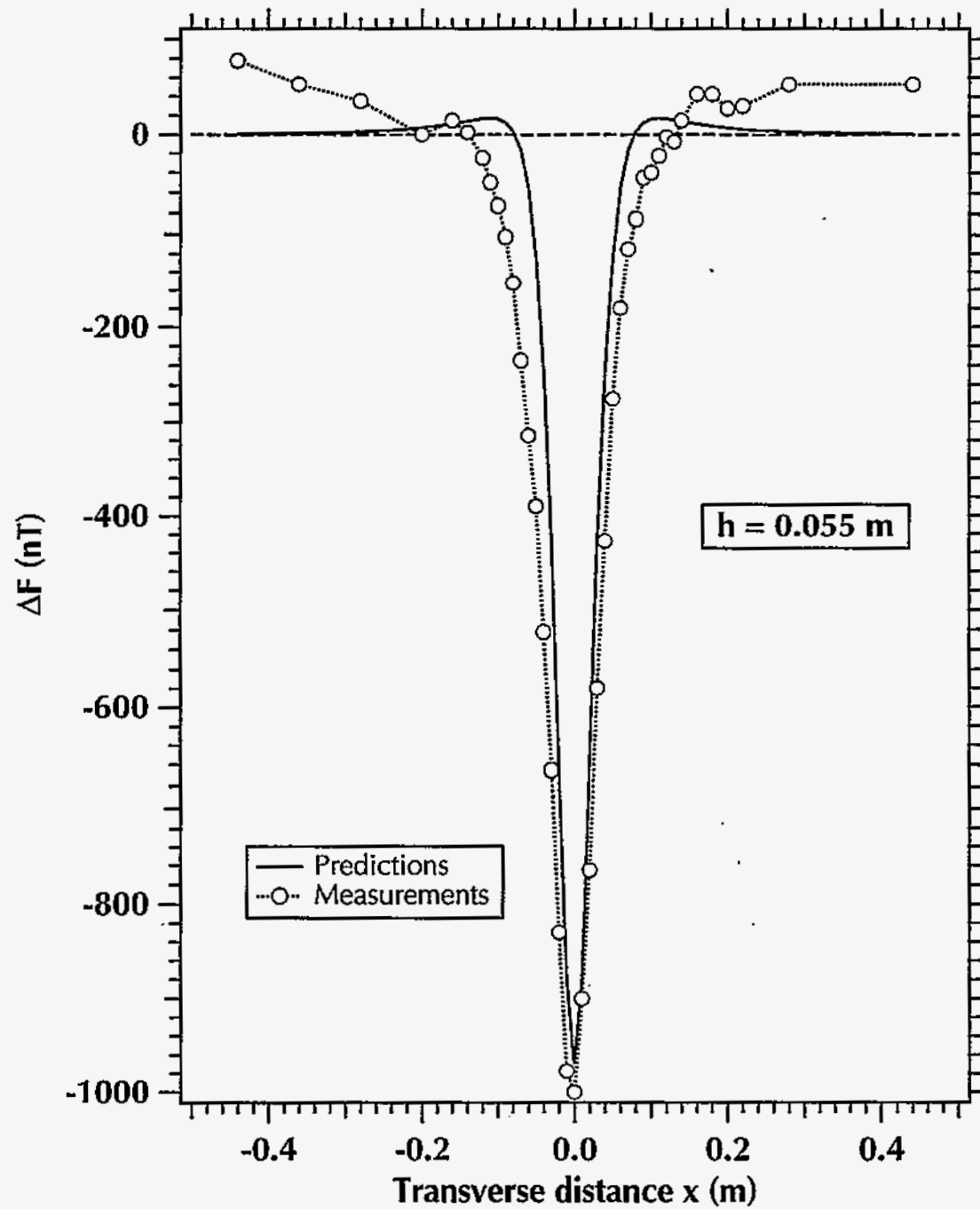**Figure 6.9.** Calculated and measured $\Delta F$ for a sphere with $V = 100$ ml at a depth $h = 0.055$ m.
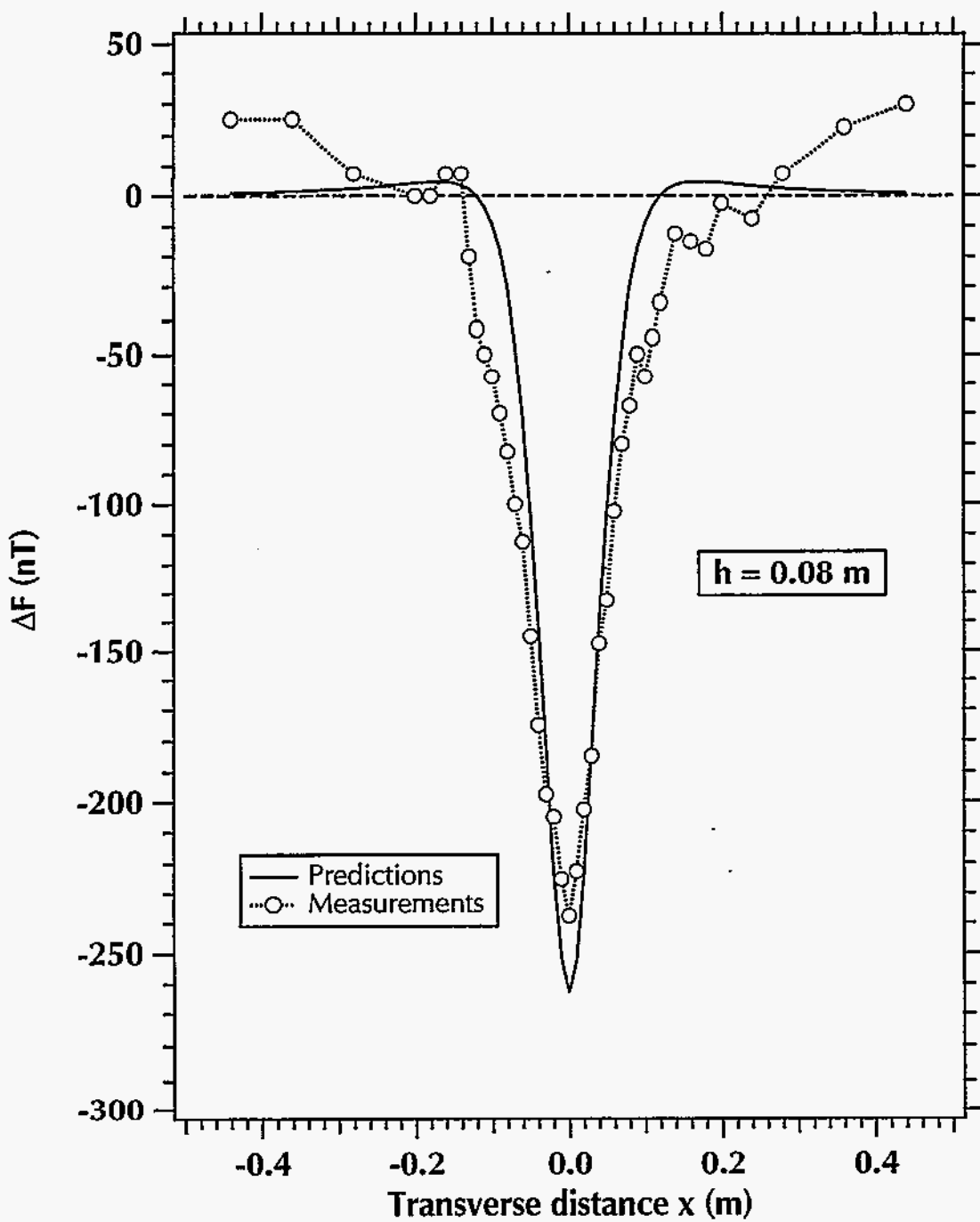
**Figure 6.10.** Calculated and measured $\Delta F$ for a sphere with $V = 100$ ml at a depth $h = 0.085$ m.
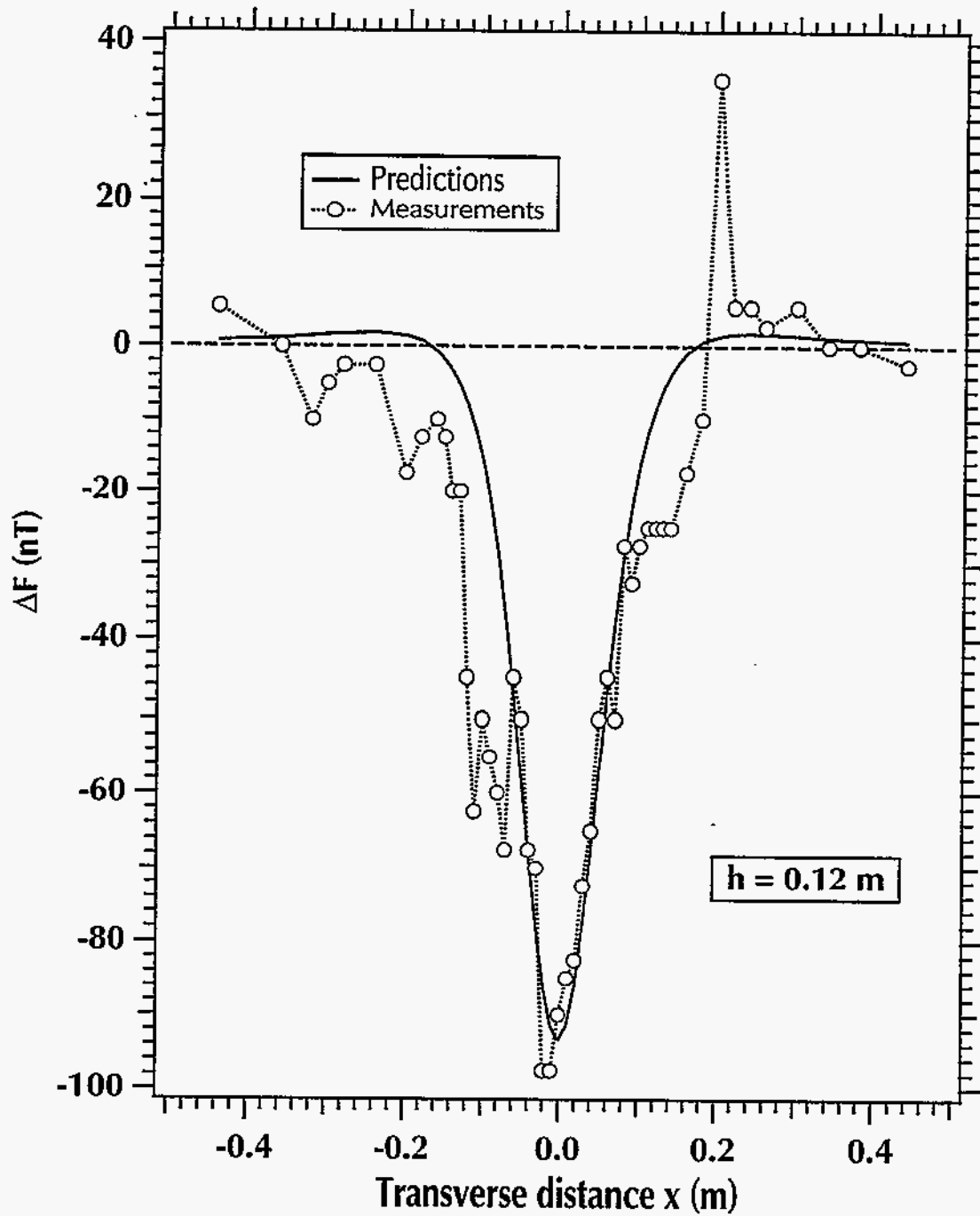
**Figure 6.11.** Calculated and measured $\Delta F$ for a sphere with $V = 100$ ml at a depth $h = 0.12$ m.
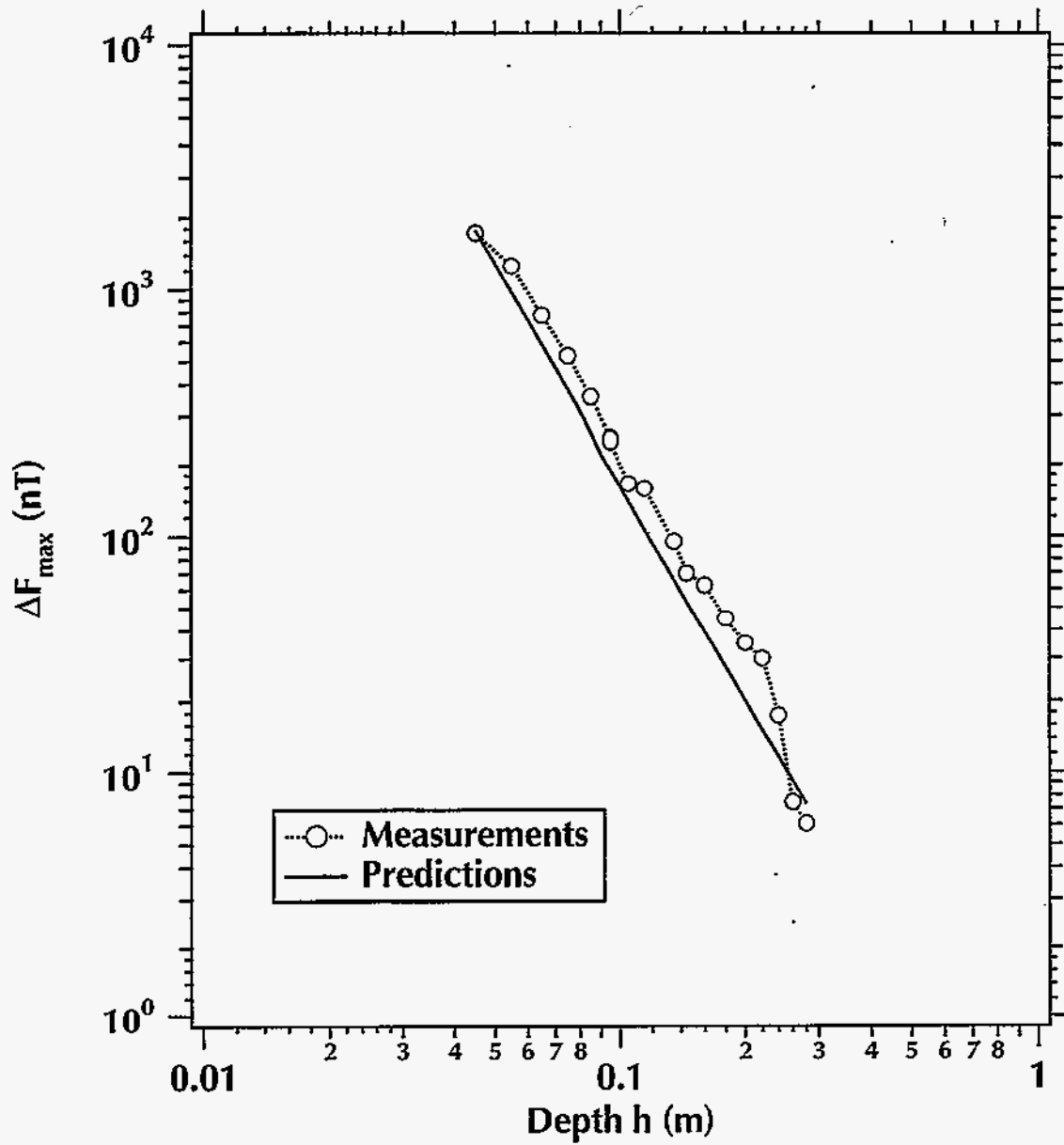
**Figure 6.12.** Calculated and measured $\Delta F_{max} = \Delta F(x = 0, h)$ for a buried sphere with a $V = 100$ ml.

## 6.3.2. Cylindrical Anomaly

An anomaly was created with a $V = 100$ ml cylinder ($r = 0.02$ m) filled with EMG 901 ferrofluid (**Table 6.2**). Measurements of the cylinder-induced anomaly along the transverse axes at $z = 0.03$, $0.05$, and $0.09$ m are shown in **Figure 6.13** through **6.15**, and are in very good agreement with the predictions of equation (6.10). The cylinder-induced anomaly is broader than that for the sphere, and does not have an $x$ region in which $\Delta F < 0$.

**Figure 6.16** shows a comparison of measured and predicted $\Delta F_{max} = \Delta F(x = 0, z)$ for $0.03$ m $\geq z \geq 0.28$ m. A very good agreement between the two data sets is observed.

## 6.3.3. Rectangular Slab Anomaly

A flat plate anomaly was created using a rectangular container with dimensions $0.03 \times 0.08 \times 0.12$ m. The container was filled with Monterey sand, and was then saturated with a 30% solution of EMG 805$^{TM}$ ferrofluid. The susceptibility of this rectangular slab system $k_{ms}$ is computed as $k_m = 0.0306$ MKS.

The flat plate anomaly was positioned so that the distance between its long edge and the magnetometer (i.e., the depth $h$) was $0.03$ m. A comparison of the $\Delta F$ measurements to predictions is shown in **Figure 6.17**. Although a scattering of the measurements is observed in the vicinity of the anomaly edges, there is a good agreement between measurements and predictions in terms of $\Delta F$ shape, width and magnitude.

| Table 6.2. Properties of the EMG 901$^{TM}$ Ferrofluid | |
|---|---|
| Viscosity at 27 $^0$C | 11 cp |
| Magnetite concentration (vol/vol) | 9.89% |
| Surfactant concentration (vol/vol) | 15% |
| Light mineral oil concentration (vol/vol) | 75.11% |
| Initial magnetic susceptibility | 0.337 MKS |
| Density | 1360 kg/m$^3$ |
| Saturation magnetization | $4.4 \times 10^4$ A/m |

**Figure 6.13.** Calculated and measured $\Delta F$ for a semi-infinite cylinder with $r = 0.02$ m at a depth $z = 0.03$ m.

**Figure 6.14.** Calculated and measured $\Delta F$ for a semi-infinite cylinder with $r = 0.02$ m at a depth $z = 0.05$ m.
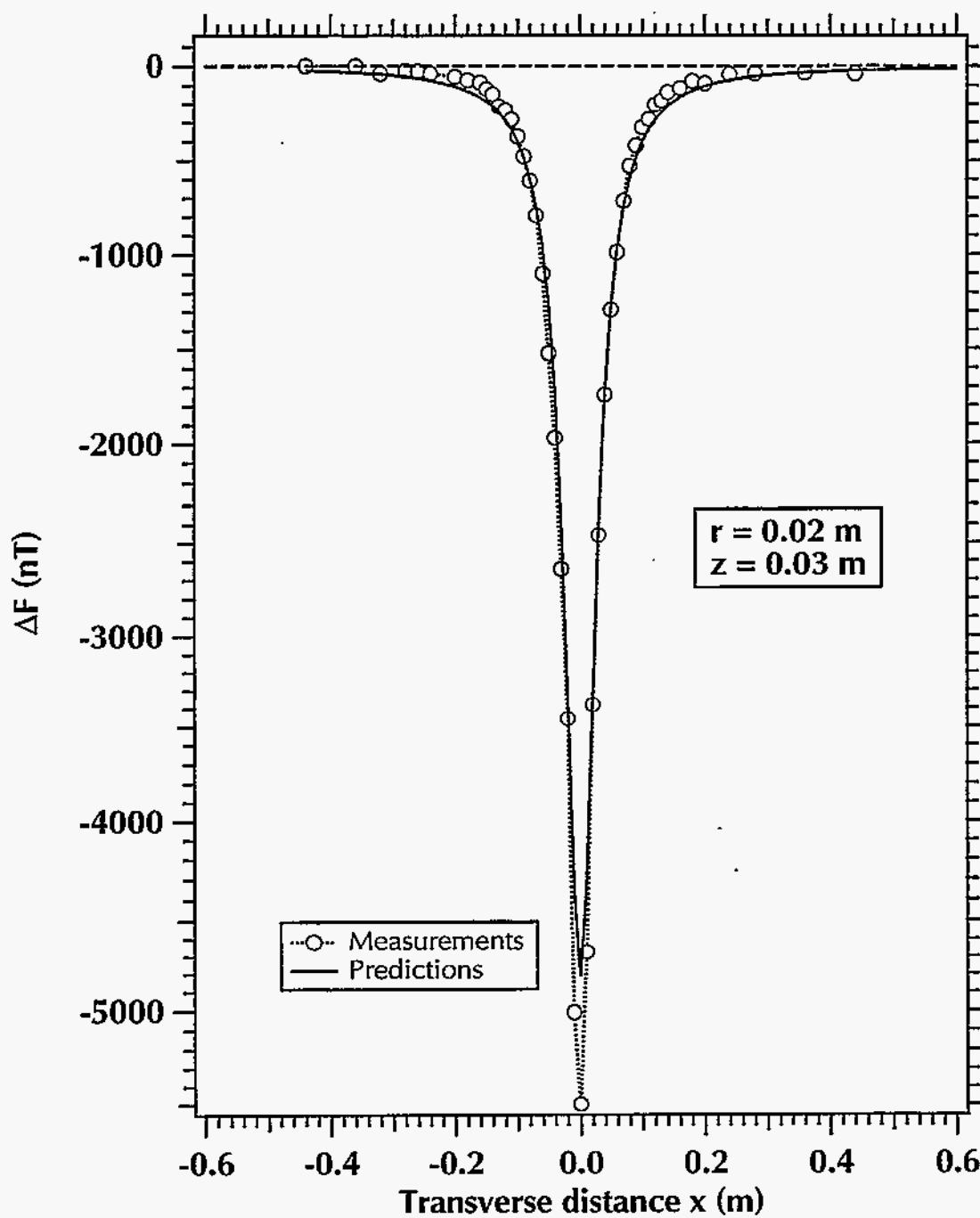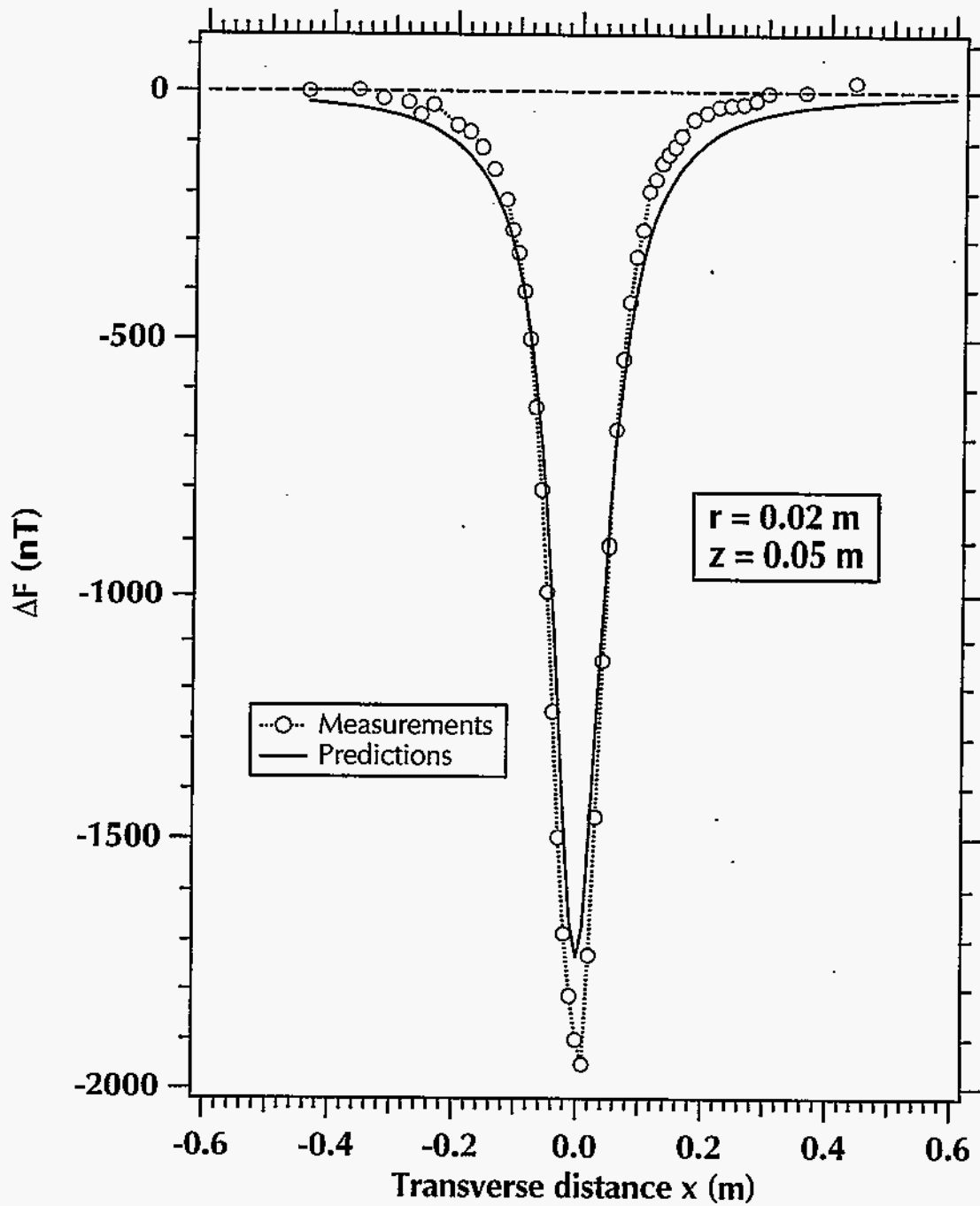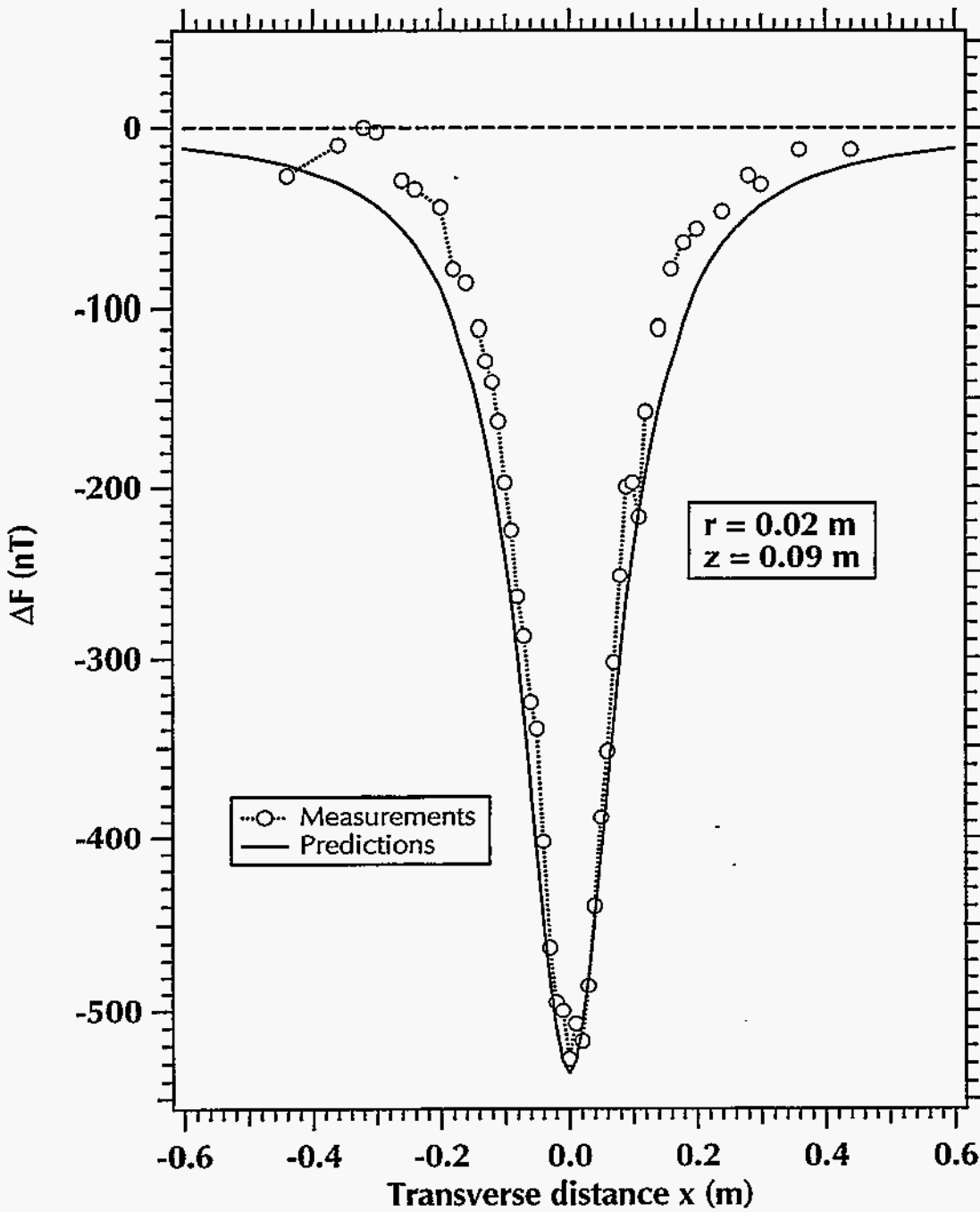
**Figure 6.15.** Calculated and measured $\Delta F$ for a semi-infinite cylinder with $r = 0.02$ m at a depth $z = 0.09$ m.
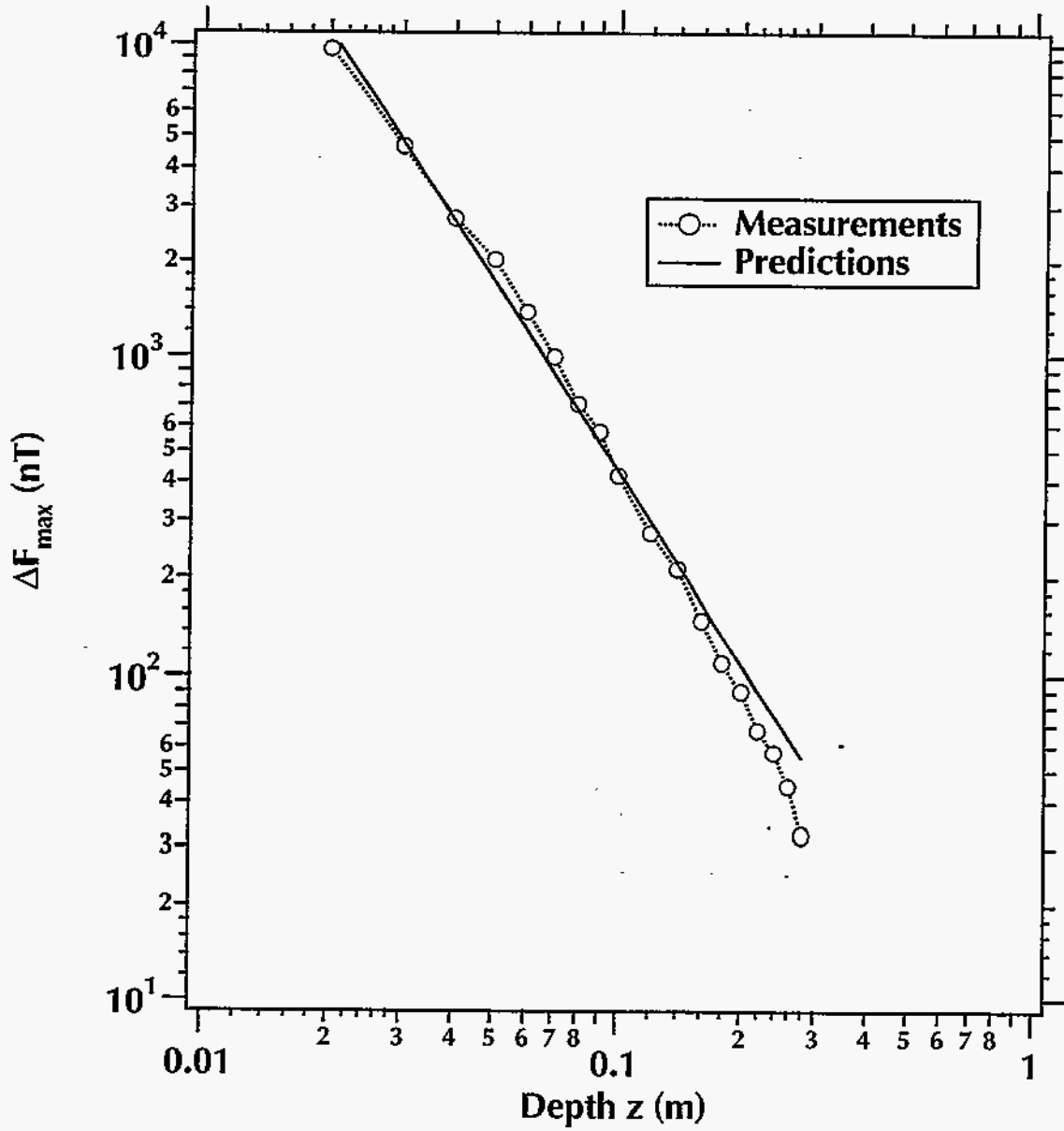
**Figure 6.16.** Calculated and measured $\Delta F_{max} = \Delta F(x = 0, z)$ for a semi-infinite cylinder with $r = 0.02$ m.
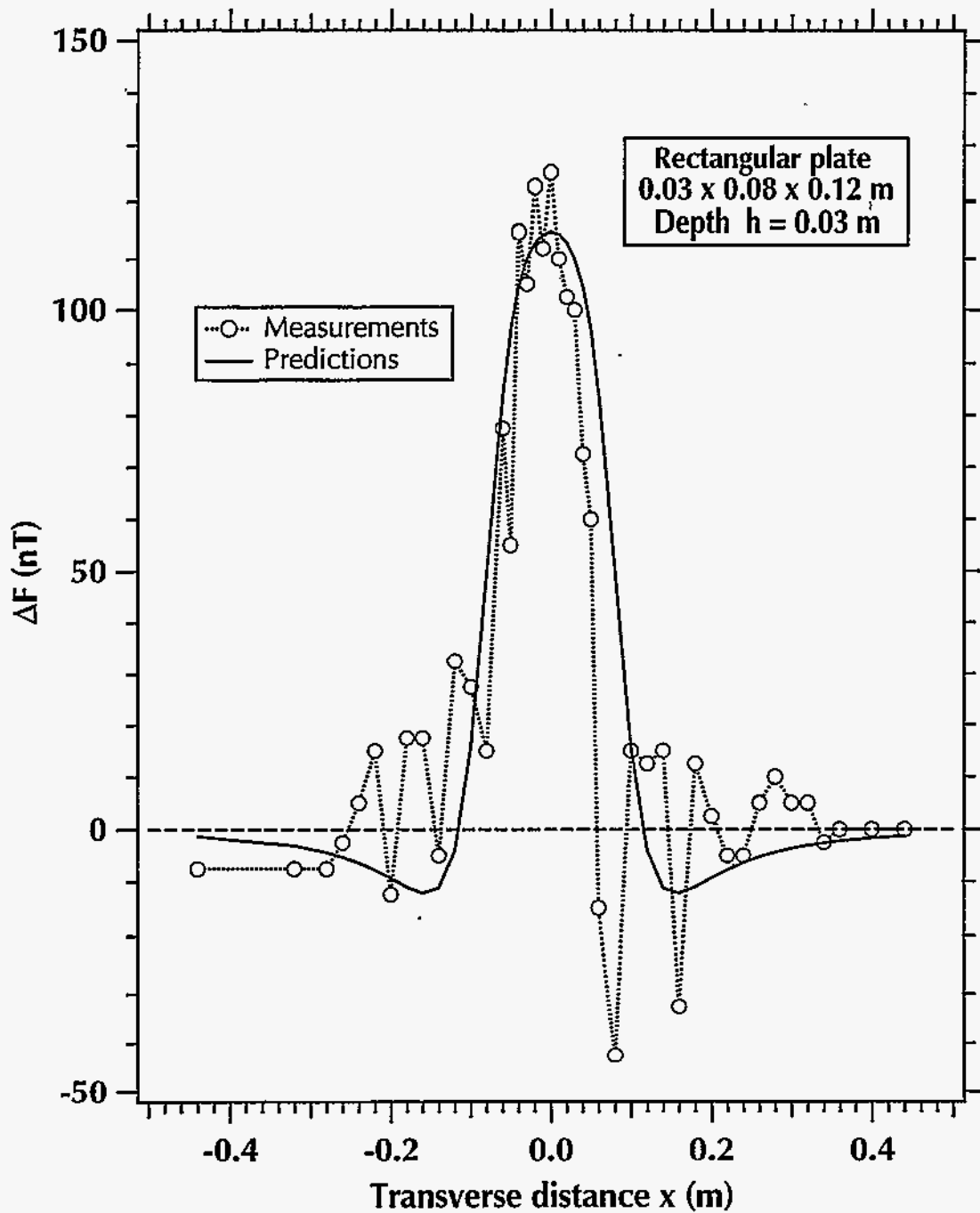
**Figure 6.17.** Calculated and measured $\Delta F$ for a $0.03 \times 0.08 \times 0.12$ m rectangular plate at a depth $h = 0.03$ m.

## 6.4. Synopsis

To investigate the feasibility of using ferrofluids as tracers (FT) in the subsurface, theoretical and experimental investigations of the magnetic anomalies they induce were conducted. The results of these studies confirm that the anomaly behavior can be accurately predicted by existing mathematical models.

Care must be exercised in the application of FT-based tracer techniques to minimize the magnetic noise, which can obscure small anomaly signals and significantly increase detection limits. One limiting factor in anomaly detection is the susceptibility of the ferrofluid, which is a function both of the particle size and the material properties of the magnetite in the ferrofluid. Larger magnetite particles increase the FT susceptibility, and thus the detection depth. The particle size of the magnetite is determined by the manufacturing process. The stability of the fluid is dependent on a force balance between particle interaction and repulsion between the surfactants attached to the fluid particles. Although the particle size can be increased, this affects adversely the FT stability [*Rosensweig*, 1979]. In addition, a FT with a larger particle size may exhibit increased (and undesirable) filtration effects when injected into a porous medium. New FTs, with the same particle size but with higher susceptibility (such as Nd-Fe-B-based FTs), could increase the detection depths of FTs and improve their tracer potential.

# 7. SUMMARY AND CONCLUSIONS

Ferrofluids are stable colloidal suspensions of magnetic particles in various carrier liquids [*Raj and Moskowitz*, 1990] with high saturation magnetizations. The solid, magnetic, single-domain particles have an average diameter of $3 - 15$ nm, and are covered with a molecular layer of a dispersant. Thermal agitation (Brownian motion) keeps the particles suspended, while the dispersant coating prevents the particles from agglomeration. Ferrofluids are superparamagnetic and move as a homogeneous single-phase fluid under the influence of a magnetic field, with no separate consideration for the magnetic particles and the carrier liquid. This attribute is responsible for the unique property of ferrofluids that they can be manipulated in virtually any fashion, defying gravitational or viscous forces in response to external magnetic fields [*Chorney and Mraz*, 1992].

In this report we review the results of our investigation of the potential of ferrofluids
1. to accurately and effectively guide (i) reactants (for *in-situ* treatment) or (ii) barrier liquids (low-viscosity permeation grouts) to contaminated target zones in the subsurface using electromagnetic forces, and
2. to trace the movement and position of liquids injected in the subsurface using geophysical methods.

Ferrofluids for Guiding liquids (FGs) have low viscosities ($< 5$ cp, allowing easy injection into the subsurface), small particle size ($3.5 - 15$ nm, minimizing potential filtration problems), and a very high saturation magnetization ($100 - 2,600$ Gauss). The ability of accurately guide FGs to specific areas in response to an external field has potentially important applications in the environmental restoration of the subsurface. We investigate the use of FGs to enhance the efficiency of *in situ* treatment and waste containment through (a)

accurate guidance and delivery of reagent liquids to the desired subsurface contamination targets and/or (b) effective sweeping of the contaminated zone as FGs move from the application point to an attracting magnet/collection point. FGs can be manufactured with the appropriate carrier liquids, reactants (e.g. oxidants) for *in situ* treatment and barrier liquids [*Moridis et al.*, 1995].

Current delivery and emplacement practices for *in situ* remediation or containment consists entirely of injection, and suffer from the adverse effects of heterogeneity which may cause the treatment effort to be short-circuited by preferential flow through highly-permeable zones. Magnetic fields are easier to manipulate than pressure fields, are unaffected by the significant heterogeneity of the soil hydraulic properties, and are significantly less affected by heterogeneity in the soil magnetic properties. Emplacement of liquids (for *in-situ* treatment or containment) in response to a magnetic field is thus expected to be more accurate and effective by allowing liquids to be focused and guided to the desired locations in the subsurface and more effectively sweeping the targeted treatment zone. FGs offer the unique advantage of a predictable and symmetric final distribution of the liquid regardless of the flow pathway. The transient approach to the final distribution may, however, be affected by medium heterogeneities.

Ferrofluid for Tracing liquids (FTs) cast a strong electro-magnetic signature, and are used commercially for magnetic pattern recognition in magnetic tapes, hard and floppy disks, and crystalline and amorphous alloys. The high saturation magnetization in the FTs provides a signature sufficiently strong for magnetic detection methods at low loading volumes (i.e. $1 - 5\%$). We investigated exploiting this property to develop a method for monitoring of liquid movement and position during injection using electromagnetic methods. FTs can also provide a significant detection and verification tool in containment technologies, where they can be injected with the barrier liquids to provide a strong signature allowing determination of the barrier geometry, continuity and integrity. FTs can also be used to identify high-permeability pathways, and thus allow the design of more effective remediation systems.

Starting from first principles, the partial differential equation of FG flow in porous media was derived. This equation is analogous to the conventional Darcy equation, from which it differs by the inclusion of magnetic and magnetostrictive forces. The appropriate multi-phase and/or solute transport equations governing the flow of subsurface liquids in the presence of FGs were identified, as well as relationships affecting the rheology of FGs. The corresponding equations of induction and magnetic field (Maxwell equations) were determined, and the appropriate modifications were made. Analytical 1-D solutions were developed for a FG moving in an FG-saturated medium in response to a magnetic field.

We studied the movement of an aqueous FG in response to magnetic fields from permanent magnets and electromagnets. Permanent magnets were shown to be far more effective than electromagnets in these small-scale experiments. In the presence of magnetic fields, ferrofluid columns were induced to move upward (against gravity) as a cohesive unit.

Ferrofluid drops on horizontal surfaces were attracted to Nd-Fe-B magnets located 24 cm away. The magnetopressure of FG-filled columns were also measured for varying magnetic fields and different ferrofluids.

Hele-Shaw experiments demonstrated the ability to guide FGs in response to external magnetic fields, and indicated that FGs remain stable and do not disperse during magnetic flow despite their complete water miscibility. As the fluid approached the magnet, its velocity increased due to the increasing magnetic field strength and gradient. An important observation with implications for FG emplacement was that the FGs accumulate against the magnet in a symmetric predictable distribution which is controlled only by the attributes of the magnetic field.

Experiments of magnetically-induced FG flow in porous media in 2-D sand beds confirmed the ability to guide FGs in response to fields from Nd-Fe-B magnets [Borglin and Moridis, 1998]. The FG flow pattern toward the magnet was very similar to that observed in the Hele-Shaw experiment. In general, FG fingers (corresponding to the strongest field and/or highest permeability pathways) move away from the initial FG pool toward the magnet. Once a continuous direct path to the magnet is established, accumulation of the fluid begins and the final FG distribution is an arc-shaped symmetric pool around the magnet. Practically identical observations are made with (a) different initial FG distributions, (b) different sand tray sizes and (c) variable distances between the initial FG position and the magnet. The importance of these observations lies in the realization that despite differently-shaped initial FG distributions, varying initial distance from the magnets, heterogeneous permeability fields and FG flow along preferential pathways, the final FG distribution is invariably predictable, symmetric and is controlled by the magnetic field. In other words, the final FG distribution is unaffected by heterogeneities in the properties of the porous media and flow patterns. The implication of this realization is that FGs with appropriate reagent-laden carrier liquids can be accurately guided to and positioned in contaminated target zones in the subsurface.

Practical FG applications involve the solution of coupled, strongly nonlinear equations of flow and magnetic field which are tractable only through numerical simulation. Using the TOUGH2 general simulator of flow and transport through porous media [Pruess, 1991a], the new module EOS7M, describing the behavior and flow of ferrofluids in the presence of a magnetic field, was developed, verified against analytical solutions, and validated against laboratory data [Oldenburg et al., 1998]. The EOS7M module accounts for the effects of the magnetic field on the ferrofluid, as well as the coupled effects of water-miscibility on the ferrofluid properties and its flow and transport characteristics.

We demonstrated the feasibility of using conventional magnetometry for detecting subsurface zones of injected FTs used to trace liquids injected for remediation or barrier formation [Borglin et al., 1998]. The geometric shapes considered were a sphere, a thin disk, a rectangular horizontal slab, and a cylinder. Simple calculations based on the principles

of magnetometry were made to determine the detection depths of FTs. Experiments involving spherical, cylindrical and horizontal slabs showed a very good agreement between predictions and measurements.

# 8. REFERENCES

Bhattacharyya, B.K., Magnetic Anomalies due to prism-shaped bodies with arbitrary polarization, *Geophysics, XXIX*(4), 517-526, 1964.

Bailey, R.L., Lesser known applications of ferrofluids, *J. Magnetism Magnetic Mater.*, *39*(1,2), 178-182, 1983.

Becker, A., and L.S. Collett, Magnetic losses in lunar materials, *Earth and Planetary Science Letters, 41*, 139-142, 1978.

Borglin, S., and G.J. Moridis, Experimental investigations of magnetically-driven flow of ferrofluids through porous media, LBL Report No. 40126, Lawrence Berkeley National Laboratory, Berkeley, California, 1998.

Borglin, S., A. Becker, and G.J. Moridis, Magnetic detection of ferrofluid injection zones, LBL Report No. 40127, Lawrence Berkeley National Laboratory, Berkeley, California, 1998.

Breiner, S., Applications Manual for Portable Magnetometers, Geometrics, Sunnyvale, California, 1973.

Chorney, A.F., and W. Mraz, Hermetic sealing with magnetic fluids, *Machine Design*, 79-82, May 1992.

de Wiest, R.J.M., *Flow Through Porous Media*, Academic Press, New York, 1969.

Dorgarten, H.-W., and C.-F. Tsang, Modeling the density-driven movement of liquid wastes in deep sloping aquifers, *Groundwater, 29*(5), 655-662, 1991.

Ferrofluidics, Application Note: Ferrofluids in the biomedical field, Ferrofluidics Corp., Nashua, New Hamp., 1992.

Herbert, A.W., C.P. Jackson, and D.A. Lever, Coupled groundwater flow and solute transport with fluid density strongly dependent on concentration, *Water Res. Res., 24*(10), 1781-1795, 1988.

Millington, R.J., Gas diffusion in porous media, *Science,130*(3367),100-102, 1959.

Moridis, G.J., and C.M. Oldenburg, Principles of ferrofluid flow in porous media, LNBL Report No. 40167, Lawrence Berkeley National Laboratory, Berkeley, California, 1998.

Moridis, G.J., L. Myer, P. Persoff, S. Finsterle, J.A. Apps, D. Vasco, S. Muller, P. Yen, P. Williams, B. Freifeld, and K. Pruess, First-Level Field Demonstration of Subsurface Barrier Technology Using Viscous Liquids, LBL Report No. 37520, Lawrence Berkeley National Laboratory, Berkeley, California, 1995.

McCaig, M., *Permanent Magnets in Theory and Practice*, 1st edn, John Wiley & Sons, New York, 1977.

McCaig, M. and A.G. Clegg, *Permanent Magnets in Theory and Practice*, 2nd edn, John Wiley & Sons, New York, 1987.

Morimoto, Y., Magnetic guidance of ferro-colloid entrapped emulsion for site-specific drug delivery, *Chemical and Pharmaceutical Bulletin (Tokyo), 48*, 1279-1284, 1983.

Moskowitz, R., Dynamic sealing with magnetic fluids, *ASLE Transactions, 18*(2), 135-143, 1975.

Newbower, R.S., A new technique for circulatory measurements employing magnetic fluid tracers, in Proceedings, 1972 Biomedical Symp., San Diego, 1972.

Oldenburg, C., and K. Pruess, Dispersive transport dynamics in a strongly coupled groundwater-brine flow system, *Water Resour. Res., 31*(2), 289-302,1995.

Oldenburg, C.M., Borglin, S.E., and G.J. Moridis, On modeling flow and transport of magnetic fluids in porous media, LBL Report No. 40146, Lawrence Berkeley National Laboratory, Berkeley, California, 1998.

Pruess, K., TOUGH User's Guide, Nuclear Regulatory Commission, Report NUREG/CR-4645, 1987 (also Lawrence Berkeley Laboratory Report LBL-20700, Berkeley, California, 1987).

Pruess, K., TOUGH2 - A general-purpose numerical simulator for multiphase fluid and heat flow, LBL Report No. 29400, Lawrence Berkeley Laboratory, May 1991a.

Pruess, K., EOS7, An equation-of-state module for the TOUGH2 simulator for two-phase flow of saline water and air, Lawrence Berkeley Laboratory Report LBL-31114, Berkeley, California, August 1991b.

Raj, K., and R. Moskowitz, Commercial applications of ferrofluids, *Journal of Magnetism and Magnetic Materials, 85*, 233-245, 1990.

Reeves, M., Ward, D.S., Johns, N.D., and Cranwell, R.M., Theory and implementation of SWIFT II, the Sandia Waste-Isolation Flow and Transport Model for Fractured Media, Report No. SAND83-1159, Sandia National Laboratories, Albuquerque, N.M., 1986.

Rosensweig, R.E., Fluid dynamics and science of magnetic liquids, in *Advances in Electronics and Electron Physics*, Vol. 48, edited by L. Marton, pp. 103-199, Academic Press, New York, 1979.

Rosensweig, R.E., *Ferrohydrodynamics*, Cambridge University Press, 1985.

Saffman, P.G., and G. Taylor, The penetration of a fluid into a porous medium or Hele-shaw cell containing a more viscous liquid, *Proc. Royal Soc. of London*, Series A, vol. 246, 312-331, 1958.

Scheidegger, A.E., General theory of dispersion in porous media, *Journal of Geoph. Res.*,

66(10), 3273-3278, 1961.

Shliomis, M.I., Effective viscosity of magnetic suspensions, *Soviet Phys. JETP 34*(6), 1281-1294, 1972.

Senyei, A.E., and K. Widder, Drug targeting: Magnetically responsive albumin micro-spheres - A review of the system to date, *Gynecology and Oncology, 12*(1), 21-33, 1981.

Telford, W.M., L.P. Geldart, and R.E. Sheriff, *Applied Geophysics*, 2nd Edition, Cambridge University Press, Cambridge, New York, 1990.

Voss, C.I., *A Finite-Element Simulation Model for Saturated-Unsaturated, Fluid-Density-Dependent Ground-Water Flow with Energy Transport or Chemically-Reactive Single-Species Solute Transport*, U.S. Geological Survey, Reston, Virginia, 1984.

# 8. References

References

# 9. ACKNOWLEDGEMENTS

## 9. Acknowledgements